iScience

CellPress
OPEN ACCESS

Article

Postnatal *Arx* transcriptional activity regulates functional properties of PV interneurons

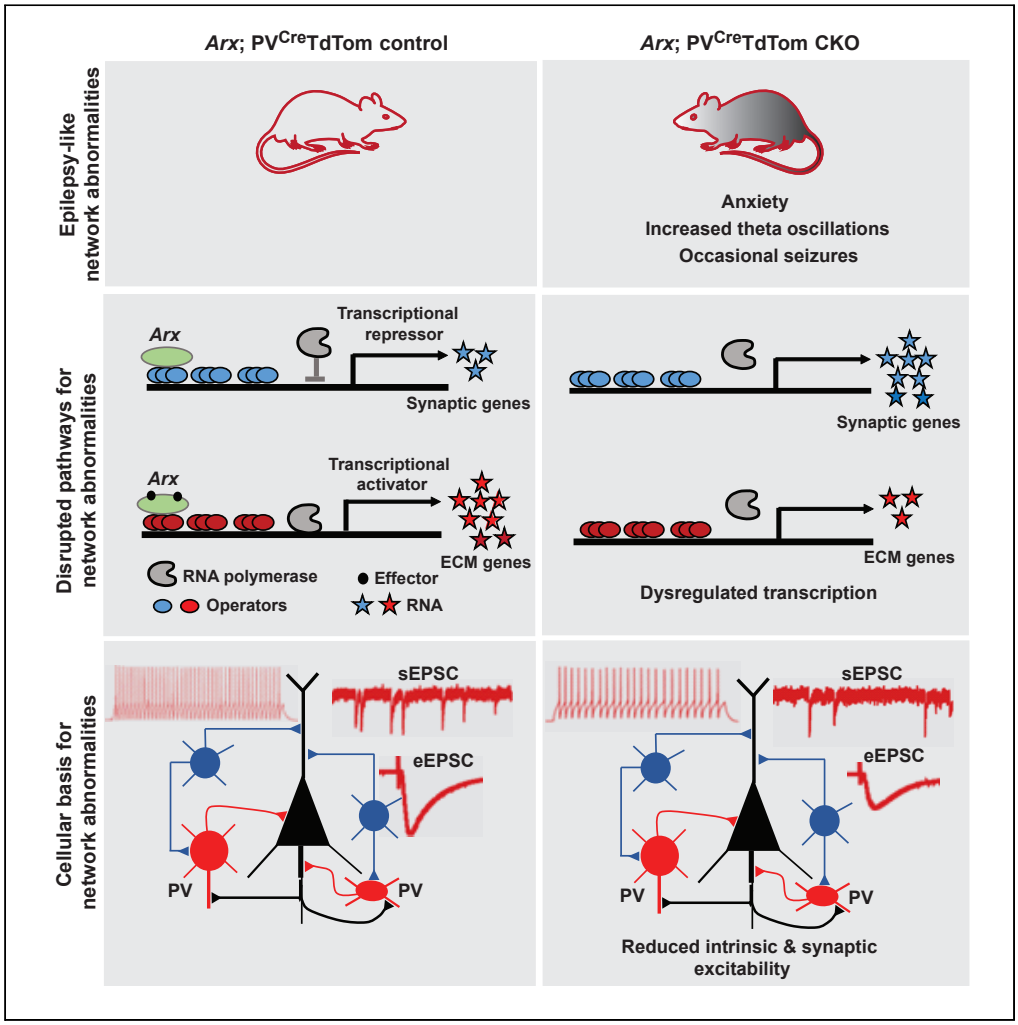

Donald J. Joseph, Markus Von Deimling, Yuiko Hasegawa, ..., Rashmi Risbud, Almedia J. McCoy, Eric D. Marsh

marshe@email.chop.edu

HIGHLIGHTS

Arx CKO mice displayed abnormal theta rhythms, occasional seizures, and anxiety

Loss of *Arx* in PV interneurons broadly altered their gene expression profiles

The perineuronal net around PV interneurons was altered in *Arx* CKO mice

Loss of *Arx* in PV interneurons altered their intrinsic and synaptic properties

Joseph et al., iScience *24*, 101999
January 22, 2021
https://doi.org/10.1016/j.isci.2020.101999

iScience

CellPress
OPEN ACCESS

Article

Postnatal *Arx* transcriptional activity regulates functional properties of PV interneurons

Donald J. Joseph,[1] Markus Von Deimling,[1,5] Yuiko Hasegawa,[1] Ana G. Cristancho,[1] Rebecca C. Ahrens-Nicklas,[2,3] Stephanie L. Rogers,[1] Rashmi Risbud,[1] Almedia J. McCoy,[1] and Eric D. Marsh[1,3,4,6,*]

SUMMARY

The transcription factor Aristaless-related X-linked gene (*Arx*) is a monogenic factor in early onset epileptic encephalopathies (EOEEs) and a fundamental regulator of early stages of brain development. However, *Arx* expression persists in mature GABAergic neurons with an unknown role. To address this issue, we generated a conditional knockout (CKO) mouse in which postnatal *Arx* was ablated in parvalbumin interneurons (PVIs). Electroencephalogram (EEG) recordings in CKO mice revealed an increase in theta oscillations and the occurrence of occasional seizures. Behavioral analysis uncovered an increase in anxiety. Genome-wide sequencing of fluorescence activated cell sorted (FACS) PVIs revealed that *Arx* impinged on network excitability via genes primarily associated with synaptic and extracellular matrix pathways. Whole-cell recordings revealed prominent hypoexcitability of various intrinsic and synaptic properties. These results revealed important roles for postnatal *Arx* expression in PVIs in the control of neural circuits and that dysfunction in those roles alone can cause EOEE-like network abnormalities.

INTRODUCTION

Mutations in the *Aristaless Related homeobox* transcription factor (ARX) cause early onset epileptic encephalopathies (EOEEs), a wide spectrum of disorders characterized by pharmacoresistant seizures, persistent electroencephalography (EEG) abnormalities, and cognitive deficits (Shoubridge et al., 2010). ARX has multiple roles in development, including cell cycle regulation in dorsal excitatory precursors and migration/fate specification of ventral interneuron precursors. Interestingly, ARX is downregulated in dorsal precursors upon exiting the cell cycle but remains expressed in migrating and mature interneurons. This complex pattern of expression is highly suggestive of distinct roles for ARX in the different stages of brain development.

Arx mouse models generated from conditional embryonic gene deletion or mutations have generally recapitulated human EOEEs and exhibited a complex pattern of spontaneous seizures, motor dysfunction, and learning impairments (Colombo et al., 2007; Dubos et al., 2018; Kitamura et al., 2002; Lee et al., 2017; Marsh et al., 2009; Simonet et al., 2015). Although the exact mechanisms by which pathogenic variation of *Arx* results in the EOEEs is currently unclear, accumulating evidence has converged toward the concept of interneuonopathy as a causative event (Kato and Dobyns, 2005). The underlying implication of this concept is that *Arx*-mediated loss of specific GABAergic interneurons leads to emergent hyperexcitable networks. However, it is currently unknown whether the phenotypes in ARX-linked EOEEs are exclusively due to ARX dysfunction in both interneuron and excitatory neuron progenitors or whether its persistent dysfunction in all or a subpopulation of mature interneurons plays a significant role in the evolution of seizures, EEG, and other phenotypes in EOEE in patients (Nordli, 2012). Therefore, investigations into the role of postnatal *Arx* expression are needed for a more comprehensive understanding of the underlying pathologic mechanisms of EOEEs and the contribution of sustained expression of this transcription factor (TF) to the evolution and/or manifestation of certain clinical phenotypes of EOEEs.

The loss of ARX function in postnatal interneurons could impair postnatal neural networks and consequently influence the developmental trajectories and the pleiotropic phenotypes of EOEEs. Indeed, three

[1]Division of Child Neurology, Children's Hospital of Philadelphia, Abramson Research Center, Rm. 502, 3615 Civic Center Boulevard, Philadelphia, PA 19104, USA

[2]Division of Metabolism, Children's Hospital of Philadelphia, Philadelphia, PA 19104, USA

[3]Department of Pediatrics, Children's Hospital of Philadelphia, Philadelphia, PA 19104, USA

[4]Department of Neurology, Perelman School of Medicine at the University of Pennsylvania, Philadelphia, PA 19104, USA

[5]Klinik für Urologie, Städtisches Klinikum Lüneburg, Bögelstraße 1, 21339 Lüneburg, Germany

[6]Lead Contact

*Correspondence: marshe@email.chop.edu

https://doi.org/10.1016/j.isci.2020.101999

lines of evidence in the mouse literature suggest an important role for impaired postnatal *Arx* transcriptional activity in the pathogenic mechanisms of *Arx*-related disorders. First, mild and disparate loss of GABAergic neurons have been noted in various *Arx* knock-in mice carrying polyalanine insertion mutations (Beguin et al., 2013; Dubos et al., 2018; Kitamura et al., 2002, 2009; Lee et al., 2017; Price et al., 2009), leaving a significant number of interneurons with dysfunctional *Arx* signaling intact. Second, although $Arx^{-/Y}$; *Dlx5/6*CIG mice exhibit a more robust interneuron loss phenotype, the male mice suffer from early postnatal lethality, whereas the females survive with variable *Arx* expression (Marsh et al., 2009). Finally, seizures noted in early postnatal $Arx^{-/Y}$; *Dlx5/6*CIG mice evolved from no spasms to full-blown human-like infantile spasms in adult males (Marsh et al., 2009). Taken together, these observations suggest that postnatal *Arx* transcriptional activity in GABAergic neurons may be necessary for broad neural circuit functions in the adult brain and that dysfunction in this postnatal role could contribute to the manifestation and/or evolution of EEOE phenotypes.

Cortical GABAergic interneurons constitute just 20% of the neuronal population, but they influence virtually all stages of circuit maturation due in part to their extensive heterogeneity and extended maturation trajectory (Klausberger and Somogyi, 2008; Le Magueresse and Monyer, 2013). Despite their heterogeneity, recent studies have parsed out interneurons into three major classes (PV, SST, and $5HT_3R$) and have demonstrated that each subclass, for the most part, adopts a different maturation trajectory by virtue of their birth date (Le Magueresse and Monyer, 2013). The PV subclass has a particularly long window of maturation (Doischer et al., 2008) and their extended developmental trajectory is thought to provide several windows of vulnerability during which aberrant signaling factors can contribute to neurodevelopmental disorders (Morishita et al., 2015). Indeed, the function of PVIs is well known to be altered in several neurodevelopmental disorders, and emerging studies have now demonstrated that certain disease phenotypes can be replicated by selective ablation of a handful of genetic risk factors in these interneurons during postnatal development (Hu et al., 2014). Although *Arx* is highly expressed in PVIs compared with most other interneuron subtypes during early postnatal development (Fishell and Kepecs, 2019), the functional significance for this high and sustained expression has not been addressed. Thus, an understanding of how ongoing *Arx* transcriptional activity affects the postnatal maturation trajectory of PVIs is an important objective for the elucidation of the pathologic mechanisms of EOEEs. To that end, we generated a CKO mouse model in which *Arx* was postnatally ablated in PVIs and determined whether that could alter neural network function. We found a significant increase in hippocampal theta rhythms that was accompanied by occasional spontaneous seizures and anxiety-related behaviors. The disrupted genetic and molecular pathways underpinning these clinical phenotypes were primarily associated with a diverse array of extracellular-matrix-related genes. Finally, we found that the cellular basis for the hyperexcitable hippocampal networks in CKO mice was a profound reduction in the intrinsic and synaptic excitability of PVIs. Our data provide evidence that postnatal *Arx* transcriptional activity in PVIs is an important regulator of neural circuits and that loss of this function contributes to the pathologic mechanisms of EOEEs. Therefore, restoration of postnatal *Arx* transcriptional activity in PVIs in the postnatal brain following onset of EOEEs may be an effective strategy toward circuit-based therapies.

RESULTS

Conditional deletion of Arx in PVIs

To examine the contribution of postnatal *Arx* dysfunction in the pathogenic mechanisms of EOEEs, we generated mice lacking *Arx* only in PVIs by first crossing mice with Cre driven by the PV promoter (Hippenmeyer et al., 2005) to TdTomato (TdTom) (Madisen et al., 2010) reporter mice to generate *Arx*; PV^{Cre}TdTom mice (hereafter termed control mice; Figure 1A). Mice with Cre recombinase and TdTom expression in PVIs (*Arx*; PV^{Cre}TdTom mice) were then crossed with mice carrying *Arx* flanked *LoxP* sites ($Arx^{LoxP/LoxP}$) (Fulp et al., 2008; Marsh et al., 2009) alleles to generate $Arx^{Flox/y}$; PV^{Cre}TdTom CKO mice (hereafter termed *Arx* CKO mice; Figure 1A). Cre-recombination and mouse genotypes were confirmed by RT-PCR analysis in P21 mice (Figure 1B). Because *Arx* is an X-linked gene, we restricted our studies to male mice in both genotypes. We noted PV^{Cre}-driven recombination as measured by the appearance of TdTom + neurons in both control and *Arx* CKO mice as early as postnatal day 15 (P15) with increasing TdTom florescence at 35 days (P35) (Data not shown) and near-complete loss of *Arx* in TdTom-containing cells at 8 weeks (Figure 1C). Cell-type specificity of PV^{Cre} mice has been previously described (Fuchs et al., 2007; Hippenmeyer et al., 2005), and our timeline for PV^{Cre} recombination is consistent with a previous report by Carlen and colleagues (Carlen et al., 2012). We found very little overlap between TdTom and *Arx* immuno-histochemical signals from 6- to 8-week-old mice, suggesting that *Arx* was strictly ablated in PVIs (Figure 1C).

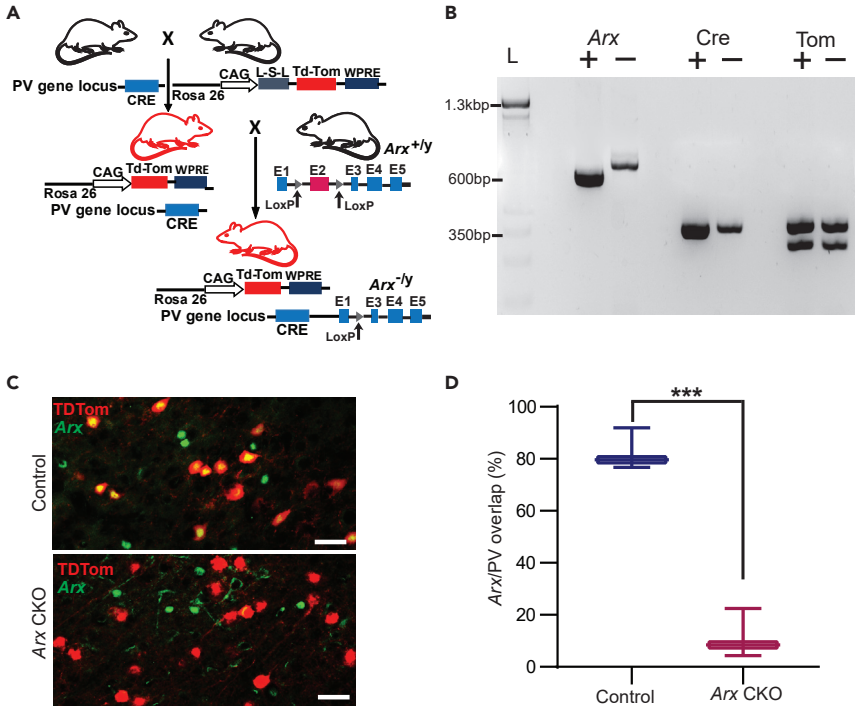

Figure 1. Conditional ablation of *Arx* in PVIs

(A) Schematic drawing of the breeding strategy for generation of *Arx* CKO mice.

(B) PCR-based analysis of mice genotypes. Lane L (1Kb) represents the DNA ladder. *Arx* CKO mice were identified by the presence of the TdTom allele and reduced recombinant Arx^{Flox} and Cre bands (–) compared with controls (+). Control mice also expressed the TdTom allele.

(C) Representative images from control and *Arx* CKO mice showing virtually no overlapping ARX immunoreactivity (green) in PVIs or TdTom + cells (red).

(D) Quantitative histochemical analysis of *Arx* expression in PVIs given as overlapping percent, showing very little overlap in *Arx* CKO mice (***$p < 0.001$; unpaired, 2-tailed Student's t test; control & *Arx* CKO: n = 3). The lower Q1 and upper Q3 quartiles of box plots (D) represent data outside the 5–95 percentile, and dots outside this range denote outliers. Scale bars: 25 μm.

Immunohistochemical staining of ARX and PV labeling of the same cohorts of mice revealed co-labeling of ARX and PV in 82.7 ± 4.6% of cortical and hippocampal PVIs in control mice but only in 11.7 ± 5.5% of PVIs in *Arx* CKO mice (Figure 1D). All *Arx* CKO mice were viable, fertile, and displayed no obvious brain abnormalities (data not shown). As PV^{Cre}-driven recombination was not detectable before the second postnatal week, early developmental processes in our *Arx* CKO mice were not affected. Thus, our PV^{cre} and $Arx^{LoxP/LoxP}$ recombination approach resulted in a suitable *Arx* CKO mouse model to investigate the role of postnatal *Arx* transcriptional activity in the maturing brain.

Loss of *Arx* led to increased theta oscillations and presence of occasional seizures

As the major phenotype in *Arx*-linked EOEEs are seizures and an abnormal EEG, we first examined EEG oscillatory activity and noted that power spectra calculated from hippocampal and cortical electrodes either during night or during day recordings did not differ between control and *Arx* CKO mice (Figures 2A–2C). However, analysis of hippocampal theta rhythms in epochs of high-theta oscillatory activities in those recordings revealed changes in theta power spectra (Figure 2E). Specifically, *Arx* CKO mice showed an increase in normalized peak power spectra in the theta frequency bands (Figure 2F). We also examined the EEG recordings for the presence of seizures and observed spontaneous electrographic seizures in some *Arx* CKO mice (2/12) but not in control mice (0/8; Figure 2G). Typically, seizure onset was marked by fast and high-amplitude spikes (100μV/5–10Hz), lasting more than 60 s and followed by a prolonged post-ictal flattening period (Figure 2G). These results demonstrate that the loss of *Arx* in PVIs alone is sufficient for the induction of epilepsy-like network hyperexcitability.

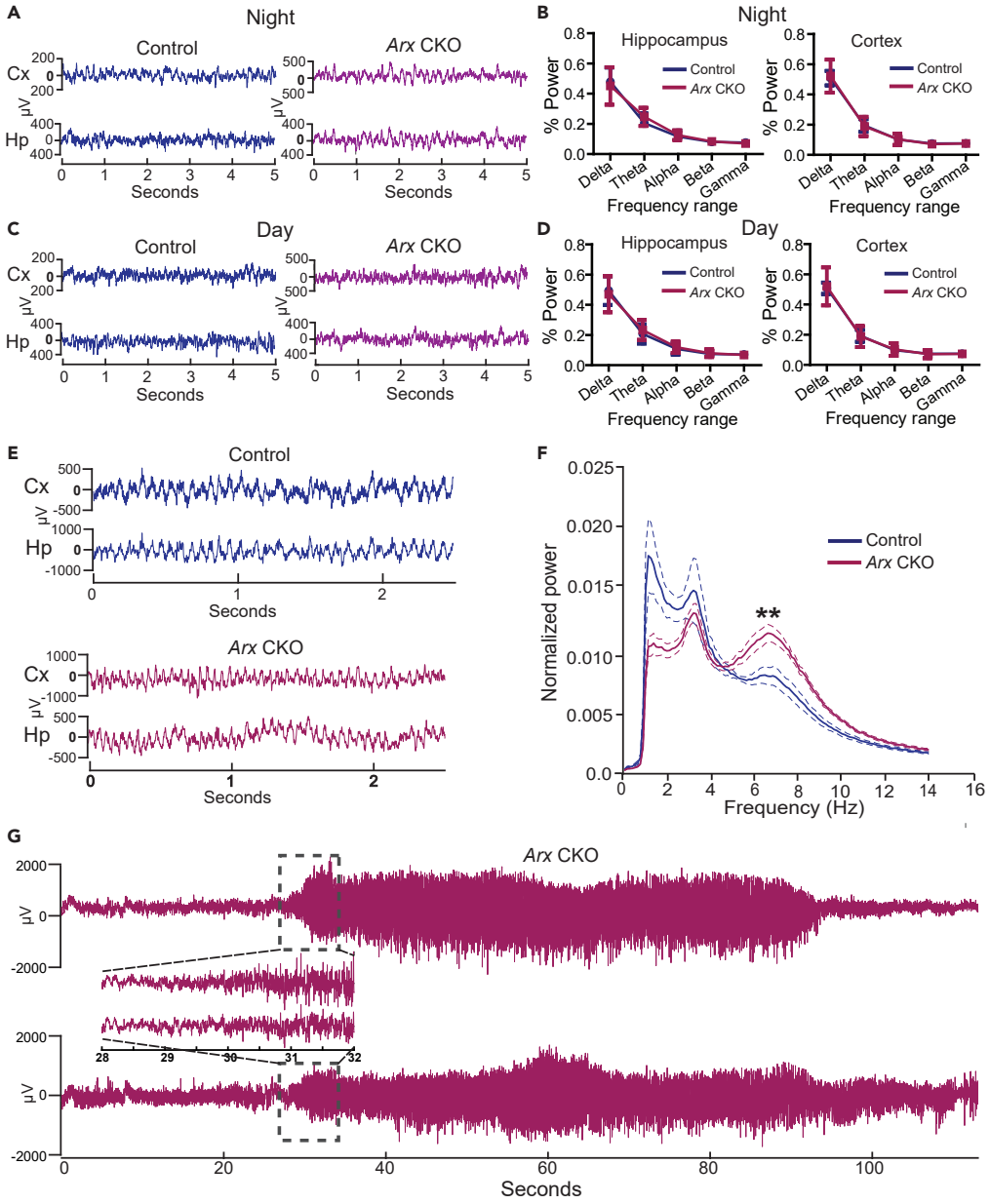

Figure 2. Loss of *Arx* in PVIs resulted in increased theta rhythms and occasional seizures

(A and C) Representative traces of night (A) and day (C) time hippocampal and cortical EEG recordings.

(B and D) Grand average of normalized hippocampal (Left plots) and cortical (Right plots) power spectra from night (B) and day time (D) EEG recordings showed no differences between genotypes ($p > 0.05$; $n \geq 8$ for both control and *Arx* CKO.

(E) Representative traces of EEG recordings dominated by theta oscillations.

(F) Power spectra of high theta epochs revealed a significant increase in theta rhythms in *Arx* CKO mice (**$p < 0.01$; Control, *Arx* CKO: n = 7, 8).

(G) Representative traces of two electrographic seizures noted in two different *Arx* CKO mice (2/12). Expanded view shows that a buildup of rhythmic spikes preceded seizure onset. Data analyzed by two-way ANOVA (C & D) and by the unpaired, 2-tailed Student's t test (F). All data are given as mean ± SD.

Increased anxiety-like behaviors in *Arx* CKO mice

Arx-linked disorders are characterized by significant impairments in cognitive and adaptive behaviors (Dubos et al., 2018; Jackson et al., 2017; Kitamura et al., 2009; Price et al., 2009; Simonet et al., 2015). Therefore,

we investigated if motor coordination, spatial learning and memory, fear conditioning, novel object recognition, and anxiety were abnormal in the *Arx* CKO mice. Motor coordination and strength were tested using the rotarod and grip strength tests. Motor coordination and learning rate measured in the rotarod test were indistinguishable from control mice (Figures S1A and S1B). Forelimb and hindlimb grip strengths and pulled force were also similar in both genotypes (Figures S1C and S1D). Thus, neuromuscular strength and coordination in mice are independent of postnatal *Arx* transcriptional activity in PVIs.

Next, we measured hippocampus-dependent cognitive function using the forward and reverse spatial learning and memory paradigms of the Morris water maze (MWM) test (Simonet et al., 2015). Control and *Arx* CKO mice showed similar performance in the forward and reverse learning phases of the MWM (Figures S2A–S2E). This lack of difference in performance was also noted during the probe or memory test in the form of equal number of crosses for the previous location of the platform during both the recall and purging phases of the probe test (Figures S2F and S2G).

We further probed learning performance using the contextual fear conditioning paradigm (Phillips and LeDoux, 1992) and novel object recognition test (Ennaceur and Delacour, 1988). Control and *Arx* CKO mice showed very low but similar initial freezing ratio prior to the context or foot shock (Figure S2H). Total freezing ratio measured 24 h after the context was also similar in both genotypes (Figure S2I). Similarly, there was no difference in performance between the *Arx* CKO and control mice in the novel object recognition test (Figures S2J and S2K).

As a final measure of adaptive behaviors, we evaluated anxiety using the open field (OF) test (Simonet et al., 2015). Control and *Arx* CKO mice covered equal amount of distance in the OF arena (Figures 3A and 3B), but the *Arx* CKO mice spent significantly less time in the center (Figures 3A and 3C). This reduction in time spent in the center of the arena was noted only for locomotor activity during the second of three 5-min bins, which resulted in a significant reduction in the acclimatization ratio (Figure 3C). This enhancement in anxiety-like behavior was further indicated by a significant increase in fecal counts during the open field test (Figure 3D). To further test anxiety, we performed the elevated plus-maze (EPM) test (Dawson and Tricklebank, 1995) and noted that control and *Arx* CKO mice made similar number of entries into the open and closed arms of the EPM (Figures 3E and 3F). However, the *Arx* CKO mice spent significantly less time in the open arm of the test apparatus (Figures 3E and 3G). Taken together, these results suggest that loss of postnatal *Arx* in PVIs contributes to the expression of anxiety-like behaviors but not cognitive nor motor coordination in *Arx*-linked disorders.

Postnatal loss of *Arx* in PVIs altered their transcriptomic profiles

Loss of function of *Arx* during early embryonic development disrupts genes expression of molecular and cellular processes such as cell migration, axonal guidance, neurogenesis, and regulation of transcription (Fulp et al., 2008). Given the developmental tilt of these pathways, we reasoned that the disrupted pathways underpinning the network and behavioral abnormalities in adult *Arx* CKO mice might be different than the previously described developmentally expressed genes. Therefore, we performed genome-wide expression profiling of FACS-sorted PVIs (PND 35–40). RNA sequencing (RNA-Seq) from cortical and hippocampal TdTom + PVIs from five control and four *Arx* CKO mice resulted in an extensive library of paired reads, which were then mapped to 25K + genes and normalized in DEseq2 (Love et al., 2014). We first assessed the quality of the sequencing data using hierarchical clustering and principal component analysis (PCA) analyses and found a modest separation between control and *Arx* CKO samples (Figures 4A and S3A), reflective of their distinct transcriptomic profiles. Using a modified Bland-Altman (MA) plot, we noted that ablation of *Arx* in PVIs changed the expression of many genes, but only 144 were significantly dysregulated (Figure 4B). Among the differentially expressed genes (DEGs), 28 were upregulated and 116 genes were downregulated (Figure 4B). The epilepsy-related genes *LAMB1, COL18A1, Nid1,* and *DOCK6* (Pisciotta et al., 2018; Radmanesh et al., 2013; Suzuki et al., 2002; Vasudevan et al., 2010) were among the downregulated DEGs (See Table S1 for the full list of DEGs). As hypothesized, we found virtually no overlap between our DEGs and those from embryonic *Arx* deletion (Fulp et al., 2008), proving that the postnatal *Arx* transcriptional regulatory program is distinct from the embryonic brain. To validate the RNA-Seq data, we performed quantitative real-time PCR (qRT-PCR) analysis on *Arx* and 4 DEGs (*Gria3, Olmf1, Cck, and Nid1*) using different biological replicates from the RNAseq analysis. *Arx* was chosen for validation, as it was expected to be reduced in expression in spite of not being a DEG, an observation that is likely due to its low abundance (mean normalized read count = 188) or differential expression of its

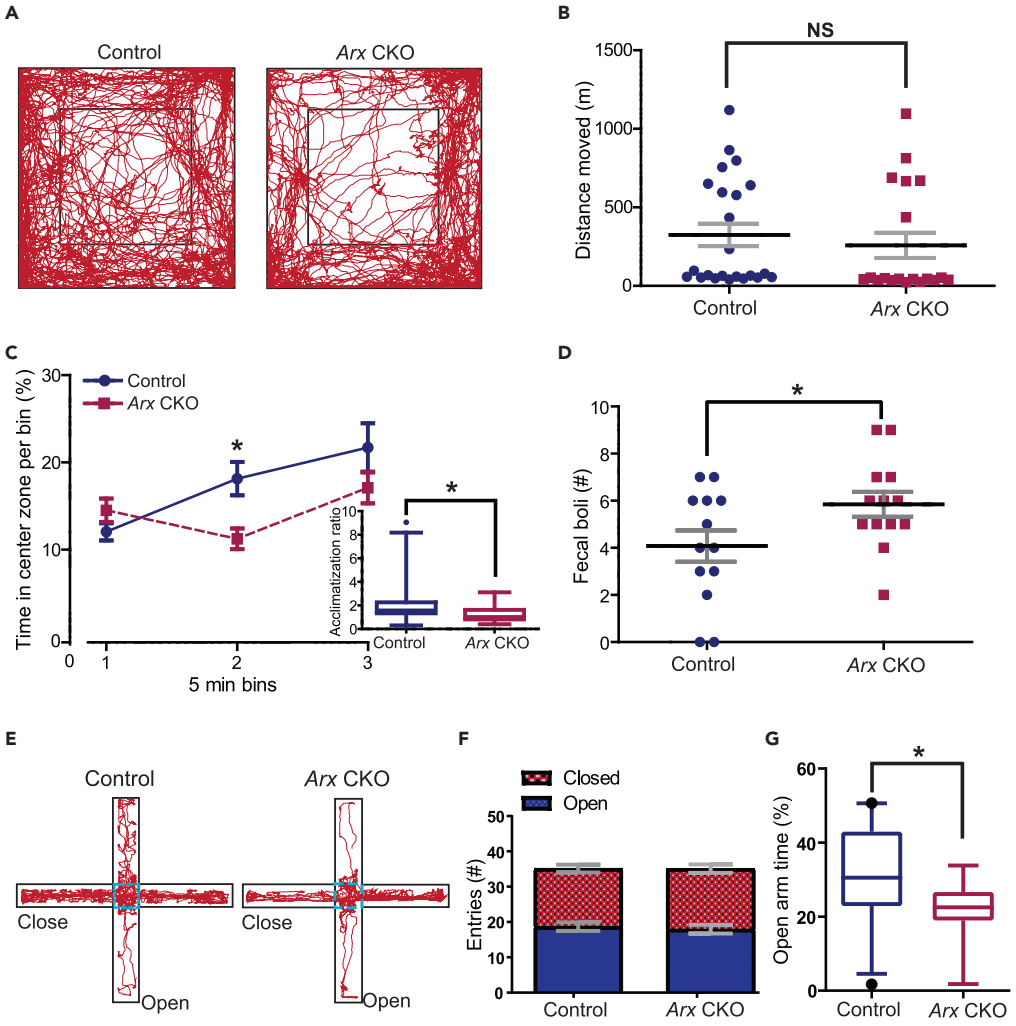

Figure 3. *Arx* CKO mice displayed anxiety-like behaviors

(A) Schematic representation of the zones and a mouse movement in the open field arena. The middle square was taken as the center or anxiety zone.

(B) Total distance traveled was similar in control and *Arx* CKO mice.

(C) Three five-minute bins, showing reduced time in the center of the arena by *Arx* CKO mice (*p < *0.05*). The inset plot of reduced acclimatization ratio measured as the ratio of center time in the second bin over the first bin (*p < *0.05*; Control, *Arx* CKO: n = 23, 19).

(D) Reduced fecal boli number in *Arx* CKO mice (*p < *0.05*, Control & *Arx* CKO: n = 13).

(E) Schematic representation of the EPM used for anxiety test and example traces of a mouse movement in each arm.

(F and G)(F) *Arx* CKO mice made equal amount of entries in the EPM open and close arms but spent less time in the open arms (G, *p < *0.05*, control, *Arx* CKO: n = 23, 19). The lower Q1 and upper Q3 quartiles of box plots (C & F) represent data outside the 5–95 percentile, and dots outside this range denote outliers. Data analyzed by Mann Whitney U test or two-way ANOVA followed by Bonferroni *post hoc* tests (B, C, & F) and by the unpaired, 2-tailed Student's t test (D & G). All data are given as mean ± SEM.

intronic and coding sequences as previously shown (Fulp et al., 2008). Nonetheless, we observed a statistically significant increase in *Gria3* and *Cck* and a decrease in *Arx* as well as *Nid1* (Figure S3B). Although not statistically significant, *Olfm1* mRNA expression also increased more than 2-fold in *Arx* CKO tissues (Figure S3B).

Given the multiplicity of disrupted genes, we choose a biological pathway-based analytical approach to identify the most important molecular and cellular processes underlying the network and behavioral abnormalities in *Arx* CKO mice. To that end, we applied gene ontology (GO) analysis using the Database for

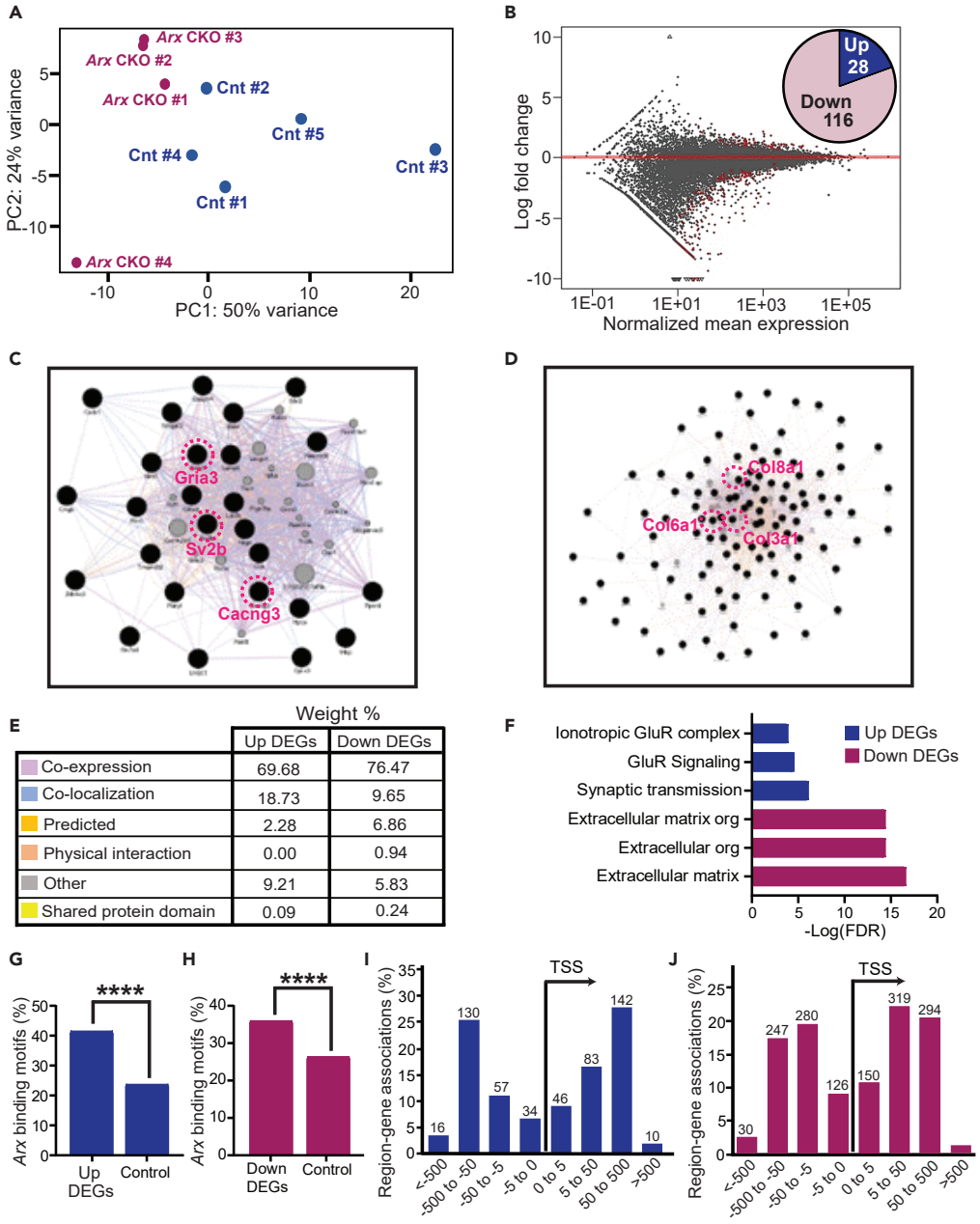

Figure 4. Loss of *Arx* in PVIs altered their transcriptomic profiles

(A) PCA plot showing separation between control and *Arx* CKO biological replicates.

(B) MA plot of DEGs and Venn diagram with the number of up- and downregulated DEGs. Red dots indicate up- and downregulated genes, whereas the black dots indicate non-significant genes based on cut-off criteria (|log2FC| ≥ 1, *FDR* < *0.05*).

(C and D) Functional networks formed by (C) upregulated and downregulated (D) DEGs. Black nodes represent the queried DEGs, and the gray nodes are other genes related to the DEGs.

(E) Percent weight table for each of the functional association networks made by the up- and downregulated DEGs.

(F) Top 3 significantly enriched Gene ontology [$-\log_{10}$ (FDR)] terms associated with functional networks made by DEGs.

(G and H) Open chromatin regions with *Arx*-binding sites were more likely to be found in up- (G) and downregulated (H) DEGs than randomly generated sites (****p < *0.0001*).

(I and J) Upregulated (I) and downregulated (J) DEGs binding motifs were mostly found in distal regions relative to the TSSs. Values on bar graphs represent number of genes associated with peaks in each genomic bin. Transcriptomic data were from 5 control and 4 *Arx* CKO mice. Data analyzed by Benjamini-Hochberg FDR method (B & F) and Chi-square test (G & H).

Annotation, Visualization and Integrated Discovery (DAVID) (Huang da et al., 2009). Separate GO analysis for the upregulated and downregulated DEGs was performed for the enrichment of cellular component. Notably, synapse, α-amino-3-hydroxy-5-methyl-4-isoxazolepropionic acid (AMPA) glutamate receptor complex, and terminal bouton were the top three significant cellular component GO terms associated with the upregulated DEGs (Figure S3C with full table pathways). By contrast, proteinaceous extracellular matrix, extracellular matrix, and collagen fibril organization were the three most significant cellular component GO terms associated with the downregulated genes (Figure S3D). Hence, the prominent biological pathways underpinning network and behavioral abnormalities in *Arx* CKO mice are distinct from those dysregulated following embryonic loss of *Arx*.

Functional gene networks were constructed to identify dysregulated pathways based on co-expression, co-localization, physical interaction, predicted interaction, shared protein domain, and other functional relations using the GeneMANIA cytoscape app (Montojo et al., 2014). In the generated networks, genes/proteins are depicted as dark (Query genes) and gray (Predicted genes) circles and the detected functional relationships between genes/proteins as connecting lines or edges (Figure 4C). Eight genes (2 unregulated, 6 downregulated) among the DEGs were omitted from the constructed networks because they were not recognized by the GeneMANIA-Cytoscape app. Among the rest, the upregulated genes were connected primarily via co-expression networks (69.68%) (Figure 4E) and to a lesser extent via co-localization (18.73%), interaction with predicted genes/proteins (2.28%), shared protein domains (0.09%), and other functional relations (9.21%) (Figure 4E). The downregulated DEGs were also primarily co-expressed together, yielding a co-expression network weight of 76.47% (Figure 4E). The remaining downregulated DEGs were connected via co-localization (9.65%), interaction with predicted genes/proteins (6.86%), physical interactions (0.94%), shared protein domains (0.24%), and other functional relations (5.83%) (Figure 4E). GO analysis of the generated networks that were clustered around synaptic and ECM processes are noted in DAVID (Figures 4F and Tables S2 and S3). These results indicate that postnatal *Arx* expression in PVIs regulates a network of genes widely connected by co-expression and that the upregulated and downregulated genes within its regulatory controls differ in functional network weight, physical interactions, and function. More importantly, the level of significance for the top three GO categories in the network analysis was more profound for the downregulated DEGs compared with the upregulated genes, highlighting the importance of dysregulation of ECM-related gene networks in the production of network and behavioral abnormalities in *Arx* CKO mice.

Gene expression changes identified in our RNAseq could be a consequence, rather than a cause, of the noted network and behavioral abnormalities. To determine whether the expression changes were directly due to loss of *Arx*, we utilized *in silico* analysis. This approach was chosen, as the low *Arx* transcript levels limit direct assessment of binding through cell-specific chromatin immunoprecipitation. Using previously published open chromatin sites in PVIs derived by assay of transposase-accessible chromatin (ATAC), we performed transcription-factor-binding motif (TFBM) enrichment analysis in the 100 kb upstream and downstream of the transcription start site (TSS) of DEGs (Mo et al., 2015). ATAC sequencing is a validated method for identifying the open chromatin signature (Buenrostro et al., 2013). Using Cistrome in combination with the UCSC Table Browser (Karolchik et al., 2004; Liu et al., 2011), we identified a total of 23 of 28 (82.1%) upregulated DEGs (Figure S3E) and 95 of 116 (81.9%) downregulated DEGs (Figure S3F) with at least one overlapping PV-ATAC site and *Arx*-binding motif. A list of DEGs with at least one overlapping PV-ATAC site and *Arx*-binding motif is given in Table S4 (FDR <0.05). The synapse-associated genes *Gria3* and *Sv2b* were among the upregulated DEGs with overlapping PV-ATAC sites and *Arx*-binding motifs (Table S4). The downregulated DEGs with overlapping PV-ATAC sites and *Arx*-binding motifs included the extracellular matrix gene *Col18a1* and *Nid1* (Table S4). To determine if *Arx*-binding motifs were more likely to be present in PV-ATAC sites near DEGs, we first compared the probability of finding an *Arx*-binding motif in PV-ATAC sites in such DEG with randomly generated genomic regions matched for length and percent GC content in RSAT (Nguyen et al., 2018). Our results showed the presence of *Arx*-binding sites in PV-ATAC sites were more likely in the upregulated DEGs than in randomly generated PV-ATAC sites (Figure 4G). *Arx*-binding motifs were also more likely to be found in PV-ATAC sites from downregulated DEGs than in randomly generated matched sites (Figure 4H). We also measured the region-to-gene associations of overlapped PV-ATAC sites and *Arx*-binding motifs using the Genomics Region of Enrichment Analysis Tool (GREAT) (McLean et al., 2010) and noted that less than 10% of such association for upregulated (Figure 4I) and downregulated (Figure 4J) DEGs occurred within 5 Kb of the annotated TSSs. By contrast, there was a clear tendency for this PV-ATAC sites/*Arx* motifs association for upregulated and downregulated

DEGs to be confined to regions distant from the annotated TSSs (Figures 4I and 4J). These results indicate that *Arx*-binding motifs in the postnatal brain are enriched at putative enhancers of both up- and downregulated DEGs. Thus, *Arx* regulatory roles in postnatal gene regulation might be as a secondary modulator of gene expression through binding at distal enhancers instead of a primary and necessary driver of transcription mediated through binding at proximal enhancers (Lenhard et al., 2012).

Arx ablation disrupted the perineuronal nets around PVIs

ECM-related genes are important in the development and maturation of neural circuits (Stranahan et al., 2013). Therefore, we asked whether the profound downregulation of ECM-regulated genes in PVIs resulted in structural alterations. We first assessed the density of PVIs using conventional immunolabeling techniques. We found that the density of PVIs was not altered in *Arx* CKO mice (Figures 5A and 5B). To rule out non-cell autonomous effects on the other GABAergic interneurons, we measured the density of hippocampal SST, CB, and CR GABAergic interneuron subtypes and found no differences (Figure 5B). To further assess structural alterations, we investigated whether the loss of *Arx* in PVIs led to molecular changes in the perineuronal nets (PNNs), an ECM specialization that consists of proteoglycans such as aggrecan (ACAN) and generally wraps PVIs (Giamanco and Matthews, 2012). Using immunolabeling techniques, we observed a marked reduction in the intensity of the aggregating proteoglycans marker ACAN (Figures 5C and 5E) and a substantial decrease in the number of the glycosylated ACAN marker Cat-315 (Figures 5D and 5F) throughout the hippocampus of *Arx* CKO mice. As expected, co-labeling of TdTom and Cat-315 showed that PVIs are preferentially wrapped by the PNNs in control mice, but this structural relationship appears to be disrupted in *Arx* CKO mice as evidenced by the profound reduction in the number of TdTom + cells surrounded by Cat-315 (Figures 5D and 5G).These results further confirm the RNA-Seq GO analysis and establish an important role for postnatal *Arx* signaling in the structural maintenance of PVIs in neural circuits.

Reduced membrane excitability of PVIs in *Arx* CKO mice

The PNN has been shown to be a potent regulator of neuronal excitability (Balmer, 2016; Dityatev et al., 2007; Favuzzi et al., 2017; Lensjo et al., 2017), raising the possibility that the loss of PNN around PVIs from *Arx* CKO mice may have altered the intrinsic excitability of these interneurons. To test this possibility, we recorded intrinsic membrane properties of PVIs from the first Cornu Ammonis (CA1) region of the hippocampus in whole-cell current clamp mode. Passive intrinsic membrane properties were not significantly affected by the loss of *Arx* (see Table S5 for values of resting membrane potential, capacitance, input resistance, and membrane time constant). Similarly, action potential properties measured from the initial spike evoked by the rheobase current (Figure 6A) were indistinguishable between genotypes with regard to amplitude, duration at half amplitude, and fast afterhyperpolarization potential (AHP) (Table S5). However, the rheobase current amplitude required to evoke this initial action potential (AP) was significantly higher in PVIs from *Arx* CKO mice (Figure 6B). In addition, the membrane threshold for the initial AP firing was more depolarized in these PVIs (Figure 6C). These hypo-excitability measures were associated with much slower onset latencies for the initial APs (Figure 6D). Trains of APs triggered by 500 ms depolarizing current steps in both *Arx* CKO and control mice were relatively brief in duration and occurred at high frequency with very low adaptation ratio (Figure 6E), suggesting that PVIs that underwent Cre-recombination in both genotypes still exhibited major physiological hallmarks of wild-type fast-spiking PVIs (Kuhlman and Huang, 2008; Rudy and McBain, 2001). However, the number of APs generated by a given 500ms current step was significantly reduced in PVIs from *Arx* CKO mice (Figure 6F), indicating that ablation of *Arx* in PVIs alters their steady state firing properties. These results suggest that postnatal *Arx* transcriptional activity is an important regulator of intrinsic membrane properties of PVIs.

Dendritic complexity of PVIs is intact in Arx CKO mice

The hypo-excitability measures in PVIs from *Arx* CKO mice could depend on the types and density of voltage-gated ion channels over the neuronal membrane (Migliore and Shepherd, 2005) or altered complexity of their dendrites (van der Velden et al., 2012). Given that our RNA-Seq data revealed a lack of prominent dysregulation of voltage-gated ion channels, we measured dendritic complexity using Sholl analysis (Sholl, 1953). Quantitative analysis of biotin-labeled PVIs in the hippocampal CA1 region did not reveal any significant differences in dendritic complexity as measured by number of intersections, branch number, and maximum branch length in Sholl concentric circles near or distant from the soma (Figures S4A–S4D). Thus, these results suggest that dendritic morphology did not substantially contribute to PVI or overall CA1 network excitability.

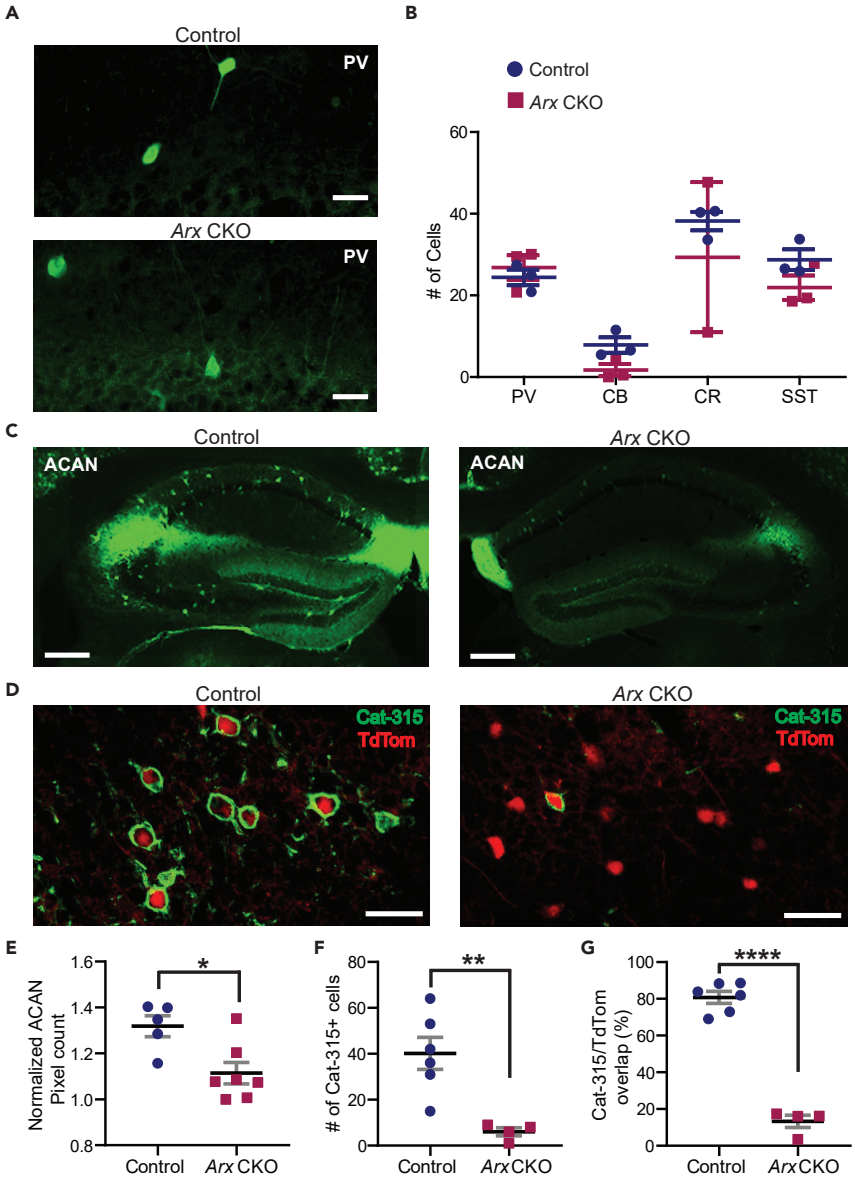

Figure 5. Perineuronal nets are disrupted around PVIs in *Arx* CKO mice without altering the density of GABAergic interneurons

(A) Representative images of PV immunolabeling in the hippocampus of control (Top) and *Arx* CKO (Bottom) mice.

(B) Density of PV, CB, CR, and SST GABAergic interneurons per mm^2 in the CA1 hippocampus was comparable in both genotypes ($p > 0.05$; two-way ANOVA; control, *Arx* CKO: N = 3).

(C and D) Representative images of aggrecan (C, ACAN) and Cat-315/TdTomato co-labeling in the hippocampus of control (Left) and *Arx* CKO mice (Right) (D).

(E–G)ACAN intensity was reduced in *Arx* CKO mice (E, *$p < 0.05$; unpaired 2-tailed Student's t test; control = 5 and *Arx* CKO = 7). Quantitative analysis of Cat-315 + neurons per mm^2 revealed a significant reduction in the density (F, **$p < 0.01$; inpaired 2-tailed Student's t test; control = 6 and *Arx* CKO = 4) and in the number of neurons with overlapping expression of this marker with TdTom (G, ****$p < 0.0001$; unpaired, 2-tailed Student's t test; Control = 6 and *Arx* CKO = 4). Data are given as mean ± SEM (B). Scale bars: (A) 25 μm, (C) 50 μm, (D) 100 μm.

Reduced spontaneous synaptic excitability in PVIs

Brain oscillations are thought to emerge through an interactive interplay between intrinsic membrane and synaptic properties (Benayoun et al., 2010). Thus, we reasoned that the hypo-excitability of PVIs in *Arx* CKO mice could be accompanied by alterations in synaptic excitability. To measure synaptic excitability, we

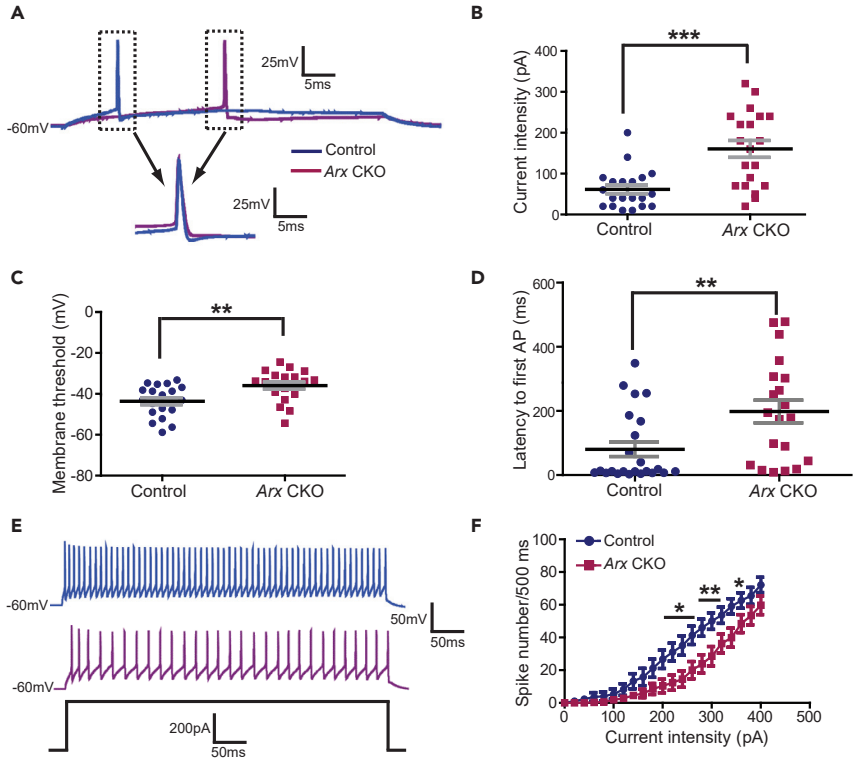

Figure 6. Intrinsic membrane properties of PVIs are altered in *Arx* CKO mice

(A) Representative rheobase spikes recorded on PVIs.

(B–D) PVIs in *Arx* CKO mice were hypoexcitable based on higher rheobase current (B, ***p < *0.001*; control & *Arx* CKO: n = 20/12, cells/mice), more depolarized AP threshold (C, **p < *0.01*; control & *Arx* CKO: n = 20/12, cells/mice), and delayed latency to rheobase spikes (D, **p < *0.01*; control: n = 23/12, *Arx* CKO: n = 20/12, cells/mice).

(E) Representative spikes at maximal depolarizing current injection.

(F) PVI steady state spike frequency was reduced in *Arx* CKO mice (p < *0.0001*; control: n = 16/10, *Arx* CKO: n = 20/10, cells/mice). *Symbols in F denote post hoc test significance levels: *p < *0.05*, **p < *0.01*. Data are given as mean ± SEM and analyzed by the unpaired, 2-tailed Student's t test (B & C), Mann Whitney U test (D), or two-way ANOVA followed by Bonferroni post hoc tests (F).

simultaneously recorded spontaneous excitatory postsynaptic currents (sEPSCs) and inhibitory postsynaptic currents (sIPSCs) on PVIs at a holding potential of −40mV in aCSF free of glutamate and GABA receptor blockers (Zhou et al., 2009). The inward sEPSC onto PVIs appeared as rapidly rising and slowly decaying currents, whereas the rise and decay kinetics of the outward IPSCs currents were slower as previously described (Figure 7A) (Wuarin and Dudek, 1993). There was a reduction in the mean frequency of spontaneous EPSCs onto *Arx* CKO PVIs (Figure 7B) as well as a rightward shift of the cumulative probability curve for inter-event intervals (Figure 7B). Although the mean sEPSC amplitude was similar in both genotypes, there was a shift toward larger sEPSC events in their cumulative distribution in *Arx* CKO mice (Figure 7C).

Analysis of sIPSCs also revealed a significant rightward shift in the cumulative probability of inhibitory inter-event intervals, reflecting a reduction in the frequency of sIPSCs (Figure 7D). However, the mean frequency of these sIPSC did not differ between genotypes (Figure 7D). Analysis of sIPSCs also showed no significant differences in mean events amplitude nor in their cumulative distribution in *Arx* CKO and control mice (Figure 7E). As expected from the lack of changes in EPSC and IPSC amplitudes, their mean amplitude ratio was not altered in *Arx* CKO mice (Figure 7F). These results support a role for transcriptional activity of postnatal *Arx* in the regulation of some spontaneous excitatory and inhibitory synaptic properties in PVIs.

Alterations in miniature synaptic transmission onto PVIs

To measure the contribution of network activity to the changes in spontaneous synaptic transmission onto PVIs in the CA1 hippocampal region, we recorded miniature EPSCs (mEPSCs) and IPSCs (mIPSCs) in the

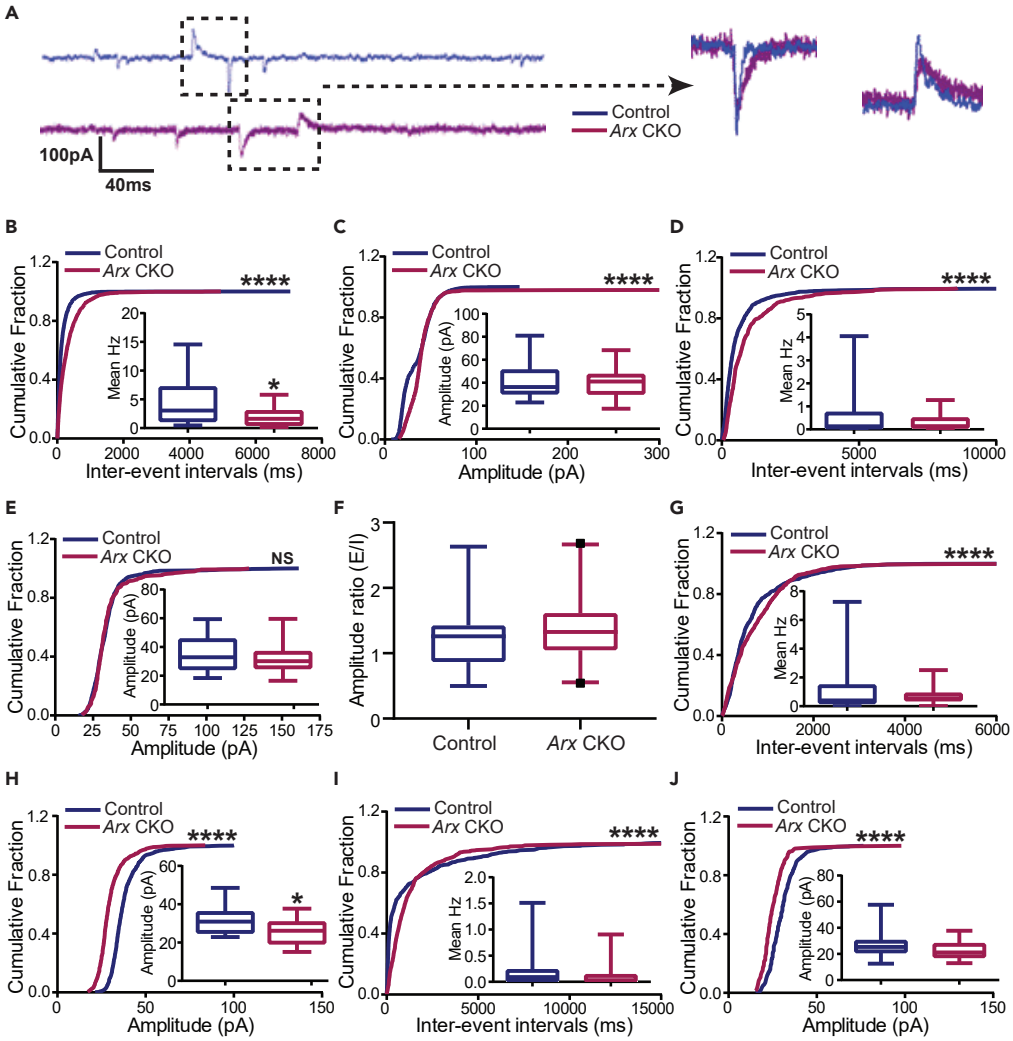

Figure 7. Impaired spontaneous synaptic transmission

(A) Example traces of sEPSCs and sIPSC recorded on PVIs in the CA1 hippocampus of control and *Arx* CKO mice.

(B) Reduced sEPSC frequency onto PVIs in *Arx* CKO mice (Cumulative and box plots: ****p < *0.0001*, *p < *0.05*; control: n = 16/10, *Arx* CKO: n = 20/12, cells/mice).

(C) Cumulative amplitude shifted toward larger events without affecting the mean (cumulative and box plots: ****p < *0.0001*, p > *0.05*; control: n = 16/10, *Arx* CKO: n = 20/12, cells/mice).

(D) The cumulative frequency of sIPSCs shifted toward less events without any effects on their mean frequency (cumulative and box plots: ****p < *0.0001*, p > *0.05*; control: n = 17/11, *Arx* CKO: n = 21/12, cells/mice).

(E) Cumulative distribution and mean of sIPSC amplitude are normal in *Arx* CKO mice (cumulative and box plots: p > *0.05* for both graphs; control: n = 14/10, *Arx* CKO: n = 19/12, cells/mice).

(F) Ratio of excitatory to inhibitory amplitudes was not altered (p > *0.05*; Control: n = 17/10, *Arx* CKO: n = 18/12, cells/mice).

(G) A shift toward less excitatory events (mEPSCs) was still evident in presence of TTX with no effects on the mean frequency (cumulative and box plots: ****p < *0.0001*, p > *0.05*; control: n = 20/12, *Arx* CKO: n = 17/12, cells/mice).

(H) Cumulative distribution of mEPSC amplitudes shifted toward smaller events as reflected in the mean amplitude (cumulative and box plots: ****p < *0.0001*, *p < *0.05*; Control & *Arx CKO:* n = 17/12, cells/mice).

(I) Biphasic cumulative distribution mIPSC frequency with no effects on the mean (cumulative and box plots: ****p < *0.0001*, p > *0.05*; Control: n = 15/10, *Arx* CKO: n = 11/10, cells/mice).

(J) Cumulative distribution of mIPSC amplitudes shifted toward larger events with no effects on the mean amplitude (cumulative and box plots: ****p < *0.0001*, p > *0.05*; control: n = 19/12, *Arx* CKO: n = 17/12, cells/mice). Data are given as mean ± SEM and analyzed by the K-S (cumulative plots) or the unpaired, 2-tailed Student's t (Box plots) tests.

presence of 0.5μM tetrodotoxin (TTX). In contrast to sEPSC, quantitative analysis of mEPSCs showed no significant differences in mean frequency of excitatory events between *Arx* CKO and control mice (Figure 7G). However, similar to the sEPSCs, the cumulative probability curve of mEPSCs inter-event intervals shifted toward less frequent events in *Arx* CKO mice compared with controls (Figure 7G). In contrast to sEPSCs, the mean amplitude of mEPSCs recorded on PVIs from *Arx* CKO mice was significantly reduced compared with controls, and this observation was consistent with a leftward shift toward smaller events in their cumulative distribution (Figure 7H).

The mean frequency of the mIPSCs in *Arx* CKO mice was not statistically different from controls (Figure 7I). Analysis of the cumulative distribution of mIPSCs inter-event intervals showed a biphasic curve, with a cluster of events shifted leftward toward more frequent events and another shifted rightward toward less frequent events (Figure 7I). The mean amplitude of mIPSC events revealed that *Arx* CKO mice were indistinguishable from control mice, but the cumulative distribution of those events shifted toward larger mIPSCs (Figure 7J). These results suggest that loss of *Arx* in PVIs was primarily associated with changes to excitatory synaptic properties, including a reduction in EPSC mean frequency as well as significant changes in the cumulative distribution of sEPSC/sIPSC IEI and amplitude. Many of these changes were either blunted or reversed by the addition of TTX, suggesting *Arx*-mediated alterations in synaptic drives onto PVIs might be influenced by intrinsic properties of presynaptic cells and/or network excitability.

Loss of *Arx* reduced evoked excitatory drive onto PVIs

The quantitative analysis of mEPSCs and mIPSCs on PVIs are mostly consistent with a reduction in synaptic excitability. To further strengthen this conclusion, we measured the input-output (I-O) relationship of whole-cell evoked EPSCs (eEPSCs) and IPSCs (eIPSCs) on PVIs in response to Shaffer collateral (SC) stimulation (Figure 8A). We found that the I-O relationship of the eEPSC amplitude was reduced in *Arx* CKO mice (Figure 8B). This reduction in synaptic transmission was further manifested in a reduction in charge transfer and decay kinetics (Figures 8C and 8D). By contrast, eIPSC I/O relationship for amplitude, charge transfer, and decay kinetics revealed no differences between genotypes (Figures 8E–8G). However, the ratio of eEPSC/eIPSC amplitudes onto PVIs in *Arx* CKO mice was reduced (Figure 8H), indicating a shift toward less excitation.

The reduction in synaptic excitability of CA1 PVIs following the postnatal loss of *Arx* could arise from alterations in the pre-synaptic machinery. Therefore, we recorded whole-cell patch paired pulse responses (PPR) in PVIs at SC-CA1 synapses (Figures 8I and 8J). We found that the ratio of eEPSC PPR recorded on *Arx* null PVIs was unchanged relative to controls (Figure 8I), suggesting that *Arx*-mediated impairments in evoked excitatory transmission were independent of presynaptic defects. The eIPSC PPR in *Arx* CKO was indistinguishable from control mice (Figure 8J), a consistent observation with the lack of change in inhibitory synaptic drive onto in PVIs. Taken together, these results indicate that network hyperexcitability in *Arx* CKO mice was driven primarily by a reduction in SC drive onto PVIs that was independent of the presynaptic release machinery.

Postsynaptic glutamate receptors hypofunction contributes to reduced synaptic excitability

Given that PPR of eEPSCs and dendritic complexity were unaltered in PVIs from *Arx* CKO mice, we reasoned that the reduction in synaptic excitability could arise from alterations in the function of postsynaptic glutamate receptors (GluRs). We measured mixed AMPA and N-Methyl-D-aspartic acid or N-Methyl-D-aspartate (NMDA) eEPSCs in response to SC stimulation and characterized the AMPA and NMDA components of those EPSCs with respect to their conductance, rectification patterns, and functional ratio. Examination of the I-V relationship for both AMPA- and NMDA-receptor-mediated currents at different holding potentials revealed considerable inward rectification in both genotypes, but this rectification behavior appears to be more moderate in *Arx* CKO mice (Figures 9A–9C). Accordingly, the rectification index (RI), defined as the ratio of current amplitude at +50 and −50 mV, for both AMPA and NMDA receptor currents was significantly reduced in PVIs from *Arx* CKO mice (Figures 9D and 9E). This suggests that excitatory synapses on PVIs were more likely to be activated via Ca^{2+} impermeable GluRs. A caveat, however, is that the recorded reversal potentials of AMPA and NMDA receptor currents were different from their expected 0 mV value (Suyama et al., 2017). Although several factors could account for this discrepancy, poor space clamp error may have largely contributed to this error in voltage. Because this error could potentially affect the accuracy of the RI of AMPA and NMDA receptors, we limited our analysis to cells that did not substantially differ from their reversal potentials to ensure that space clamp errors were evenly distributed

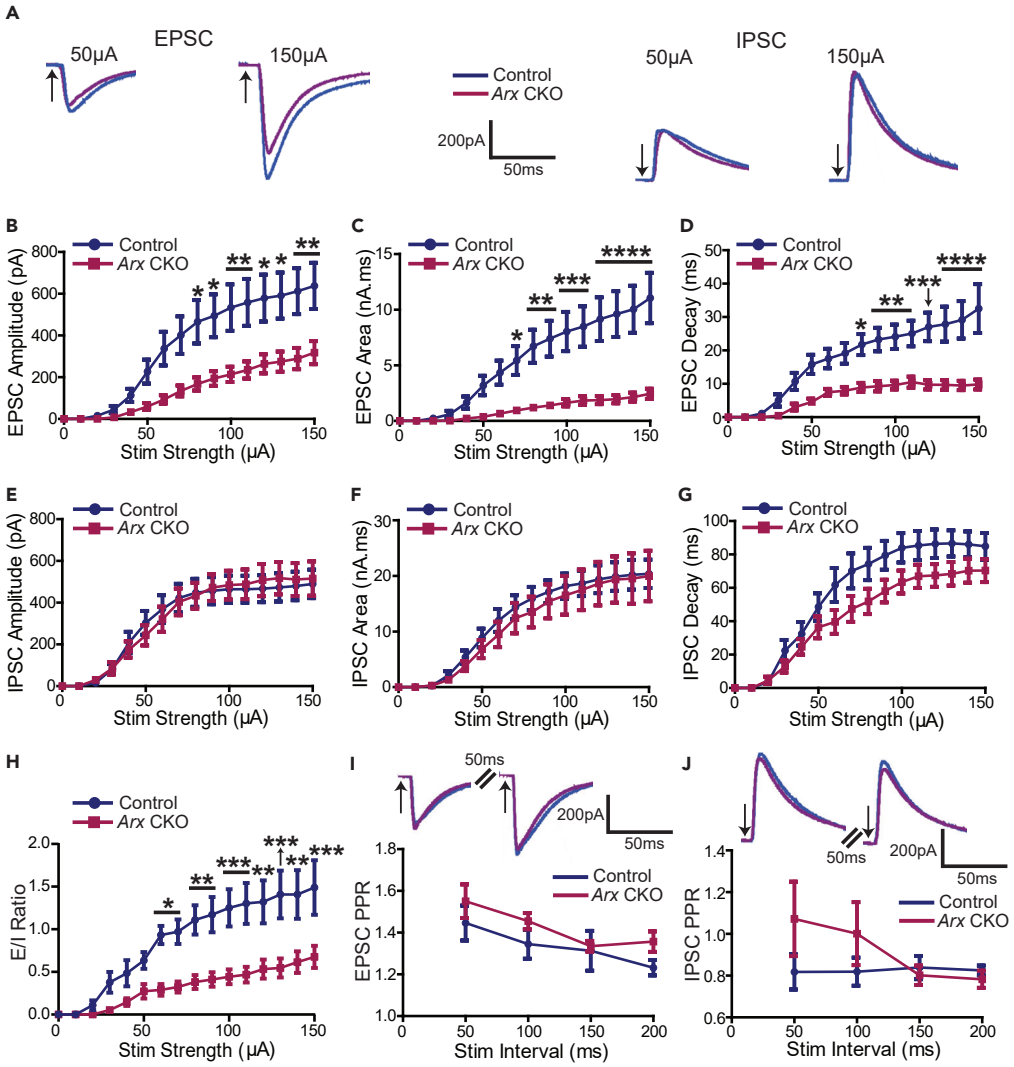

Figure 8. PVIs in *Arx* CKO mice are synaptically hypoexcitable

(A) Representative traces of EPSC and IPSC evoked by SC stimulation in the CA1 hippocampal region.

(B–D) I/O curves for eEPSC amplitude (B), area under the curve (C), and decay kinetics (D) revealed a profound reduction in excitatory drives onto PVIs ($p < 0.0001$; control: n = 19 cells/10 mice, *Arx* CKO: n = 18 cells/12 mice).

(E–G) Evoked inhibitory drive is normal as shown in I/O curves for eIPSC amplitude (E), area under the curve (F), and decay kinetics (G) ($p < 0.0001$; control: n = 24/12, *Arx* CKO: n = 21/12, cells/mice).

(H) The ratio of excitatory to inhibitory of the I/O curves shifted toward less excitation in *Arx* CKO mice ($p < 0.0001$; control: n = 11/8, *Arx* CKO: n = 10/8 cells/mice).

(I and J) The paired-pulse ratio for both eEPSC (I) and eIPSC (J) was normal in *Arx* CKO mice ($p > 0.05$; control: n = 17/12, *Arx* CKO: n = 16/10, cells/mice for both EPSC and IPSC PPR). Representative paired-pulse traces above graphs were recorded at interval of 50 ms. Data are given as mean ± SEM and analyzed by two-way ANOVA followed by Bonferroni post hoc tests. *Symbols denote post hoc test significance levels: *$p < 0.05$, **$p < 0.01$, ***$p < 0.001$, ****$p < 0.0001$.

across genotypes. Of note, the RI values were consistently lower in *Arx* CKO PVIs compared with controls irrespective of differences in reversal potentials, confirming the accuracy of our RI data.

To further elucidate the synaptic mechanisms of reduced excitatory drive to PVIs, we measured the ratio of AMPA/NMDA receptors. As expected, based on the RI measurements, the AMPAR/NMDA receptor current ratio was significantly reduced in PVIs from *Arx* CKO mice compared with controls (Figures 9F and 9G), further supporting the postsynaptic basis of eEPSC impairments noted in PVIs following the loss of *Arx*. Taken together, these results suggest that the synaptic basis of network and behavioral abnormalities

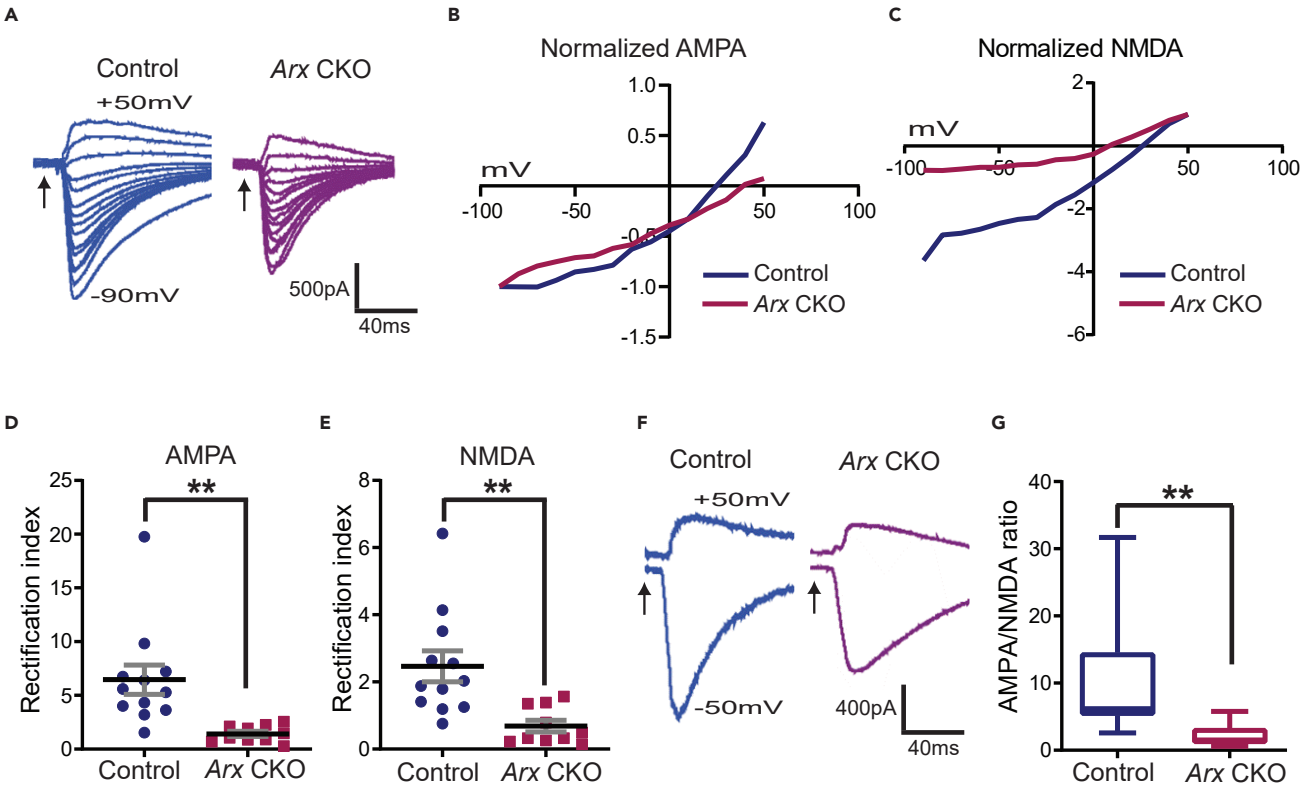

Figure 9. Impaired functional properties of AMPA and NMDA receptors in *Arx* CKO mice

(A) Representative traces of mixed AMPA- and NMDA-receptor-mediated currents on PVIs evoked by SC stimulation in the CA1 hippocampal region.

(B–E) (B and C) I–V curves of AMPA- (B) and NMDA-receptor (C)-mediated conductance normalized to highest respective current. (C and D) Reduced AMPA (D; **p < *0.01*; control: n = 12/8, *Arx* CKO: n = 10/8, cells/mice) and NMDA (E; **p < *0.01*; **p < *0.01*; control: n = 12/8, *Arx* CKO: n = 10/8, cells/mice) receptor RI onto PVIs.

(F) Representative traces of AMPA- and NMDA-receptor-mediated EPSCs recorded at −50 mV and +50 mV, respectively.

(G) Reduced ratio of AMPAR/NMDAR currents onto PVIs in *Arx* CKO mice (**p < *0.01*; **p < *0.01*; control: n = 12/8, *Arx* CKO: n = 10/8, cells/mice). Data are given as mean ± SEM and analyzed by the unpaired, 2-tailed Student's t test.

in *Arx* CKO mice can be attributed primarily to a reduction in excitatory synaptic drive onto PVIs as a result of dysregulation of postsynaptic GluRs.

DISCUSSION

Loss of function of *Arx* during embryonic development leads to defects in migration of interneurons, epilepsy, and cognitive deficits. ARX remains expressed in mature interneurons, with an unknown function and relationship to disease progression. We addressed this important question by ablating postnatal *Arx* expression exclusively in the PVIs and noted an increase in EEG theta oscillations, occasional spontaneous seizures, and behavioral abnormalities. RNAseq analysis suggests that these network effects were likely due to dysregulation of coherent set of genes, with those related to the ECM as the central hub of dysregulated pathways underlying the network abnormalities. The cellular and synaptic mechanisms mediating these network effects appear to involve a profound reduction in excitability of intrinsic and synaptic properties onto PVIs. Therefore, our results place *Arx* in PVIs at nexus of a broad set of genes essential for sculpting as well as maintaining mature neural networks and dysfunction in those roles contributes to the pathologic mechanisms of *Arx*-linked EEOEs.

Seizures and other network abnormalities are important clinical manifestations of EEOEs (Nordli, 2012; Shoubridge et al., 2010). We found a selected increase in theta oscillations and rare electrographic seizures following the postnatal loss of *Arx* in PVIs. An alteration in theta oscillations was expected, given previous reports of tight coupling of PVI excitability with both theta and gamma oscillations (Amilhon et al., 2015;

Carlen et al., 2012; Gonzalez-Burgos and Lewis, 2008). Our findings were unexpected, as they are in the opposite direction of previous studies that demonstrated reduced theta rhythms following optogenetic silencing of activity of PVIs or hypoexcitability induced by selective reduction of NMDAR function in these cells (Amilhon et al., 2015; Carlen et al., 2012; Korotkova et al., 2010). This discrepancy could be due to a variety of experimental and biological factors. First, the level of PVI dysfunction due to *Arx* dysregulation and optogenetic stimulation is very different resulting in different effects on theta oscillations. Second, the subtype of PVIs altered could lead to activation of distinct oscillatory generators (Colgin, 2013) shifting theta rhythms distinctly. Third, the lack of effect on gamma and enhanced theta oscillations may represent functional features of hippocampal circuits disposed to spontaneous, albeit sporadic, seizures in *Arx* CKO mice as a result of selective disruption of an important postnatal transcriptional regulator of neural circuits. Future studies are needed to determine whether the regulation of gamma rhythms and the direction of theta modulation in hypoexcitable PVIs are contingent on whether signaling dysfunctions mediating hypoexcitability of these cells lead to neural circuits disposed to spontaneous seizures.

The presence of occasional spontaneous seizures (2/12) compared with the regularity of seizures in the $Arx^{-/Y}$; Dlx5/6CIG mouse line (100%) where deletion occurs embryonically and includes all interneurons (Marsh et al., 2009) could be due to the following: (1) our 3-day EEG recordings being an insufficient time to capture infrequent seizures; (2) variable Cre recombination in the *Arx* CKO mice could have influenced seizure threshold and, thus, reduced the frequency of spontaneous seizures; and (3) complete penetrance of reduced threshold for spontaneous seizures may require postnatal *Arx* dysfunction in all interneurons or in combination with different interneuron subtypes. Interestingly, occasional rather than regular seizures were also noted in another CKO mouse model in which *Scn1a* (NaV1.1) was ablated in PVIs (Ogiwara et al., 2013), suggesting that the threshold for the development of more regular seizures may require both pre- and postnatal effects on PVIs. Thus, it will be important to determine how dysfunction in postnatal *Arx* signaling in other interneurons, either alone or in concert, contribute to spontaneous seizures in future studies. Nonetheless, our results confirm the essential role of PVIs in network oscillations (Amilhon et al., 2015) and show that postnatal dysfunction in *Arx* transcriptional activity in PVIs alone can contribute to the pathophysiology of EEOEs.

Diminished cognitive and adaptive behaviors are core features of the Intellectual disability described in EEOEs (Verma et al., 2019). To that end, we assessed the performance of *Arx* CKO and control mice in behaviors within the cognitive, motor, and anxiety domains. Interestingly, we only found a behavioral phenotype within the anxiety domain in the *Arx* CKO mice. More specifically, the mutant mice exhibited an increase in anxiety-related behaviors, an observation that is well correlated with the enhanced theta oscillations in these mice, given the direct relationship between the magnitude of these rhythms and anxiety-provoking environments (Gordon et al., 2005). Although the expression of anxiety-like behaviors was consistent across the OF and EPM tests used in this study, this phenotype was apparent in the time spent in the open arm of the EPM but not in the number of entries into the open and closed arms, suggesting that *Arx*-dependent activity in PVIs mediates the expression of anxiety-like behaviors as opposed to a general effect on activity levels. Indeed, the anxiety phenotype in the OF was noted without any discernible differences in activity levels of control and *Arx* CKO mice. Although control and *Arx* CKO mice display similar levels of spontaneous activity in the OF, our quantification of spontaneous activity levels are lower than others have reported (Bolivar et al., 2000; Bothe et al., 2005; Miller et al., 2010; Moy et al., 2007; Sik et al., 2003). Similarly, both genotypes displayed low exploration activity in the NOR test (Bolivar et al., 2000; Bothe et al., 2005; Miller et al., 2010; Moy et al., 2007; Sik et al., 2003). Although we cannot fully explain these differences, environmental factors such as noise, temperature changes, and housing are known to impact levels of exploration and spontaneous activity in mice (Van Meer and Raber, 2005). Alternatively, the difference in these behaviors may be explained by the 129P2/OlaHsd x 129S6/SvEvTac x C57BL/6J hybrid background of our mice. Genetic variability across inbred strains exists in most behavioral tests, including those for cognitive and emotional disorders (Van Meer and Raber, 2005). In particular, the 129S1 strain, an important contributor to the hybrid background strain in this study, has consistently been shown to display low levels of spontaneous and exploratory activity in OF and NOR tests, respectively (Bolivar et al., 2000; Bothe et al., 2005; Miller et al., 2010; Moy et al., 2007; Sik et al., 2003).

Previous reports have stated that anxiety or emotional stress can impair spatial learning and memory (Goodman and McIntyre, 2017; Packard and Wingard, 2004). Thus, we were surprised by the lack of effects on spatial learning and memory in the *Arx* CKO mice in light of the increased anxiety-like behaviors in these mice. This

is particularly interesting given the association of spatial performance in the early stages of the MWM to anxiety or thigmotaxic behavior in mice. Although increase in thigmotaxic behavior in *Arx* CKO mice was evident in the OF test, analysis of path efficiency and distance traveled to the escape platform did not reveal any differences in the expression of such behavior at any point during the MWM test. These differences in the two paradigms are likely due to context-dependent expression of fear (Van Meer and Raber, 2005).

The selective impairments of anxiety in the *Arx* CKO mice among the three behavioral domains tested in this study is consistent with the previously described relationship between alterations in the functional properties of PVIs and manifestation of cognitive and motor deficits relevant to neurodevelopmental disorders (Hu et al., 2014). Notably, alterations in the neurotransmitter release properties of PVIs by deletion of the Glutamic acid decarboxylase 67 gene or in their excitability by genetic deletion of ion channels such as NMDARs, GluR1, metabotropic GluR5, and the sodium voltage-gated channel alpha subunit 1 (SCN1A) have led to variable cognitive and spontaneous activity phenotypes from significantly affected to indistinguishable from controls (Billingslea et al., 2014; Carlen et al., 2012; Fuchs et al., 2007; Korotkova et al., 2010; Saunders et al., 2013). Our results suggest that anxiety-like behaviors are among the emergent behavioral phenotypes from mice with dysfunctional PVIs and that their manifestation may be primarily related to postnatal alterations in the functional properties of these cells. Although this selective anxiety phenotype in our postnatal *Arx* CKO model is interesting, it is in contrast to the diverse adaptive behavioral deficits in various *Arx* mutant mice (Dubos et al., 2018; Jackson et al., 2017; Kitamura et al., 2009; Price et al., 2009; Simonet et al., 2015). These discrepant observations are likely due to differences in prenatal and postnatal *Arx* roles and/or the number/type of interneuron subtypes where *Arx* is dysregulated. Nonetheless, our present results demonstrate that loss of *Arx* transcriptional activity in maturing PVIs alone can lead to anxiety-related behaviors commonly noted in EOEEs.

To understand the molecular determinants of the network and behavioral abnormalities in *Arx* CKO mice, we assessed the transcriptomic profiles of PVIs and found dysregulation of a diverse and broad set of genes. Except for Calb1, these deregulated genes did not overlap with DEGs following embryonic deletion of *Arx* (Fulp et al., 2008), suggesting that the postnatal *Arx* transcriptional program mostly diverged from its embryonic counterpart. Interestingly, *Arx* was not among our DEGs, but qPCR analysis of its expression revealed a significant reduction as expected. The basis for the incoherence between the DEG and qPCR analyses with respect to *Arx* could be due to a number of factors. First, low *Arx* read counts in the RNAseq could have diminished the accuracy of quantifying *Arx* expression (Lozoya et al., 2018). Second, P35-40 total RNA from FACS sorted *Arx* null PVIs used for genome-wide expression profiling may have been contaminated with slowly degrading mRNA transcribed prior to recombination at ~ P15. Thus, it may be advantageous in the future to isolate RNA from *Arx* CKO models in older mice to mitigate the possible impact of slowly degrading *Arx* mRNA on transcriptomic profiling studies. Third, high GC content of *Arx* could have severely limited the efficiency of *Arx* sequencing (Dohm et al., 2008). Fourth, our flox/flox excision approach to generate nonfunctional ARX could have excluded and/or included regulatory elements that differentially affected the stability of the generated *Arx* RNA. In that context, it is worth noting that conditional ablation of *Arx* in the embryonic brain resulted in both upregulated and downregulated *Arx* expression in microarray analysis (Fulp et al., 2008). Interestingly, the upregulated signal was associated with the coding sequence or cDNA, whereas the downregulated signal was associated with a small segment of Intron 1 of the *Arx* genome rather than spliced RNA. Future studies are needed to sort out the regulatory mechanism that ultimately controls *Arx* RNA stability. Nonetheless, our qPCR results generally support the RNA-seq analysis and demonstrated a clear reduction in *Arx* expression in PVIs.

Given the diversity and number of altered DEGs in *Arx* CKO mice, we used bioinformatics approaches to identify the biological pathways that DEGs converged upon and those most essential for the production of *Arx* CKO network abnormalities. The low *Arx* expression in the mature brain necessitated this approach, as its low abundance would be a major obstacle to ChIP-Seq and other biochemical functional analyses. We found that upregulated DEGs were particularly involved in synaptic pathways, whereas the downregulated DEGs were mostly involved ECM-related pathways. More importantly, both the up- and downregulated DEGs were primarily connected via co-expression networks with many of these DEGs having putative *Arx*-binding motifs. These motifs were found in an overwhelming number of ECM-related genes in the downregulated DEGs, suggesting that *Arx* preferentially binds to ECM genes, making them the likely locus of the hub pathways that led to network abnormalities in *Arx* CKO mice. Generation of epitope-tagged *Arx* will enable the production of supporting empirical evidence to validate this conclusion. Nevertheless, it is

worth noting that our analyses revealed that the postnatal loss of *Arx* in PVIs led to the downregulation of proven epilepsy-related genes such as *LAMB1*, *COL18A1*, *Nid1*, and *DOCK6* (Pisciotta et al., 2018; Radmanesh et al., 2013; Suzuki et al., 2002; Vasudevan et al., 2010). Thus, these ECM-related DEGs are likely to be causally relevant to the noted network abnormalities in *Arx* CKO mice.

Central to our RNAseq observations is the preponderance of ECM-associated genes in the DEGs and the identification of several epilepsy causal genes within that group. Consistent with the profound dysregulation of ECM components, we demonstrated a marked reduction in ACAN and a significant loss of Cat-315, suggesting a disruption in the molecular integrity of the PNN. In contrast, the density of PVIs and other GABAergic interneurons was not affected by the loss of *Arx* in PVIs. Similarly, PVI dendritic complexity was indistinguishable from control and *Arx* CKO mice. Overall, our results validate the RNAseq data and provide strong evidence that ECM-related biological pathways are central to network abnormalities in *Arx* CKO mice. Indeed, this conclusion is supported by previous reports of epileptogenesis in mice deficient in ECM molecules (Dityatev, 2010; Vasudevan et al., 2010) and reports of seizures leading to remodeling of the ECM (Dityatev, 2010).

PVIs are connected to pyramidal cells in cortical regions via feedback and feedforward microcircuits (Klausberger and Somogyi, 2008), endowing the intrinsic properties of these interneurons with the power to influence the output of pyramidal cells. Intrinsic membrane active properties were found to be reduced in PVIs of the *Arx* CKO mice. Notably, the rheobase and spike frequency properties were among the most profoundly affected intrinsic properties. Interestingly, these observations were not correlated with changes in the expression voltage-gated ion channels in our RNAseq dataset. We surmise that they are likely linked to the downregulation of ECM genes in PVIs and subsequent breakdown of the PNNs around these cells. Indeed, several studies have demonstrated direct intrinsic membrane impairments in line with our observations following enzymatic breakdown of the PNNs (Balmer, 2016; Lensjo et al., 2017).

How does the dysregulation of ECM and subsequent breakdown of the PNNs lead to hypo-excitability of PVIs in the absence of dysregulated ion channels? One hypothesis to explain this would be altered dendritic complexity. We were not able to demonstrate a dendritic change, despite the previously reported relationship between dendritic complexity and neuronal excitability (Mason and Larkman, 1990). Another possibility, that our data support, is that dysregulated ECM and changes to the PNNs alters the density of voltage-dependent ion channels at the membrane. Indeed, it has been previously shown that the PNN component tenascin-R interacts with NaV1.2 (Srinivasan et al., 1998), suggesting that clusters of NaV1.2 bound by tenascin-R could have diffused after degradation of the PNNs around PVIs, leading to hypo-excitability. In addition, breakdown of the PNN could lead to the loss of negative charge with decrease in extracellular protein (Morawski et al., 2015) ultimately impacting local electric field sensing by ion channels and subsequent neutralization of membrane surface charge akin to the effect of high extracellular [Ca^{2+} on membrane properties (Frankenhaeuser and Hodgkin, 1957). This neutralizing effect by diffused PNN could have then shifted the voltage-dependence of ion channels toward more depolarized membrane potentials (Frankenhaeuser and Hodgkin, 1957), leading to higher rheobase current and reduced spiking as noted in *Arx* null PVIs. Although our RNAseq data support an ECM-dependent mechanism in the alterations of PVI membrane properties, we acknowledge that the excitable properties of neurons, which can be influenced by localization or phosphorylation, may not always align to the transcriptomic level of a particular ion channel. Although RNA-Seq transcriptomic profiling provides a comprehensive analysis of actively regulated genes, many studies have found no correlation or seemingly inverse relationships between the expression of various membrane (Adelman et al., 2019; Bomkamp et al., 2019; Földy et al., 2016; Larson et al., 2016; Tripathy et al., 2017) and synaptic (Fazel Darbandi et al., 2018; Harrington et al., 2016; Yook et al., 2019) genes with their electrophysiological properties. Thus, the relationship between gene expression and cellular/behavioral phenotypes is complex, and this complexity must be taken into account in future studies into the ion channel mechanisms mediating hypoexcitability of PVIs in *Arx* CKO mice.

In addition to impaired intrinsic properties, disruption in the balance of excitation and inhibition likely contributes to network hyper-excitability in *Arx* CKO mice (He and Cline, 2019). Thus, we recorded both spontaneous EPSC and IPSC currents on PVIs and noted a constellation of changes to the properties of these spontaneous events in presence or absence of TTX that suggests an overall reduction in basal excitatory drives onto PVIs. A reduction in sEPSC frequency and mEPSC amplitude was most prominent among those changes. There are many possible explanations for those prominent changes. For example, fewer excitatory synapses, altered probability of vesicle release, or reduced network activity could all be altered via

cell autonomous and non-cell autonomous mechanisms. However, the lack of changes in mini EPSCs frequency and preservation of normal dendritic elaboration suggest that change in synaptic density on PVIs is not a likely contributing factor.

To further probe the contribution of impaired synaptic drive to network hyper-excitability in *Arx* CKO mice, we measured I-O relationship of evoked EPSCs and IPSCs on PVIs and found a decreased excitability of PVIs primarily driven by a reduction in eEPSCs. The locus of this reduction in synaptic excitability appeared to be the postsynaptic side as evidenced by changes in conduction and ratio of AMPA and NMDA receptors. The reduction in postsynaptic GluR current at PVI synapses is inconsistent with the upregulation of DEGs associated with excitatory transmission. We surmise that this may be part of an ongoing compensatory response to restore synaptic excitability at PVI synapses following the loss of *Arx*. The reduction in excitatory transmission in the face of increased expression of glutamate receptor signaling genes can be explained by reduction in lateral diffusion of AMPA and NMDA receptors from extracellular to synaptic compartments (Groc et al., 2006). Previous studies have shown that the ECM/PNN components do indeed operate as passive diffusion barrier that control the lateral diffusion exchanges of glutamate receptors between synaptic and extrasynaptic compartments (Shi and Ethell, 2006). Interpretation of the RI of the AMPA and NMDA receptors herein may be complicated by their reversal potentials, which were considerably different from 0 mV, an observation previously noted in another study (Suyama et al., 2017). This error in voltage could be due to series resistance, activation of K+ channels at positive potential, liquid junction potential, and poor space clamp among others. We limited the source of this error by employing a cesium-based internal solution to block K^+ leak currents and compensated for liquid junction potential as well as series resistance, albeit up to 80%. We suppose that this error in voltage might then be due to poor space clamp, a serious limitation in slice recordings that is currently difficult to overcome. To mitigate its impact on our analysis, we excluded cells whose reversal potentials were substantially far from 0 mV and made sure the reversal potentials in the remaining cells from both genotypes were comparable. Nonetheless, these findings strengthen our conclusion that the reduction in PVI synaptic excitability was primarily associated with impaired excitatory drives with a postsynaptic locus.

Taken together, our findings demonstrate that continued expression of *Arx* has an important role in the functional maintenance of PVIs and that alterations in *Arx* expression in these cells specifically during early postnatal brain development contributes to the pathologic mechanisms of *ARX*-related EOEEs. Although the precise molecular mechanisms mediating this postnatal role remain to be elucidated, our results establish a role for *Arx* transcriptional activity in the functional properties of PVIs and in the proper maintenance of ECM integrity around these cells. Loss of this postnatal transcriptomic regulation of PVIs resulted in a profound reduction in intrinsic and synaptic excitability, leading to behavioral and network abnormalities. Our results suggest that restoration of cellular properties and network functioning in adult mice may be a viable therapeutic approach toward ARX-related EOEEs. Notably, functional restoration of circuit activity in mature mice by Cre-mediated re-expression of certain genes (Cisse et al., 2017; Guy et al., 2007; Rotaru et al., 2018; Silva-Santos et al., 2015; Ure et al., 2016) or by cell transplantation (Casalia et al., 2017; Cunningham et al., 2014; Howard et al., 2014) has shown great promise in a number of NDDs including Rett syndrome, Dravet syndrome, and Angelman syndrome. Similar approaches could be applied to the *Arx*-linked EEOE mouse models in the near future to test whether reintroduction of *Arx* or downstream effectors, including epigenetic and epitranscriptomic regulators, could provide more precise and enduring restorative therapeutics in *Arx*-linked EOEEs.

Limitations of the study

We aimed to determine the role of an early acting developmental TF *Arx* in neural circuits and its contribution to the progression of EOEEs by using cre-lox technology. Although our new PVI CKO model allowed dissection of the functional consequence of *Arx* ablation in PVIs, this model does not mimic the normal disease process, which involves both developmental and ongoing dysfunction in *Arx* signaling in all interneurons. Another limitation is that although we focused our investigations on the hippocampus, a region vital for learning and seizure generation, *Arx* expression was also ablated in PVIs from other brain regions in our *Arx* CKO model. Therefore, we cannot rule out the possibility of *Arx*-fulfilling distinct functions at other brain regions nor the possibility of the noted effects in CA1 hippocampus being mediated by connective or interactive defects between those regions. Despite these limitations, cell-type-restricted gene knockout models represent necessary models to understand the biological underpinnings of neurological disorders including the EOEEs. This is particularly relevant to *Arx*-linked EOEEs, given the pleiotropic phenotypes,

strong genotype-phenotype relationship, and the numerous symptoms associated with *ARX* disorders are probably related to cell-specific alterations in the function of *Arx*. This study has now defined important roles for postnatal *Arx* in PVIs in the specific control of neural circuit function in the hippocampus. Further studies are needed, however, to establish the specific roles of this TF in PVIs from other brain regions as well as in other interneuron subtypes throughout the brain. Insights from those studies along with those from this study should provide a more comprehensive view of the full range of control exerted by postnatal *Arx* transcriptional activity in the complex regulation of neural circuits and facilitate the development of targeted circuit-based therapies in EOEEs.

Resource availability

Lead contact

Further information and requests for resources and reagents should be directed to Eric D. Marsh (marshe@email.chop.edu).

Materials availability

No new unique materials or reagents were generated in this study.

Data and code availability

RNA sequencing data are available in GEO depository: GSE157689

https://www.ncbi.nlm.nih.gov/geo/query/acc.cgi?acc=GSE157689.

Datasets used for generating figures are available in Mendeley Data depository: DOI: 10.17632

https://doi.org/10.17632/r94jkwmd5z.1.

MATLAB codes are available from the Lead contact on reasonable request.

METHODS

All methods can be found in the accompanying Transparent Methods supplemental file.

SUPPLEMENTAL INFORMATION

Supplemental information can be found online at https://doi.org/10.1016/j.isci.2020.101999.

ACKNOWLEDGMENTS

This work was supported by the National Institute of Neurological Disorders and Stroke grant (Grant #: RO1 NS082761 to EDM, 2018); The Stiftung zur Förderung der Medizinischen Forschung der Christian-Albrechts-Universität zu Kiel (Fellowship grant to MVD, 2017); the National Institute of Child Health and Human Development (Grant #: 5U54HD086984 to the Institutional Intellectual Developmental Disabilities Research Center Cellular Neuroscience Core at the Children's Hospital of Philadelphia, 2019; and the Epilepsy Foundation (Postdoctoral fellowship #: 367394 to DJJ, 2015). The authors thank Drs Jeffrey A. Golden and Ethan M. Goldberg for providing the *Arx* $^{LoxP/LoxP}$ and PV^{cre} mouse lines, respectively. We thank Rick Matthews, Wendi Burnette, Douglas Coulter, and Hajime Takano for technical support and Jeff Golden for reading the manuscript. We are also grateful for advice and suggestions from members of the Marsh laboratory during the conduct of this research.

AUTHORS CONTRIBUTION

Conceptualization, E.D.M and D.J.J.; Methodology, E.D.M, D.J.J, Y.K, R.C.A-N, A.G.C, and M.V.D.; Investigation, D.J.J, Y.K, M.V.D, A.J.M, and R.R; Writing – Original Draft, D.J.J and E.D.M; Writing – Review & Editing, R.C.A-N, A.G.C, A.J.M, and M.V.D; Visualization, D.J.J, R.C.A-N, A.G.C, and A.J.M; Supervision, E.D.M; Funding Acquisition, E.D.M, M.V.D, and D.J.J.

DECLARATION OF INTERESTS

The authors declare no competing financial interests.

Received: July 17, 2020
Revised: December 8, 2020
Accepted: December 23, 2020
Published: January 22, 2021

REFERENCES

Adelman, P.C., Baumbauer, K.M., Friedman, R., Shah, M., Wright, M., Young, E., Jankowski, M.P., Albers, K.M., and Koerber, H.R. (2019). Single-cell q-PCR derived expression profiles of identified sensory neurons. Mol. Pain *15*, 1744806919884496.

Amilhon, B., Huh, C.Y., Manseau, F., Ducharme, G., Nichol, H., Adamantidis, A., and Williams, S. (2015). Parvalbumin interneurons of Hippocampus tune population activity at theta frequency. Neuron *86*, 1277–1289.

Balmer, T.S. (2016). Perineuronal nets enhance the excitability of fast-spiking neurons. eNeuro *3*, ENEURO.0112-16.2016.

Beguin, S., Crepel, V., Aniksztejn, L., Becq, H., Pelosi, B., Pallesi-Pocachard, E., Bouamrane, L., Pasqualetti, M., Kitamura, K., Cardoso, C., and Represa, A. (2013). An epilepsy-related ARX polyalanine expansion modifies glutamatergic neurons excitability and morphology without affecting GABAergic neurons development. Cereb. Cortex *23*, 1484–1494.

Benayoun, M., Cowan, J.D., van Drongelen, W., and Wallace, E. (2010). Avalanches in a stochastic model of spiking neurons. PLoS Comput. Biol. *6*, e1000846.

Billingslea, E.N., Tatard-Leitman, V.M., Anguiano, J., Jutzeler, C.R., Suh, J., Saunders, J.A., Morita, S., Featherstone, R.E., Ortinski, P.I., Gandal, M.J., et al. (2014). Parvalbumin cell ablation of NMDA-R1 causes increased resting network excitability with associated social and self-care deficits. Neuropsychopharmacology *39*, 1603–1613.

Bolivar, V.J., Caldarone, B.J., Reilly, A.A., and Flaherty, L. (2000). Habituation of activity in an open field: a survey of inbred strains and F1 hybrids. Behav. Genet. *30*, 285–293.

Bomkamp, C., Tripathy, S.J., Bengtsson Gonzales, C., Hjerling-Leffler, J., Craig, A.M., and Pavlidis, P. (2019). Transcriptomic correlates of electrophysiological and morphological diversity within and across excitatory and inhibitory neuron classes. PLoS Comput. Biol. *15*, e1007113.

Bothe, G.W., Bolivar, V.J., Vedder, M.J., and Geistfeld, J.G. (2005). Behavioral differences among fourteen inbred mouse strains commonly used as disease models. Comp. Med. *55*, 326–334.

Buenrostro, J.D., Giresi, P.G., Zaba, L.C., Chang, H.Y., and Greenleaf, W.J. (2013). Transposition of native chromatin for fast and sensitive epigenomic profiling of open chromatin, DNA-binding proteins and nucleosome position. Nat. Methods *10*, 1213–1218.

Carlen, M., Meletis, K., Siegle, J.H., Cardin, J.A., Futai, K., Vierling-Claassen, D., Ruhlmann, C., Jones, S.R., Deisseroth, K., Sheng, M., et al. (2012). A critical role for NMDA receptors in parvalbumin interneurons for gamma rhythm induction and behavior. Mol. Psychiatry *17*, 537–548.

Casalia, M.L., Howard, M.A., and Baraban, S.C. (2017). Persistent seizure control in epileptic mice transplanted with gamma-aminobutyric acid progenitors. Ann. Neurol. *82*, 530–542.

Cisse, M., Duplan, E., Lorivel, T., Dunys, J., Bauer, C., Meckler, X., Gerakis, Y., Lauritzen, I., and Checler, F. (2017). The transcription factor XBP1s restores hippocampal synaptic plasticity and memory by control of the Kalirin-7 pathway in Alzheimer model. Mol. Psychiatry *22*, 1562–1575.

Colgin, L.L. (2013). Mechanisms and functions of theta rhythms. Annu. Rev. Neurosci. *36*, 295–312.

Colombo, E., Collombat, P., Colasante, G., Bianchi, M., Long, J., Mansouri, A., Rubenstein, J.L., and Broccoli, V. (2007). Inactivation of Arx, the murine ortholog of the X-linked lissencephaly with ambiguous genitalia gene, leads to severe disorganization of the ventral telencephalon with impaired neuronal migration and differentiation. J. Neurosci. *27*, 4786–4798.

Cunningham, M., Cho, J.H., Leung, A., Savvidis, G., Ahn, S., Moon, M., Lee, P.K., Han, J.J., Azimi, N., Kim, K.S., et al. (2014). hPSC-derived maturing GABAergic interneurons ameliorate seizures and abnormal behavior in epileptic mice. Cell Stem Cell *15*, 559–573.

Dawson, G.R., and Tricklebank, M.D. (1995). Use of the elevated plus maze in the search for novel anxiolytic agents. Trends Pharmacol. Sci. *16*, 33–36.

Dityatev, A. (2010). Remodeling of extracellular matrix and epileptogenesis. Epilepsia *51* (*Suppl 3*), 61–65.

Dityatev, A., Bruckner, G., Dityateva, G., Grosche, J., Kleene, R., and Schachner, M. (2007). Activity-dependent formation and functions of chondroitin sulfate-rich extracellular matrix of perineuronal nets. Dev. Neurobiol. *67*, 570–588.

Dohm, J.C., Lottaz, C., Borodina, T., and Himmelbauer, H. (2008). Substantial biases in ultra-short read data sets from high-throughput DNA sequencing. Nucleic Acids Res. *36*, e105.

Doischer, D., Hosp, J.A., Yanagawa, Y., Obata, K., Jonas, P., Vida, I., and Bartos, M. (2008). Postnatal differentiation of basket cells from slow to fast signaling devices. J. Neurosci. *28*, 12956–12968.

Dubos, A., Meziane, H., Iacono, G., Curie, A., Riet, F., Martin, C., Loaec, N., Birling, M.C., Selloum, M., Normand, E., et al. (2018). A new mouse model of ARX dup24 recapitulates the patients' behavioral and fine motor alterations. Hum. Mol. Genet. *27*, 2138–2153.

Ennaceur, A., and Delacour, J. (1988). A new one-trial test for neurobiological studies of memory in rats. 1: behavioral data. Behav. Brain Res. *31*, 47–59.

Favuzzi, E., Marques-Smith, A., Deogracias, R., Winterflood, C.M., Sanchez-Aguilera, A., Mantoan, L., Maeso, P., Fernandes, C., Ewers, H., and Rico, B. (2017). Activity-dependent gating of parvalbumin interneuron function by the perineuronal net protein brevican. Neuron *95*, 639–655 e610.

Fazel Darbandi, S., Robinson Schwartz, S.E., Qi, Q., Catta-Preta, R., Pai, E.L., Mandell, J.D., Everitt, A., Rubin, A., Krasnoff, R.A., Katzman, S., et al. (2018). Neonatal Tbr1 dosage controls cortical layer 6 connectivity. Neuron *100*, 831–845.e837.

Fishell, G., and Kepecs, A. (2019). Interneuron types as attractors and controllers. Annu. Rev. Neurosci. *43*, 1–30.

Földy, C., Darmanis, S., Aoto, J., Malenka, R.C., Quake, S.R., and Südhof, T.C. (2016). Single-cell RNAseq reveals cell adhesion molecule profiles in electrophysiologically defined neurons. Proc. Natl. Acad. Sci. U S A *113*, E5222–E5231.

Frankenhaeuser, B., and Hodgkin, A.L. (1957). The action of calcium on the electrical properties of squid axons. J. Physiol. *137*, 218–244.

Fuchs, E.C., Zivkovic, A.R., Cunningham, M.O., Middleton, S., Lebeau, F.E., Bannerman, D.M., Rozov, A., Whittington, M.A., Traub, R.D., Rawlins, J.N., and Monyer, H. (2007). Recruitment of parvalbumin-positive interneurons determines hippocampal function and associated behavior. Neuron *53*, 591–604.

Fulp, C.T., Cho, G., Marsh, E.D., Nasrallah, I.M., Labosky, P.A., and Golden, J.A. (2008). Identification of Arx transcriptional targets in the developing basal forebrain. Hum. Mol. Genet. *17*, 3740–3760.

Giamanco, K.A., and Matthews, R.T. (2012). Deconstructing the perineuronal net: cellular contributions and molecular composition of the neuronal extracellular matrix. Neuroscience *218*, 367–384.

Gonzalez-Burgos, G., and Lewis, D.A. (2008). GABA neurons and the mechanisms of network oscillations: implications for understanding cortical dysfunction in schizophrenia. Schizophr Bull. *34*, 944–961.

Goodman, J., and McIntyre, C.K. (2017). Impaired spatial memory and enhanced habit memory in a rat model of post-traumatic stress disorder. Front. Pharmacol. *8*, 663.

Gordon, J.A., Lacefield, C.O., Kentros, C.G., and Hen, R. (2005). State-dependent alterations in hippocampal oscillations in serotonin 1A receptor-deficient mice. J. Neurosci. *25*, 6509–6519.

Groc, L., Heine, M., Cousins, S.L., Stephenson, F.A., Lounis, B., Cognet, L., and Choquet, D. (2006). NMDA receptor surface mobility depends on NR2A-2B subunits. Proc. Natl. Acad. Sci. U S A *103*, 18769–18774.

Guy, J., Gan, J., Selfridge, J., Cobb, S., and Bird, A. (2007). Reversal of neurological defects in a mouse model of Rett syndrome. Science *315*, 1143–1147.

Harrington, A.J., Raissi, A., Rajkovich, K., Berto, S., Kumar, J., Molinaro, G., Raduazzo, J., Guo, Y., Loerwald, K., Konopka, G., et al. (2016). MEF2C regulates cortical inhibitory and excitatory synapses and behaviors relevant to neurodevelopmental disorders. Elife *5*, e20059.

He, H.Y., and Cline, H.T. (2019). What is excitation/inhibition and how is it regulated? A case of the elephant and the wisemen. J. Exp. Neurosci. *13*, 1179069519859371.

Hippenmeyer, S., Vrieseling, E., Sigrist, M., Portmann, T., Laengle, C., Ladle, D.R., and Arber, S. (2005). A developmental switch in the response of DRG neurons to ETS transcription factor signaling. PLoS Biol. *3*, e159.

Howard, M.A., Rubenstein, J.L., and Baraban, S.C. (2014). Bidirectional homeostatic plasticity induced by interneuron cell death and transplantation in vivo. Proc. Natl. Acad. Sci. U S A *111*, 492–497.

Hu, H., Gan, J., and Jonas, P. (2014). Interneurons. Fast-spiking, parvalbumin(+) GABAergic interneurons: from cellular design to microcircuit function. Science *345*, 1255263.

Huang da, W., Sherman, B.T., and Lempicki, R.A. (2009). Systematic and integrative analysis of large gene lists using DAVID bioinformatics resources. Nat. Protoc. *4*, 44–57.

Jackson, M.R., Lee, K., Mattiske, T., Jaehne, E.J., Ozturk, E., Baune, B.T., O'Brien, T.J., Jones, N., and Shoubridge, C. (2017). Extensive phenotyping of two ARX polyalanine expansion mutation mouse models that span clinical spectrum of intellectual disability and epilepsy. Neurobiol. Dis. *105*, 245–256.

Karolchik, D., Hinrichs, A.S., Furey, T.S., Roskin, K.M., Sugnet, C.W., Haussler, D., and Kent, W.J. (2004). The UCSC Table Browser data retrieval tool. Nucleic Acids Res. *32*, D493–D496.

Kato, M., and Dobyns, W.B. (2005). X-linked lissencephaly with abnormal genitalia as a tangential migration disorder causing intractable epilepsy: proposal for a new term, "interneuronopathy. J. Child Neurol. *20*, 392–397.

Kitamura, K., Itou, Y., Yanazawa, M., Ohsawa, M., Suzuki-Migishima, R., Umeki, Y., Hohjoh, H., Yanagawa, Y., Shinba, T., Itoh, M., et al. (2009). Three human ARX mutations cause the lissencephaly-like and mental retardation with epilepsy-like pleiotropic phenotypes in mice. Hum. Mol. Genet. *18*, 3708–3724.

Kitamura, K., Yanazawa, M., Sugiyama, N., Miura, H., Iizuka-Kogo, A., Kusaka, M., Omichi, K., Suzuki, R., Kato-Fukui, Y., Kamiirisa, K., et al. (2002). Mutation of ARX causes abnormal development of forebrain and testes in mice and X-linked lissencephaly with abnormal genitalia in humans. Nat. Genet. *32*, 359–369.

Klausberger, T., and Somogyi, P. (2008). Neuronal diversity and temporal dynamics: the unity of hippocampal circuit operations. Science *321*, 53–57.

Korotkova, T., Fuchs, E.C., Ponomarenko, A., von Engelhardt, J., and Monyer, H. (2010). NMDA receptor ablation on parvalbumin-positive interneurons impairs hippocampal synchrony, spatial representations, and working memory. Neuron *68*, 557–569.

Kuhlman, S.J., and Huang, Z.J. (2008). High-resolution labeling and functional manipulation of specific neuron types in mouse brain by Cre-activated viral gene expression. PloS one *3*, e2005.

Larson, V.A., Zhang, Y., and Bergles, D.E. (2016). Electrophysiological properties of NG2(+) cells: matching physiological studies with gene expression profiles. Brain Res. *1638*, 138–160.

Le Magueresse, C., and Monyer, H. (2013). GABAergic interneurons shape the functional maturation of the cortex. Neuron *77*, 388–405.

Lee, K., Ireland, K., Bleeze, M., and Shoubridge, C. (2017). ARX polyalanine expansion mutations lead to migration impediment in the rostral cortex coupled with a developmental deficit of calbindin-positive cortical GABAergic interneurons. Neuroscience *357*, 220–231.

Lenhard, B., Sandelin, A., and Carninci, P. (2012). Metazoan promoters: emerging characteristics and insights into transcriptional regulation. Nat. Rev. Genet. *13*, 233–245.

Lensjo, K.K., Lepperod, M.E., Dick, G., Hafting, T., and Fyhn, M. (2017). Removal of perineuronal nets unlocks juvenile plasticity through network mechanisms of decreased inhibition and increased gamma activity. J. Neurosci. *37*, 1269–1283.

Liu, T., Ortiz, J.A., Taing, L., Meyer, C.A., Lee, B., Zhang, Y., Shin, H., Wong, S.S., Ma, J., Lei, Y., et al. (2011). Cistrome: an integrative platform for transcriptional regulation studies. Genome Biol. *12*, R83.

Love, M.I., Huber, W., and Anders, S. (2014). Moderated estimation of fold change and dispersion for RNA-seq data with DESeq2. Genome Biol. *15*, 550.

Lozoya, O.A., Santos, J.H., and Woychik, R.P. (2018). A leveraged signal-to-noise ratio (LSTNR) method to extract differentially expressed genes and multivariate patterns of expression from noisy and low-replication RNAseq data. Front. Genet. *9*, 176.

Madisen, L., Zwingman, T.A., Sunkin, S.M., Oh, S.W., Zariwala, H.A., Gu, H., Ng, L.L., Palmiter, R.D., Hawrylycz, M.J., Jones, A.R., et al. (2010). A robust and high-throughput Cre reporting and characterization system for the whole mouse brain. Nat. Neurosci. *13*, 133–140.

Marsh, E., Fulp, C., Gomez, E., Nasrallah, I., Minarcik, J., Sudi, J., Christian, S.L., Mancini, G., Labosky, P., Dobyns, W., et al. (2009). Targeted loss of Arx results in a developmental epilepsy mouse model and recapitulates the human phenotype in heterozygous females. Brain *132*, 1563–1576.

Mason, A., and Larkman, A. (1990). Correlations between morphology and electrophysiology of pyramidal neurons in slices of rat visual cortex. II. Electrophysiology. J. Neurosci. *10*, 1415–1428.

McLean, C.Y., Bristor, D., Hiller, M., Clarke, S.L., Schaar, B.T., Lowe, C.B., Wenger, A.M., and Bejerano, G. (2010). GREAT improves functional interpretation of cis-regulatory regions. Nat. Biotechnol. *28*, 495–501.

Migliore, M., and Shepherd, G.M. (2005). Opinion: an integrated approach to classifying neuronal phenotypes. Nat. Rev. Neurosci. *6*, 810–818.

Miller, B.H., Schultz, L.E., Gulati, A., Su, A.I., and Pletcher, M.T. (2010). Phenotypic characterization of a genetically diverse panel of mice for behavioral despair and anxiety. PloS one *5*, e14458.

Mo, A., Mukamel, E.A., Davis, F.P., Luo, C., Henry, G.L., Picard, S., Urich, M.A., Nery, J.R., Sejnowski, T.J., Lister, R., et al. (2015). Epigenomic signatures of neuronal diversity in the mammalian brain. Neuron *86*, 1369–1384.

Montojo, J., Zuberi, K., Rodriguez, H., Bader, G.D., and Morris, Q. (2014). GeneMANIA: fast gene network construction and function prediction for Cytoscape. F1000Res *3*, 153.

Morawski, M., Reinert, T., Meyer-Klaucke, W., Wagner, F.E., Troger, W., Reinert, A., Jager, C., Bruckner, G., and Arendt, T. (2015). Ion exchanger in the brain: quantitative analysis of perineuronally fixed anionic binding sites suggests diffusion barriers with ion sorting properties. Sci. Rep. *5*, 16471.

Morishita, H., Cabungcal, J.H., Chen, Y., Do, K.Q., and Hensch, T.K. (2015). Prolonged period of cortical plasticity upon redox dysregulation in fast-spiking interneurons. Biol. Psychiatry *78*, 396–402.

Moy, S.S., Nadler, J.J., Young, N.B., Perez, A., Holloway, L.P., Barbaro, R.P., Barbaro, J.R., Wilson, L.M., Threadgill, D.W., Lauder, J.M., et al. (2007). Mouse behavioral tasks relevant to autism: phenotypes of 10 inbred strains. Behav. Brain Res. *176*, 4–20.

Nguyen, N.T.T., Contreras-Moreira, B., Castro-Mondragon, J.A., Santana-Garcia, W., Ossio, R., Robles-Espinoza, C.D., Bahin, M., Collombet, S., Vincens, P., Thieffry, D., et al. (2018). RSAT 2018: regulatory sequence analysis tools 20th anniversary. Nucleic Acids Res. *46*, W209–W214.

Nordli, D.R., Jr. (2012). Epileptic encephalopathies in infants and children. J. Clin. Neurophysiol. *29*, 420–424.

Ogiwara, I., Iwasato, T., Miyamoto, H., Iwata, R., Yamagata, T., Mazaki, E., Yanagawa, Y., Tamamaki, N., Hensch, T.K., Itohara, S., and Yamakawa, K. (2013). Nav1.1 haploinsufficiency in excitatory neurons ameliorates seizure-associated sudden death in a mouse model of Dravet syndrome. Hum. Mol. Genet. *22*, 4784–4804.

Packard, M.G., and Wingard, J.C. (2004). Amygdala and "emotional" modulation of the relative use of multiple memory systems. Neurobiol. Learn. Mem. *82*, 243–252.

Phillips, R.G., and LeDoux, J.E. (1992). Differential contribution of amygdala and hippocampus to cued and contextual fear conditioning. Behav. Neurosci. *106*, 274–285.

Pisciotta, L., Capra, V., Accogli, A., Giacomini, T., Prato, G., Tavares, P., Pinto-Basto, J., Morana, G., and Mancardi, M.M. (2018). Epileptic encephalopathy in adams-oliver syndrome associated to a new DOCK6 mutation: a peculiar behavioral phenotype. Neuropediatrics *49*, 217–221.

Price, M.G., Yoo, J.W., Burgess, D.L., Deng, F., Hrachovy, R.A., Frost, J.D., Jr., and Noebels, J.L. (2009). A triplet repeat expansion genetic mouse model of infantile spasms syndrome, Arx(GCG) 10+7, with interneuronopathy, spasms in infancy, persistent seizures, and adult cognitive and behavioral impairment. J. Neurosci. *29*, 8752–8763.

Radmanesh, F., Caglayan, A.O., Silhavy, J.L., Yilmaz, C., Cantagrel, V., Omar, T., Rosti, B., Kaymakcalan, H., Gabriel, S., Li, M., et al. (2013). Mutations in LAMB1 cause cobblestone brain malformation without muscular or ocular abnormalities. Am. J. Hum. Genet. *92*, 468–474.

Rotaru, D.C., van Woerden, G.M., Wallaard, I., and Elgersma, Y. (2018). Adult Ube3a gene reinstatement restores the electrophysiological deficits of prefrontal cortex layer 5 neurons in a mouse model of angelman syndrome. J. Neurosci. *38*, 8011–8030.

Rudy, B., and McBain, C.J. (2001). Kv3 channels: voltage-gated K+ channels designed for high-frequency repetitive firing. Trends Neurosci. *24*, 517–526.

Saunders, J.A., Tatard-Leitman, V.M., Suh, J., Billingslea, E.N., Roberts, T.P., and Siegel, S.J. (2013). Knockout of NMDA receptors in parvalbumin interneurons recreates autism-like phenotypes. Autism Res. *6*, 69–77.

Shi, Y., and Ethell, I.M. (2006). Integrins control dendritic spine plasticity in hippocampal neurons through NMDA receptor and Ca2+/calmodulin-dependent protein kinase II-mediated actin reorganization. J. Neurosci. *26*, 1813–1822.

Sholl, D.A. (1953). Dendritic organization in the neurons of the visual and motor cortices of the cat. J. Anat. *87*, 387–406.

Shoubridge, C., Fullston, T., and Gecz, J. (2010). ARX spectrum disorders: making inroads into the molecular pathology. Hum. Mutat. *31*, 889–900.

Sik, A., van Nieuwehuyzen, P., Prickaerts, J., and Blokland, A. (2003). Performance of different mouse strains in an object recognition task. Behav. Brain Res. *147*, 49–54.

Silva-Santos, S., van Woerden, G.M., Bruinsma, C.F., Mientjes, E., Jolfaei, M.A., Distel, B., Kushner, S.A., and Elgersma, Y. (2015). Ube3a reinstatement identifies distinct developmental windows in a murine Angelman syndrome model. J. Clin. Invest. *125*, 2069–2076.

Simonet, J.C., Sunnen, C.N., Wu, J., Golden, J.A., and Marsh, E.D. (2015). Conditional loss of Arx from the developing dorsal telencephalon results in behavioral phenotypes resembling mild human ARX mutations. Cereb. Cortex *25*, 2939–2950.

Srinivasan, J., Schachner, M., and Catterall, W.A. (1998). Interaction of voltage-gated sodium channels with the extracellular matrix molecules tenascin-C and tenascin-R. Proc. Natl. Acad. Sci. U S A *95*, 15753–15757.

Stranahan, A.M., Erion, J.R., and Wosiski-Kuhn, M. (2013). Reelin signaling in development, maintenance, and plasticity of neural networks. Ageing Res. Rev. *12*, 815–822.

Suyama, S., Ralevski, A., Liu, Z.W., Dietrich, M.O., Yada, T., Simonds, S.E., Cowley, M.A., Gao, X.B., Diano, S., and Horvath, T.L. (2017). Plasticity of calcium-permeable AMPA glutamate receptors in Pro-opiomelanocortin neurons. Elife *6*, e25755.

Suzuki, O.T., Sertie, A.L., Der Kaloustian, V.M., Kok, F., Carpenter, M., Murray, J., Czeizel, A.E., Kliemann, S.E., Rosemberg, S., Monteiro, M., et al. (2002). Molecular analysis of collagen XVIII reveals novel mutations, presence of a third isoform, and possible genetic heterogeneity in Knobloch syndrome. Am. J. Hum. Genet. *71*, 1320–1329.

Tripathy, S.J., Toker, L., Li, B., Crichlow, C.L., Tebaykin, D., Mancarci, B.O., and Pavlidis, P. (2017). Transcriptomic correlates of neuron electrophysiological diversity. PLoS Comput. Biol. *13*, e1005814.

Ure, K., Lu, H., Wang, W., Ito-Ishida, A., Wu, Z., He, L.J., Sztainberg, Y., Chen, W., Tang, J., and Zoghbi, H.Y. (2016). Restoration of Mecp2 expression in GABAergic neurons is sufficient to rescue multiple disease features in a mouse model of Rett syndrome. Elife *5*, e14198.

van der Velden, L., van Hooft, J.A., and Chameau, P. (2012). Altered dendritic complexity affects firing properties of cortical layer 2/3 pyramidal neurons in mice lacking the 5-HT3A receptor. J. Neurophysiol. *108*, 1521–1528.

Van Meer, P., and Raber, J. (2005). Mouse behavioural analysis in systems biology. Biochem. J. *389*, 593–610.

Vasudevan, A., Ho, M.S., Weiergraber, M., Nischt, R., Schneider, T., Lie, A., Smyth, N., and Kohling, R. (2010). Basement membrane protein nidogen-1 shapes hippocampal synaptic plasticity and excitability. Hippocampus *20*, 608–620.

Verma, V., Paul, A., Amrapali Vishwanath, A., Vaidya, B., and Clement, J.P. (2019). Understanding intellectual disability and autism spectrum disorders from common mouse models: synapses to behaviour. Open Biol. *9*, 180265.

Wuarin, J.P., and Dudek, F.E. (1993). Patch-clamp analysis of spontaneous synaptic currents in supraoptic neuroendocrine cells of the rat hypothalamus. J. Neurosci. *13*, 2323–2331.

Yook, C., Kim, K., Kim, D., Kang, H., Kim, S.G., Kim, E., and Kim, S.Y. (2019). A TBR1-K228E mutation induces Tbr1 upregulation, altered cortical distribution of interneurons, increased inhibitory synaptic transmission, and autistic-like behavioral deficits in mice. Front. Mol. Neurosci. *12*, 241.

Zhou, F.W., Chen, H.X., and Roper, S.N. (2009). Balance of inhibitory and excitatory synaptic activity is altered in fast-spiking interneurons in experimental cortical dysplasia. J. Neurophysiol. *102*, 2514–2525.

iScience, Volume *24*

Supplemental Information

Postnatal *Arx* transcriptional activity regulates functional properties of PV interneurons

Donald J. Joseph, Markus Von Deimling, Yuiko Hasegawa, Ana G. Cristancho, Rebecca C. Ahrens-Nicklas, Stephanie L. Rogers, Rashmi Risbud, Almedia J. McCoy, and Eric D. Marsh

Supplemental figures and legends

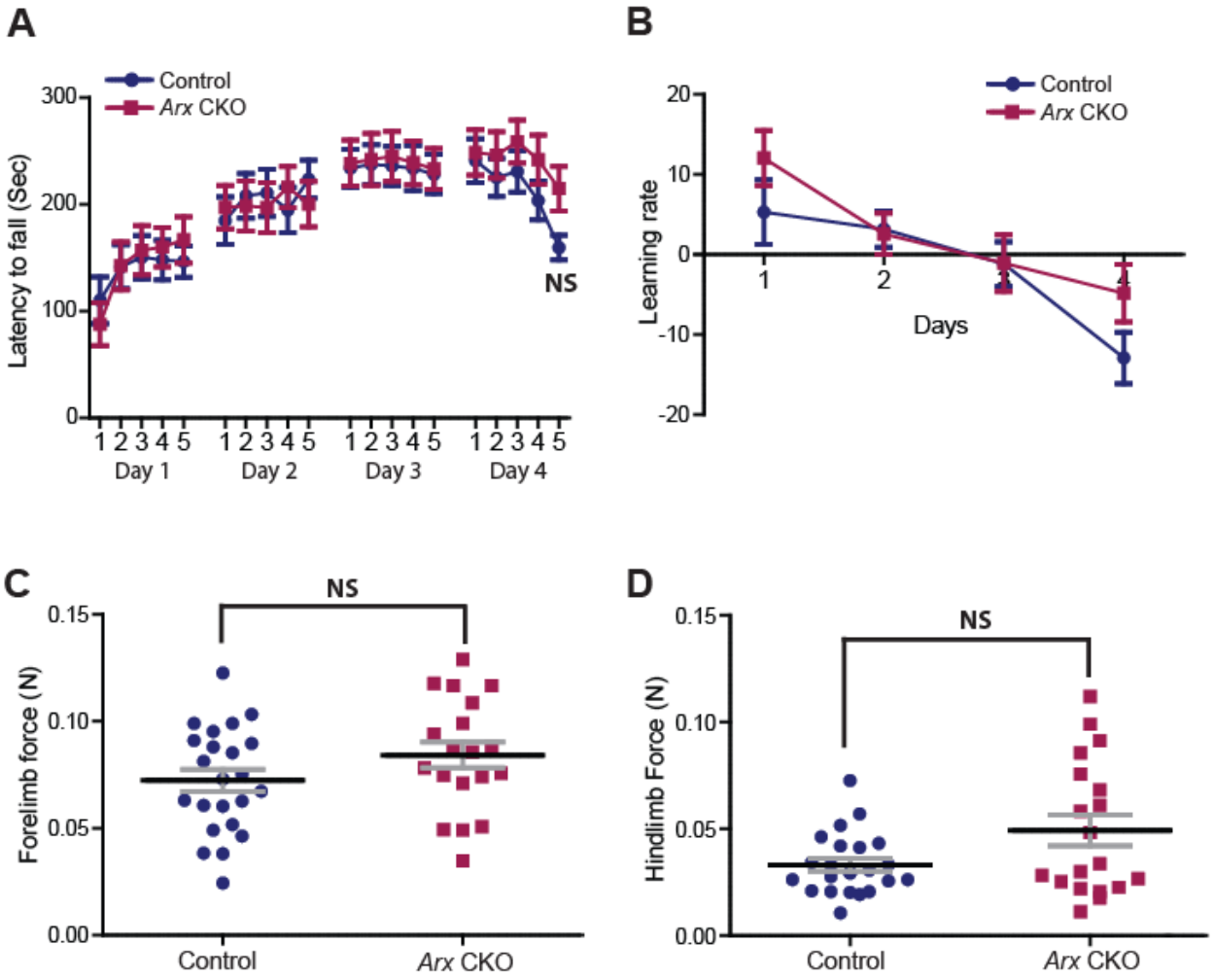

Supplemental Figure 1. Basal motor functions are normal in *Arx* CKO mice. (**A, B**) Normal motor coordination (**A**) and learning rate (B) by *Arx* CKO mice in the accelerated rotarod (*P>0.05*; Control, *Arx* CKO: n=23, 19). (**C & D**) Control and *Arx* CKO mice displayed similar level of muscle strength in the forelimb (**C**) and hindlimb (**D**) grip strength tests (*P>0.05*; Control, *Arx* CKO: n=23, 19). Data in all the graphs are given as mean±SEM and analyzed by Two-way ANOVA (**A & B**) or Mann Whitney U test (**C & D**). Related to figure 3.

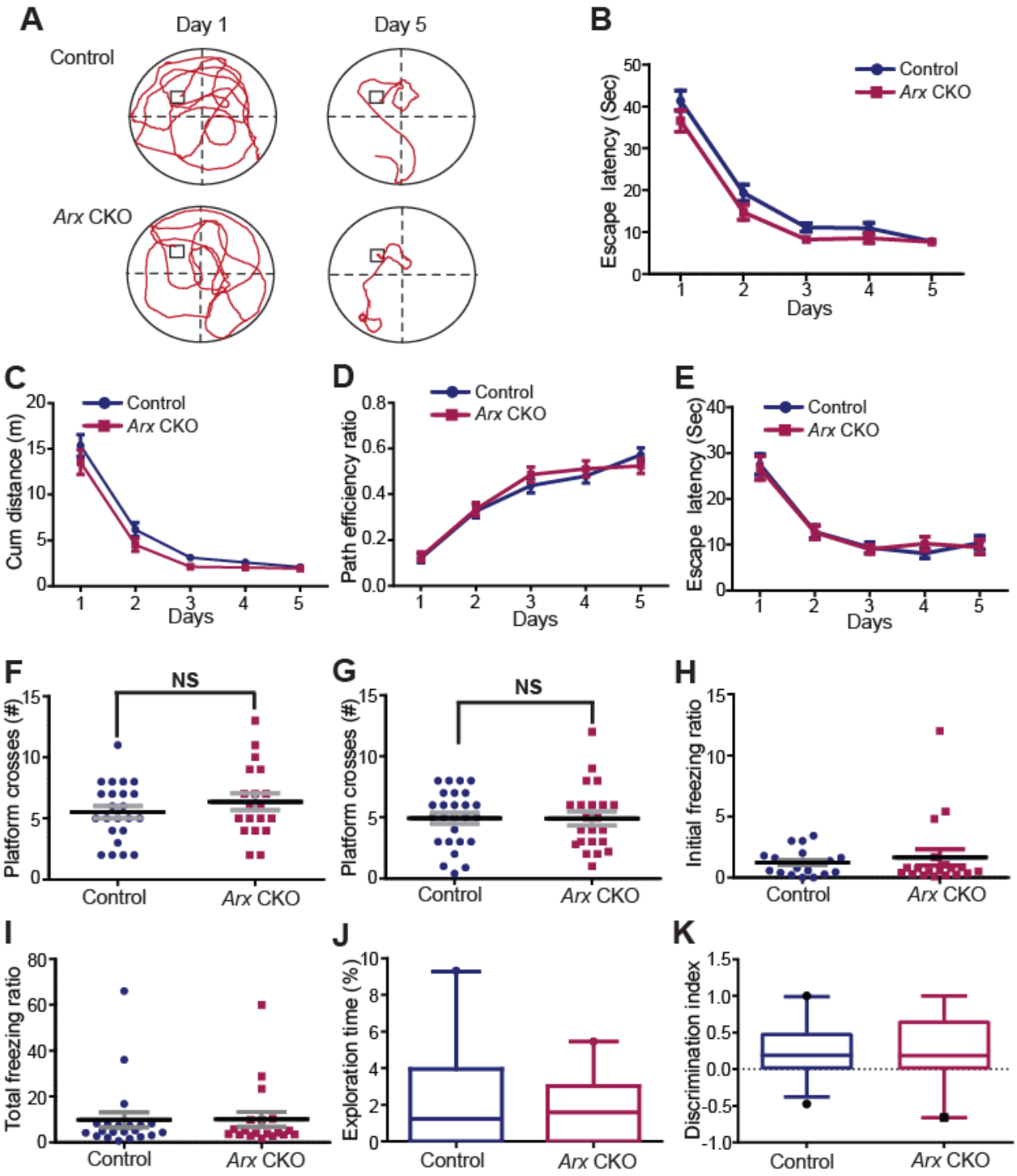
A
Day 1
Day 5
Control
Arx CKO
B
Escape latency (Sec)
Days
Control
Arx CKO
C
Cum distance (m)
Days
D
Path efficiency ratio
E
F
NS
Platform crosses (#)
G
H
Initial freezing ratio
I
Total freezing ratio
J
Exploration time (%)
K
Discrimination index

Supplemental Figure 2. Cognitive ability is preserved in *Arx* CKO mice. (**A**) Graphical representation of search patterns during learning in the MWM test. The hidden platform is displayed as a square in each graph. (**B, C**) Control and *Arx* CKO mice performed equally well during the forward (**B-D**) and reversal (**E**) learning phases of the MWM test (*P>0.05*; Control, *Arx* CKO: n=23, 19). (**F & G**) Memory recall measured by platform crossing during the forward (**F**) and reverse (**G**) phases of the MWM probe test was similar in both genotypes (*P>0.05*; Control, *Arx* CKO: n=23, 19). (**H & I**) Control and *Arx* CKO displayed similar amount of freezing episodes during (**H**) and post (**I**) training in the contextual fear-conditioning paradigm (*P>0.05*; Control, *Arx* CKO: n=21, 19). (**J & K**) Exploration time of a novel object (**J**) and discrimination index (**K**) did not differ between control and *Arx* CKO mice during the novel object test (*P>0.05;* Control, *Arx* CKO: n=23, 19). The lower Q1 and upper Q3 quartiles of box plots (**H**) represent data outside the 5-95 percentile and dots outside this range denote outliers. Data are given as mean±SEM and analyzed by Two-way *ANOVA* (**A-C**) or Mann Whitney U test (**D-H**). Related to figure 3.

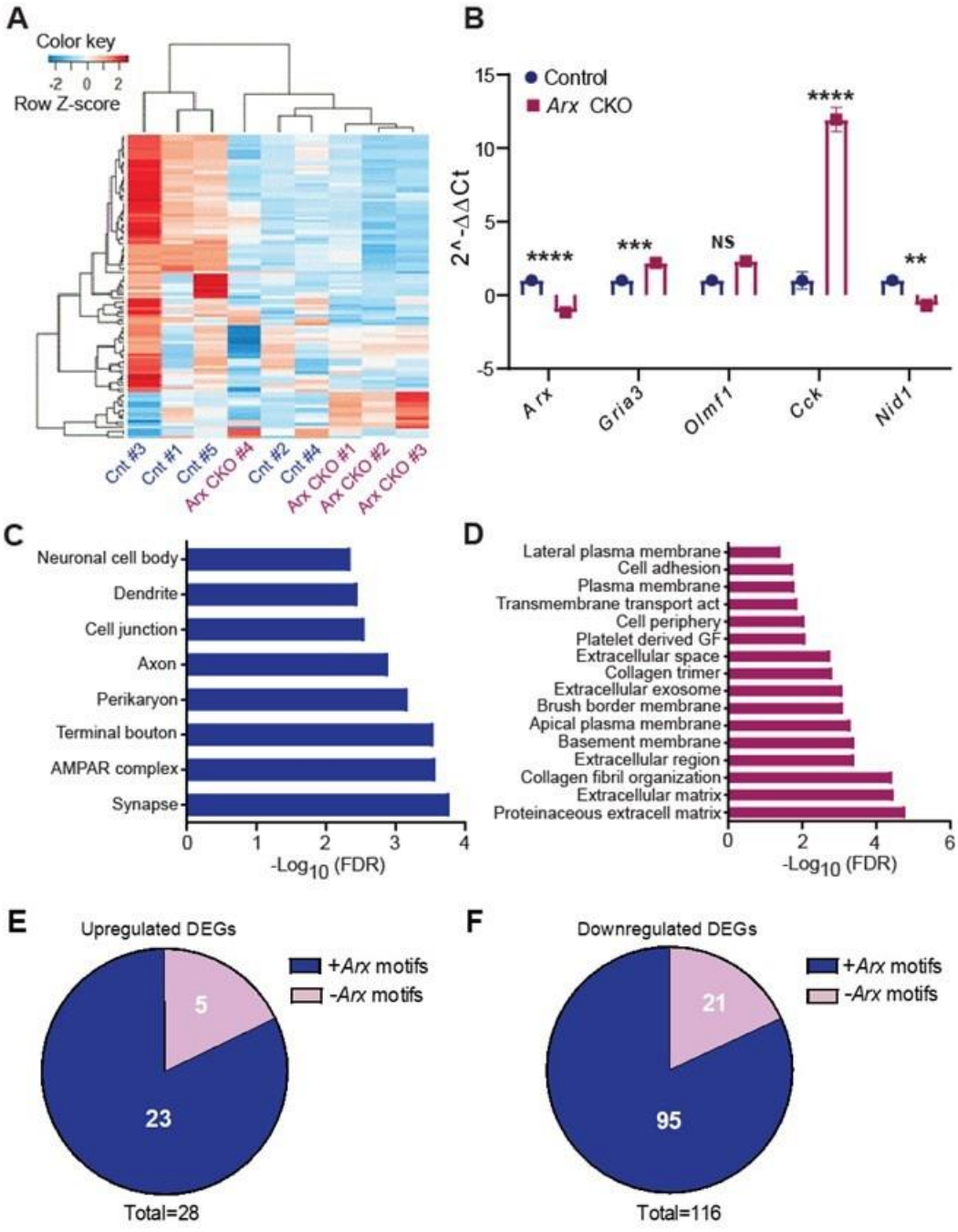
A
Color key
-2 0 2
Row Z-score
Cnt #3
Cnt #1
Cnt #5
Arx CKO #4
Cnt #2
Cnt #4
Arx CKO #1
Arx CKO #2
Arx CKO #3
B
Control
Arx CKO
2^-ΔΔCt
15
10
5
0
-5
****
***
NS
****
**
Arx
Gria3
Olmf1
Cck
Nid1
C
Neuronal cell body
Dendrite
Cell junction
Axon
Perikaryon
Terminal bouton
AMPAR complex
Synapse
0 1 2 3 4
-Log10 (FDR)
D
Lateral plasma membrane
Cell adhesion
Plasma membrane
Transmembrane transport act
Cell periphery
Platelet derived GF
Extracellular space
Collagen trimer
Extracellular exosome
Brush border membrane
Apical plasma membrane
Basement membrane
Extracellular region
Collagen fibril organization
Extracellular matrix
Proteinaceous extracell matrix
0 2 4 6
-Log10 (FDR)
E
Upregulated DEGs
+Arx motifs
-Arx motifs
5
23
Total=28
F
Downregulated DEGs
+Arx motifs
-Arx motifs
21
95
Total=116

Supplemental Figure 3. Validation of *RNAseq* and bioinformatics analyses of DEGs. (**A**) Separation of control and *Arx* CKO mice in a heat map of normalized gene expression for the top 100 DEGs by FDR values (FDR<0.05). Rows correspond to DEGs and columns to samples. (**B**) Selected RNAseq genes validated by quantitative real-time PCR normalized to18S RNA (*Adjusted P<0.0001*). (**C, D**) Functional GO enrichment analysis for upregulated (**C**) and downregulated (**D**) DEGs mostly revealed synaptic and ECM related associations (FDR<0.05). (**E, F**) Venn diagrams show that both upregulated (**E**) and downregulated (**F**) DEGs contained high proportion open chromatin regions with overlapping *Arx* binding motif. Transcriptomic data were from 5 control and 4 *Arx* CKO mice. Data analyzed by Benjamini-Hochberg FDR method (**A, C, & D**) and Two-way ANOVA followed by Sidak *post hoc* tests (**B**). *Symbols in **B** denote post hoc test significance levels: ***P<0.01, ***P<0.001, ****P<0.0001.* Related to figure 4.

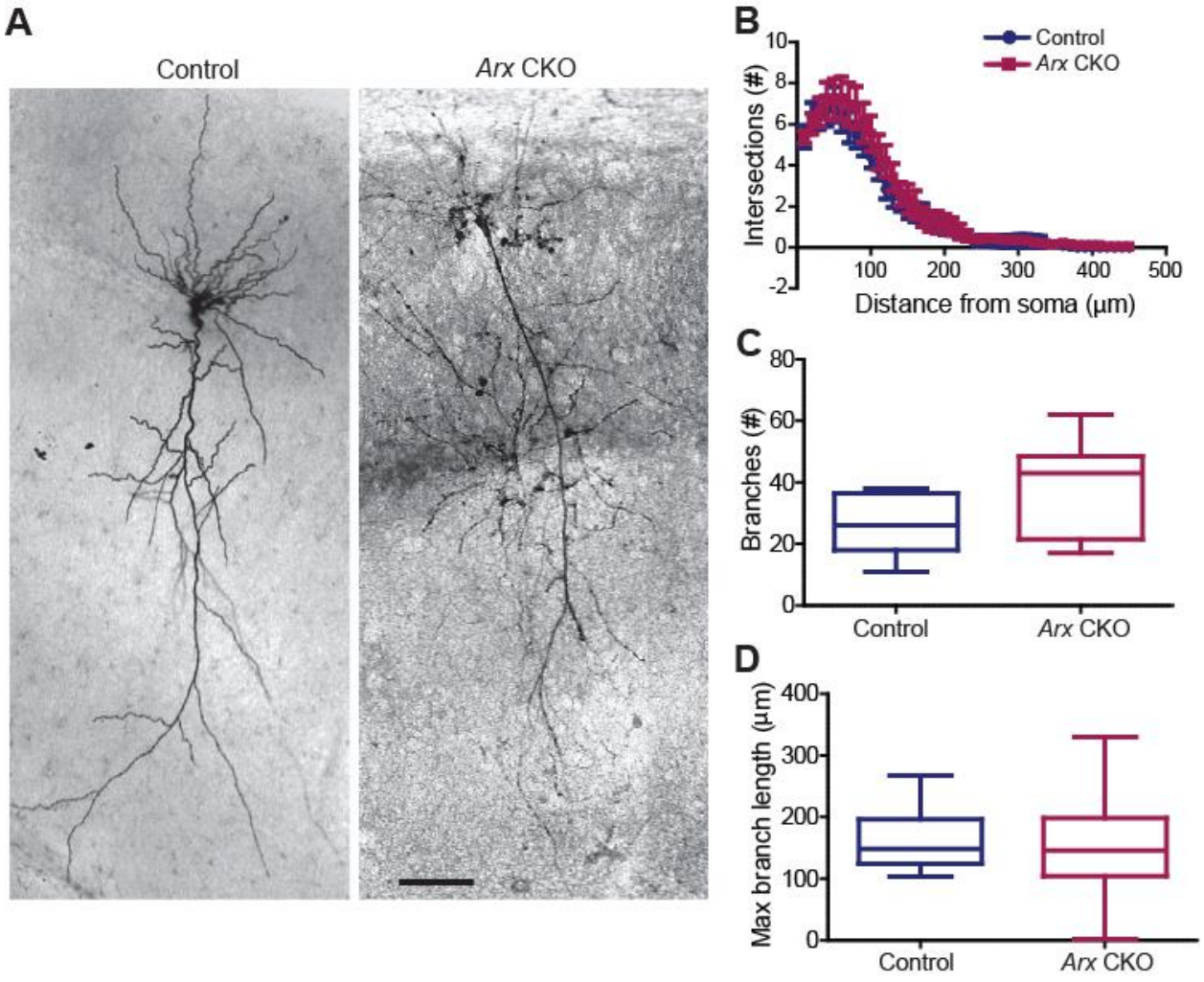
A
Control
Arx CKO
B
Control
Arx CKO
Intersections (#)
10
8
6
4
2
0
-2
100
200
300
400
500
Distance from soma (µm)
C
Branches (#)
80
60
40
20
0
Control
Arx CKO
D
Max branch length (µm)
400
300
200
100
0
Control
Arx CKO

Supplemental Figure 4. Unaltered PVI dendritic complexity in *Arx* CKO. (*A*) Representative photomicrographs of neurobiotin filled PVIs from control (Right) and *Arx* CKO (Left) mice. (**B**) The number of intersections along Sholl concentric circles did not differ between control and *Arx* CKO mice (*P>0.05*). (**C, D**) The number branches (**C**) and maximum branch length (**D**) in apical and basal dendrites were similar in control and *Ar*x CKO mice (*P>0.05*). Data were acquired from 10 mice in both control (n=10 cells) and *Arx* CKO (n=17 cells) mice and given as mean±SEM. Data analyzed by Two-way ANOVA (**B**) and by the unpaired, 2-tailed Student's *t* test (**C & D**). Scale bar: 100µm. Related to figure 6.

Up-regulated DEGs				
LAMP5	*CCK*	*TMEM59L*	*RPRML*	*CHGB*
DUSP14	*SV2B*	*MLIP*	*ZDHHC2*	*NRGN*
GRIA3	*LHFPL3*	*Gm11549*	*RALYL*	*LIN7B*
BDNF	*CACNG3*	*SLC7A3*	*HPCA*	*OLFM1*
A930003O13Rik	*NRN1*	*MAL2*	*CALB1*	*RTN1*
ST6GAL2	*NEUROD6*	*CPLX3*		
Down-regulated DEGs				
Duxf3	*ACOX2*	*GJB2*	*ADCY3*	*ACE*
COL8A1	*Car12*	*FAP*	*ABCC6*	*SEC24B*
SULF1	*Pcdhb22*	*CLDN2*	*VAT1L*	*COL6A1*
FZD6	*GLB1L2*	*DSG2*	*2610507I01Rik*	*F5*
SPAG16	*mycbpap*	*DMRT3*	*PIFO*	*SH3RF2*
SLC2A12	*CALML4*	*ANKEF1*	*PLEKHH2*	*IL31RA*
SLC22A2	*KRT18*	*SCIN*	*PCOLCE2*	*AQP1*
DDR2	*H2-Q1*	*TNS1*	*TMEM27*	*Slc6a20a*
rsph1	*LRRN4*	*SNAI3*	*FOXC1*	*4932438H23Rik*
PDE6G	*Olfr1030*	*4933429O19Rik*	*LEPR*	*TMEM217*
CDH5	*SLC22A12*	*COL1A2*	*HEYL*	*4930483J18Rik*
ADAMTS14	*TERT*	*Vmn1r13*	*Gm16548*	*CORO2B*
RECK	*DNAH11*	*COL1A1*	*EPN3*	*TTLL6*
Smok2a	*Glt28d2*	*SCARA5*	*PERP*	*A730043L09Rik*
Olfr1406	*Prl2c5*	*GUCY2C*	*IL1R1*	*KIF14*
KRT8	*PKD1L2*	*COL3A1*	*HYDIN*	*COL18A1*
STEAP4	*LAMB1*	*OTOG*	*Gm8096*	*WDR72*
PTGIS	*1700028P14Rik*	*MFAP2*	*FAM160A1*	*MYH11*
SEMA3G	*OBSCN*	*ARHGEF5*	*AEBP1*	*RD3*
Slco1a5	*CPN1*	*Ces2g*	*EPHX3*	*SLC22A6*
Zfp185	*MUC5B*	*iqgap1*	*THBS2*	*TGFB2*
Trp73	*PLB1*	*CPED1*	*DOCK6*	*SCN10A*
NID1	*Tas2r138*	*FN1*	*MFSD9*	*S1PR2*
SLC39A4				

Supplemental Table 1. List of up- and downregulated DEGs in PVIs with P values of <0.05 and fold change ≥2. Related to figure 4.

Function	FDR	Genes in network	Genes in genome
Regulation of synaptic transmission	8.52E-07	12	235
Glutamate receptor signaling pathway	2.75E-05	7	63
Ionotropic glutamate receptor complex	0.000113	6	47
AMPA selective glutamate receptor complex	0.000246	5	28
Axon development	0.000298	10	286
Neurotransmitter transport	0.000382	7	107
Regulation of neurotransmitter levels	0.000529	7	118
Regulation of synaptic plasticity	0.000529	7	119
Neuron-neuron synaptic transmission	0.000529	7	117
Postsynaptic density	0.000742	7	127
Neurotransmitter secretion	0.001055	6	84
Regulation of neuron projection development	0.00142	9	286
Ion channel complex	0.002278	7	156
Ionotropic glutamate receptor signaling pathway	0.002278	4	24
Glutamate receptor activity	0.002975	4	26
Transmembrane transporter complex	0.003052	7	168
PDZ domain binding	0.004556	6	116
Ephrin receptor	0.004678	4	31
Synaptic transmission, glutamatergic	0.004678	5	68
Perikaryon	0.004678	5	68
Ephrin receptor signaling pathway	0.00503	4	32
Synaptic membrane	0.005681	6	126
Postsynaptic membrane	0.01293	5	86
Regulation of dendrite development	0.018875	5	94
Dendrite development	0.018875	6	159
Axon guidance	0.019421	9	162
Neuron projection guidance	0.019421	6	162
Synaptic vessicle	0.021042	5	99
Extracellular-glutamate-gated-ion channel activity	0.024239	3	18
Regulation of neurotransmitter transport	0.024306	4	52
Calmodulin binding	0.027358	4	54
Dendritic spine	0.030039	5	111
Regulation of dendritic spine morphogenesis	0.030039	3	20
Neuron spine	0.031782	5	113
Regulation of dendrite morphogenesis	0.036896	4	60
Neuron recognition	0.048003	3	24
Dendritic spine morphogenesis	0.059734	3	26
Regulation of cell morphogenesis involved in differentiation	0.085075	6	226
Dendritic spine organization	0.087711	3	30

Supplemental Table 2. Biological functions identified in GeneMANIA functional networks of up-regulated DEGs (28 genes, FDR<0.05). Related to figure 4.

Function	FDR	Genes in network	Genes in genome
Extracellular matrix	2.05E-17	25	292
Extracellular matrix organization	3.79E-15	19	167
Extracellular structure organization	3.79E-15	19	168
Collagen fibril organization	7.99E-11	10	37
Extracellular matrix part	1.75E-10	14	127
Proteinaceous extracellular matrix	1.03E-10	15	179
Fibrillar collagen	2.30E-07	6	13
Extracellular matrix structural constituent	1.42E-06	6	17
Platelet-derived growth factor binding	1.41E-05	5	12
Collagen	2.02E-05	6	26
Basement membrane	0.000138	8	89
Protein heteromerization	0.001114	4	12
Brush border membrane	0.001517	6	54
Apical plasma membrane	0.003347	10	240
Growth factor binding	0.003517	7	99
Protein trimerization	0.005741	5	40
Cellular response to amino acid stimulus	0.006917	5	42
Collagen binding	0.007356	5	43
Brush border	0.007876	6	76
Response to amino acid	0.017109	5	52
Cellular response to acid	0.018931	6	90
Fibril organization	0.034106	3	11
Cell-substrate adhesion	0.042909	8	211
Structural molecule activity	0.051755	8	218
Wound healing	0.068008	8	228
Skin development	0.073807	8	232

Supplemental Table 3. Biological functions identified in GeneMANIA functional networks of down-regulated DEGs (144 genes, FDR<0.05). Related to figure 4.

Up-regulated DEGs with *Arx* binding sites near THS				
LAMP5	*CCK*	*TMEM59L*	*RPRML*	*CHGB*
RTN1	*SV2B*	*MLIP*	*ZDHHC2*	*NRGN*
GRIA3	*CACNG3*	*SLC7A3*	*RALYL*	*LIN7B*
BDNF	*NRN1*	*MAL2*	*HPCA*	*OLFM1*
DUSP14	*NEUROD6*	*CALB1*		
Down-regulated DEGs with *Arx* binding sites near THS				
COL8A1	*ACOX2*	*GJB2*	*ADCY3*	*ACE*
SULF1	*Car12*	*FAP*	*ABCC6*	*SEC24B*
FZD6	*GLB1L2*	*DSG2*	*VAT1L*	*COL6A1*
SPAG16	*mycbpap*	*DMRT3*	*PIFO*	*F5*
SLC2A12	*CALML4*	*ANKEF1*	*PLEKHH2*	*SH3RF2*
SLC22A2	*KRT18*	*SCIN*	*PCOLCE2*	*IL31RA*
DDR2	*LRRN4*	*TNS1*	*TMEM27*	*AQP1*
rsph1	*SLC22A12*	*COL1A2*	*FOXC1*	*Slc6a20a*
PDE6G	*TERT*	*COL1A1*	*LEPR*	*MFSD9*
CDH5	*Glt28d2*	*SCARA5*	*HEYL*	*TMEM217*
ADAMTS14	*Prl2c5*	*GUCY2C*	*EPN3*	*CORO2B*
RECK	*PKD1L2*	*COL3A1*	*PERP*	*TTLL6*
Smok2a	*NID1*	*MFAP2*	*IL1R1*	*4932438H23Rik*
KRT8	*1700028P14Rik*	*ARHGEF5*	*HYDIN*	*COL18A1*
STEAP4	*OBSCN*	*Ces2g*	*FAM160A1*	*WDR72*
PTGIS	*CPN1*	*iqgap1*	*AEBP1*	*MYH11*
SEMA3G	*MUC5B*	*CPED1*	*EPHX3*	*RD3*
Zfp185	*PLB1*	*FN1*	*THBS2*	*TGFB2*
Trp73	*Tas2r138*	*LAMB1*	*DOCK6*	*SCN10A*

Supplemental Table 4. List of up- and downregulated DEGs in PVIs with putative open chromatin regions with at least one overlapping *Arx* binding motif. Related to figure 4.

	Control	*Arx* CKO	*p*-Value
Passive properties			
RMP (mV)	-57.4±1.92	-60.9±1.6	0.1654
Capacitance (pF)	24.4 ± 2.0	37.8±6.6	0.0595
Time constant (ms)	6.6±0.86	6.84±0.95	0.8670
Input resistance(MΩ)	162.9±22.8	128.9±11.1	0.1892
Active properties			
Spike Amplitude (mV)	56.1±2.8	54.64±2.35	0.6861
Spike half width (ms)	0.65±0.05	0.63±0.09	0.8884
fAHP Amplitude (mV)	18.9±1.41	18.4±1.58	0.8205
n	20	20	

Supplemental Table 5. Summary of passive and active intrinsic membrane properties of PVIs. Values are given as mean±SEM and analyzed with the unpaired, two tailed Student's *t* test. Related to figure 6.

TRANSPARENT METHODS

Experimental animals and conditional knockout of *Arx* in PV interneurons

All animals were treated in accordance with relevant guidelines and regulations outlined in the National Institutes of Health Guide for the Care and Use of Laboratory Animals and approved by the Children's Hospital of Philadelphia Institutional Animal Care and Use Committee. Since *Arx* is an X-linked gene, we only used male mice in our studies. Mice were group-housed with up to five mice per cage after weaning at P21 and maintained on a 12 h light/dark cycle, at a temperature of 21±1°C, and controlled humidity (50-60%) with food and water provided *ad libitum*. To minimize suffering during the experiments, we limited the number of mice used in the study and the cohorts used were kept in normal thermal and enriched environments. As a result, all animal experiments were completed without the need to remove any subject due to obvious pain or discomfort.

Mouse strains used in this study included: PV^{Cre} mice [B6;129P2-Pvalbtm1(cre)Arbr/J; RRID:IMSR_JAX:008069; on a 129P2/OlaHsd background], the congenic TdTomato reporter Ai14 mice (Rosa-CAG-LSL-TdTomato; RRID:IMSR_JAX:007914), and the congenic strain $Arx^{LoxP/LoxP}$ generated for targeted deletion of exon 2 of the *Arx* gene following Cre recombination (Fulp et al. 2008). Both Ai14 and $Arx^{LoxP/LoxP}$ congenic lines were developed using ES cells derived from the 129S6/SvEvTac mouse strain and C57BL/6J blastocysts. All three strains were maintained on the C57BL/6J background. To generate *Arx* CKO mice, heterozygous PV^{Cre} mice were first crossed to homozygous Ai14 mice to generate PV^{Cre}; TdTomato mice. Female PV^{Cre} ;TdTomato double heterozygotes mice were then crossed to male $Arx^{LoxP/y}$ mice to generate $Arx^{flox/y}$;PV^{Cre} ;TdTomato (CKO) mice and $Arx^{Loxp/y}$;PV^{Cre} ;TdTomato littermate controls. Thus, both control and CKO mice used in this study were from the same 129P2/OlaHsd x 129S6/SvEvTac x C57BL/6J hybrid background, with the C57BL/6J being the predominant background strain. Genotypes of wild-type, floxed, TdTom, and cre-positive alleles were performed using standard end-point PCR using primers listed in key resources table (Fulp et al., 2008; Guo et al., 2000): Cre primers resulted in gene products of ~350 bp in both genotypes, whereas the tdTomato primers resulted in gene products of ~350 bp and ~270 bp in both control and CKO mice. However, the *Arx* primer set resulted in gene products of ~594 bp and ~637 bp in control and *Arx* CKO male mice, respectively.

EEG Recordings

EEG recordings from 8-10 weeks old control and *Arx* CKO male mice were carried out using standard techniques (Marsh et al., 2009). Mice were first anesthetized with a xylazine-ketamine solution (10 mg/kg xylazine and 100 mg/kg ketamine; administered i.p., Bayer, Leverkusen, Germany) and maintained with isoflurane (1-3%). Once adequate depth of anesthesia was achieved as demonstrated by lateral recumbences and absence of a withdrawal reflex to a toe pinch, the head of the mouse was secured in a stereotaxic apparatus (David Kopf Instruments, Tujunga, CA). Fur from the dorsal surface of the skull was removed using a depilatory cream (Nair Church & Dwight, Ewing, NJ) and the periosteum was exposed following a midline skin incision. The periosteum was scrapped back from the surface of the skull to expose the underlying lambda and bregma sutures. Four custom electrodes were built for cortical and hippocampal EEG recordings. The cortical electrodes (Three) were constructed by attaching 0.005 inch stainless steel wire (A-M systems, Carlsborg, WA) to self-tap screws (#0 × 1/8″, Small Parts Inc.). A mono-polar (0.005 inch) stainless steel wire (125µm; A-M systems, Carlsborg, WA) was used as the fourth or hippocampal electrode. The electrodes were then connected to Omnetics connectors (Omnetics connector corporation, Minneapolis, MN) and then drilled into the skull over the primary somatosensory cortex (left and right frontal, right

parietal) or durally inserted into the hippocampus through 2 mm diameter holes using the following stereotaxic coordinates: [from Bregma—Cortical: 1.0mm Anterior–Posterior (A-P) and 1.5 mm medial–lateral (M-L)] or [From Bregma-Hippocampus: −2.2 mm A–P, 2.0 mm M–L and 1.2 mm ventral]. Ground and reference electrodes were placed directly behind Lambda on either side of the midline. The electrodes were held in place with cold curing dental cement (Pro Base cold, Oral B Laboratories Pty Ltd, Maukau City, NZ) placed on the surface of the skull. Following the surgery, mice were allowed to recover in their home cage for 48 h prior to recordings. EEG signals and behavioral activity were simultaneously recorded using the Harmonie EEG system (Stellate, Montreal, Canada) for at least 72 hrs. The signals were filtered at a bandwidth of 0.1 KHz to 2 kHz and the sampling rate was set at 2 kHz with an anti-aliasing filter. Mice were allowed to acclimate to the recording environment for 30 min and had free access to water and food in the recording cages during the duration of the recordings.

Raw EEG traces from night and day recordings went through an automated amplitude-based detector after band-pass filtering within the 1–300 Hz range followed by a denoising step with a smart notch (SN) filter to eliminate minor background activities on the time-frequency map. The resultant EEG traces were manually inspected by an investigator blinded to the genotype of the mice and each file was screened to exclude high voltage artifacts from further analysis. Background signals from day and night recordings were analyzed in order to characterize the oscillatory features of background activity in the motor cortex and hippocampus. Power spectra for the whole EEG record or for epochs with high theta activities in the hippocampus was calculated using the spectral analysis function in MATLAB (MATLAB 2015b, Mathworks, Inc., Natick, MA). The analyzed spectra for the whole EEG record were quantified by calculating the power in selected bandwidths (Delta: 0.5-4Hz, Theta: 4–8Hz, Alpha: 8–12 Hz, Beta: 12–30Hz, and Gamma 30–50Hz dividing by total FFT power. To analyze high theta epochs in the hippocampus, we first identified the time points with high theta activity by calculating the theta ratio each time point. Specifically, the theta ratio was calculated by dividing the envelope amplitude of the theta-filtered signal by the sum of the envelope amplitude of the beta and delta signals. Using that approach, high theta epochs were identified using a 30ms moving window, if 20 out of the 30ms window had a theta z-score >2. For the 10 sec surrounding each high theta period, the power spectral density was calculated over the frequency range of 1-300Hz using a rectangular window. The data from all high theta epochs was used to calculate a mean power spectrum for each animal. In addition, each file was screened in order to detect seizures. Seizure segments were carefully reviewed to ascertain that the noted electrographic changes were associated with behavioral seizures rather than with movement artifacts. Electrographic seizures were identified according to the following set of criteria: rhythmic and repetitive spikes of amplitude of 1.5x baseline, frequency of 5-10 Hz, and lasting more than 5 sec (Marsh et al., 2009). In addition, periods of high voltage transient spikes followed by short periods of reduced EEG amplitude or paroxysmal background attenuation were considered as electrographic seizures (Marsh et al., 2009).

Behavioral Studies

Behavioral testing started when the mice were 8 weeks old and by the end of the test battery they were approximately 11 weeks old. The behavioral test battery consisted of eight tests, which were conducted in normal room illumination. To minimize potential carry-on effects, the order of the tests and inter-test interval (3 days) were kept constant. All testing was conducted during the light-phase between 0900 and 1400 h to eliminate variability in performance due to time of day. Three different cohorts of mice were used, with each cohort consisting of approximately an equal mix of control and *Arx* CKO mice from at least two different littermates. The mice were handled for 5 min each day for 3 days prior to the initial test battery. Additionally, they were habituated to the testing environment for at least 30 min before commencing each behavioral test. The apparatus used for each test battery was cleaned with

germicidal disposable cloth (Sani-Cloth Plus) between each mouse to ensure identical experimental conditions for each test mouse. All behavioral tests, except the grip strength and rota-rod tests, were video-recorded and automatically scored using the ANY-maze software (Stoelting Co., Wood Dale, IL). Experimenters were blind to the genotype of the mice during behavioral testing and quantification. The numbers of mice per genotype in each test are indicated in the figure legends.

Rotarod: Motor coordination and learning were measured by the accelerating rotarod test (Hirata et al., 2016; Simonet et al., 2015). Mice were first given a test trial on the rotarod apparatus (Ugo Basile, Model 47600, Comerio, Italy) at a constant low rotation speed (4 rpm) in order to learn how to walk on the rod. Once they were comfortable with walking on the rod, the test began by accelerating the apparatus from 4-60 RPM over a 300 sec period. Mice were tested over 4 consecutive days, with each daily session consisting of 5 trials separated by approximately 30 min. The latency to fall from the rod was automatically recorded for each test mouse. Learning rate for each daily session was calculated using the following formula: (mean latency to $\text{fall}_{\text{trials 4 and 5}}$) − (mean latency to $\text{fall}_{\text{trials 1 and 2}}$) / (number of intertrial intervals).

Grip Strength: Forelimb and hindlimb grip strength of control and *Arx* CKO mice were tested using a grip strength meter (080312-3 Columbus Instruments, Columbus, OH, USA) (Simonet et al., 2015). For forelimb testing, mice were held at the proximal part of the tail and allowed to grasp a horizontal metal bar with both paws. The mice were then steadily pulled away and the pull force recorded once the mice unclasped the metal bar. For the hindlimb grip strength measurements, mice were allowed to grab the horizontal bar with their hindlimb paws while facing away from the meter and the tails were steadily pulled directly toward the meter until their grasps broke. Measurements were discarded if the mice failed to use both fore- and hindpaws, turns backwards during the pull, or broke their grasps without resistance. Six consecutive trials within 2 min each were performed for each mouse, with the first three trials for the forelimb strength and the last three trials for the hindlimb paws. The averaged values for the fore- and hindlimbs were taken for further analysis (Simonet et al., 2015).

Morris Water Maze (MWM): Testing of spatial learning and memory was performed in the MWM with standard protocols and paradigms (Simonet et al., 2015). The water maze consisted of a circular swimming pool (128 cm in diameter) made of green plastic. The pool was filled with water (24-25°C) to within 15-20 cm from the top and an elevated escape platform (15-cm^2 Plexiglas square) was submerged 0.5-1.0 cm under the water level. To prevent the mice from seeing the submerged escape platform, the water was made opaque by the addition of non-toxic white tempera paint. We first assessed the performance of the control and *Arx* CKO in reference or forward learning to determine their ability to learn the spatial relationship between distant cues and the escape platform. Several pictures of black and white geometrical shapes were placed around the pool as spatial cues and these pictures remained in the same position throughout the testing periods. To facilitate acquisition and analysis, the pool was divided into 4 quadrants: east (E), west (W), north (N), and south (S). The escape platform was then placed in the center (16 cm from the wall) of the southwest (SW) quadrant of the pool and remained there throughout learning sessions. Four distinct mouse drop locations (N, SE, NW, and E) were used for each daily trials. Reference testing was done over 5 consecutive days with each daily session consisting of four 60 sec trials, but the order of the start locations was changed from day to day to prevent mice from developing fixed motor patterns. However, the ultimate start location patterns used in the first reference learning cohort were used in all other cohorts. Mice that failed to locate the platform during reference trials were gently guided to it. Once on the platform, each mouse was given a 10 s of post-trial time to re-orient to the visual cues around the pool before returning to their cage. The day after the completion of the last daily learning

sessions, we assessed spatial memory using the probe test of the MWM. During this probe test, the escape platform was removed and the mice were allowed to freely swim for 60 seconds from the NE start location. After 1 day of rest following completion of the probe test, mice were subjected to reversal learning over 5 consecutive days to test their ability to purge and learn new strategies. In contrast to forward learning, the escape platform was placed in the northwest quadrant (16 cm from the wall) of the pool for the reversal learning tests, but the start locations and patterns were exactly the same as in the forward learning tests. A reversal probe test was performed a day after the completion of the last daily reversal learning sessions and the start location was NE as in the forward probe trial. To minimize bias and mitigate stress in all testing paradigms, mice were gently placed in the water facing the wall of the pool. In addition, upon removal from the pool, mice were always placed in warming cage with dry paper towel under a heat lamp for at least 5 min before returning to their home cage. All mice within a cohort completed one trial before the second trial was conducted. Given the size of our cohorts, the inter-trial interval was approximately 30 min in all multi trials testing. The swim path of each mouse during all the MWM tests was recorded using a camera connected to the ANY-maze video tracking software. Learning ability during both reversal and forward learning was measured by the daily mean of escape latency (in sec). Spatial memory for the platform location during probe testing was evaluated by the number of swims or crosses over the platform site in the target quadrant.

Contextual Fear Conditioning: Fear conditioning test was performed over a 2-day period (Simonet et al., 2015). On the first day, mice were placed individually in the fear conditioning chamber (Model ENV-307W, Med Associates, Inc., Georgia, VT, USA) and allowed to freely explore the novel environment for 3 min before a 2-s foot shock (1.12 mA) was given. The mice remained in the chamber afterward for another minute before returning to their home cage. On the second day, the mice were placed back in the fear conditioning chamber and video-recorded for 5 min using the ANY-Maze software (Stoelting Co. Wood Dale, IL). Freezing episodes were automatically recorded and given as total episodes during the duration of testing or as freezing episodes per 1 min bins. Fear learning was measured by the initial freezing ratio (Post shock freezing episodes/total pre shock freezing episodes) and by total freezing ratio (Sum of 5 normalized 1 min segments) on day 2 of testing. For normalization of each 1 min segment, freezing episodes in each 1 min segment of day 2 were divided by the mean freezing episodes of three 1 min segments recorded prior to delivery of the 2-s foot shock. This approach to normalization was necessary because of the difference in duration between pre-shock (3 min) and day 2 post-shock (5 min) recordings.

Novel object recognition: The novel object recognition test was performed in an open field box (53cm wide x 53cm long x 22 cm high walls) made of opaque Plexiglass in order to obscure spatial clues around the room. To minimize stress, we used low and diffuse lighting, with the center of test apparatus illuminated around 20 lux. The test consisted of a training and a novel recognition session for each mouse with intersessions interval of 24hr, during which the mice were returned to their home cages in the holding room. During the training session, each mouse was presented with two identical objects placed near the center of the open field apparatus and the mouse was allowed to explore for 5 min. The following day during the novel recognition session, one of the identical or familiar objects was replaced with a novel object and each mouse was allowed to freely explore for 5 min. Both novel and familiar objects were of similar structure and size, but the novel object had a distinctive shape and color. To avoid the use of odor cues, the presented objects were thoroughly cleaned prior to each test animal. The time spent exploring the objects was recorded with a camera mounted above the open field apparatus. Recognition memory was measured by the ratio of time spent exploring the novel to the familiar object.

Open field: The open field test was conducted in a clear Plexiglas chamber (53cm wide x 53cm long x 22 cm high walls) in a standard lit room with constant illumination of about 300 lux at the level of the test apparatus (Simonet et al., 2015). Mice were placed in the center of the chamber and allowed to freely explore for 15 min. Activity in the open field was recorded and scored using ANY-Maze. Parameters measured by ANY-Maze included total distance travelled (m) or time (Sec) in the center zone in 5 min bins. ANY-Maze defines the peripheral zone as a 13 cm wide corridor along the wall of the open field chamber. The acclimatization ratio (Bin 2/Bin 1, Bin 3/Bin 1, and Bin3/Bin 2) of center zone distance to total distance travelled was used as an index of anxiety. To further measure anxiety, fecal boli left in the chamber were removed and quantified after the test period.

Elevated plus-maze: The elevated plus-maze apparatus consisted of four arms (50 x 12 cm) extending from a central junction (12 x 6 cm). Two of the four arms were enclosed by 40 cm high walls and the remaining two or open arms were surrounded by 0.3 cm high rims to prevent the mice from falling. The maze was elevated 40 cm above the ground and testing was performed in a standard lit room with light conditions around the open and closed arms about 300 and 30 lux, respectively. Mice were placed individually in the center junction facing an open arm and allowed to freely explore the maze for 5 min. The percentage of time spent in the open arms was taken as an index of anxiety-related behaviors.

Genome-wide Sequencing

Tissue dissociation: Juvenile *Arx* CKO and control male mice (postnatal day 35-40) were anesthetized with isoflurane and the whole brain from each genotype was extracted and quickly transferred to an iced cold (0–4 °C) sucrose aCSF containing in (mM): sucrose 204, KCl 2.5, $CaCl_2$ (Anhydrous) 0.5, $MgSO_4$ (Anhydrous) 10, NaH_2PO_4 1.25, $NaHCO_3$ 26 and glucose 11, Na-Ascorbate 5, Na-Pyruvate 3, and Thiourea 2. The sucrose ACSF was maintained at 315 mΩ and oxygenated with a mixture of 95% O_2/5% CO_2 to maintain a pH close to 7.4. After bilateral removal of the olfactory bulbs as well as the cerebellum transverse slices (350µm) were prepared in the same ice-slushy sucrose ACSF using a Leica vibratome (VT1200, Leica, Germany). To collect sufficient number of TdTom+ cells for RNA seq screens, cortical and hippocampal brain regions were micro-dissected in a recovery aCSF containing in (mM): NaCl 128, KCl 2.5, $CaCl_2$ (Anhydrous) 0.5, $MgSO_4$ (Anhydrous) 10, NaH_2PO_4 1.25, $NaHCO_3$ 26 and glucose 11. Hippocampal and cortical tissue was then dissociated into a single cell suspension using the Papain dissociation system (Worthington) following the manufacturer's instructions. Each solution in the kit was supplemented with trehalose (50 mg/ml), a disaccharide that has been shown to maintain cell viability during heat stress and cryopreservation (Saxena et al., 2012). All solutions were oxygenated for at least 30 minutes with a mixture of 95% O_2/5% CO_2 prior to use. After dissociation, cell pellets were resuspended in 2 ml of neural basal-BSA and kept on ice prior to FACS analysis. After dissociation of hippocampal/cortical tissue and confirmation of cell viability under a fluorescence microscope, TdTom+ cells were FACS sorted using the Beckman Coulter MoFLo Astrios Cell Sorter using a 100µm nozzle in the single-cell sorting mode. We collected an average of 120,842 TdTom+ cells (n = 4 control & 5 *Arx* CKO mice) from the micro-dissected cortical/hippocampal tissues for RNA extraction. To mitigate RNA degradation, sorted cells were collected in neural basal-BSA and directly lysed in Trizol LS (25:75 ratio, manufacturer's instruction). RNA extraction was the carried out using the chloroform method according to the extraction kit instructions (TRIzol Reagent, Invitrogen, Carlsbad, CA, USA). In addition, 0.3 M sodium acetate (1/10th of the reaction volume) was used to increase RNA yield. Isolated RNA had an average integrity (RIN) score of 7.9 as measured by the Agilent 2100 Bioanalyzer system (Agilent, Santa Clara, CA USA).

Transcriptome library construction and sequencing: Total RNA extracted from control and *Arx* CKO male mice cells were submitted to the Next-Generation Sequencing Core of the University of Pennsylvania for cDNA amplification, library preparation, and sequencing using the Ovation RNA-seq v2 and Rapid DR Multiplexing kits (NuGEN). Whole mRNAseq libraries were prepared from 9 mice (5 control and 4 *Arx* CKO mice) using the SMARTer Ultra Low RNA Kit for Illumina Sequencing (Clontech, Cat#634936) according to manufacturer's instructions. Standard methods to assess sample quality (Agilent Bioanalyzer, Kappa Biosystems Library Quantification kit, Qubit® Fluorometer) and measure cDNA concentration were used. A total of 1ng of amplified cDNA for each sample was used as input to build the sequencing libraries. Whole mRNAseq libraries from control and *Arx* CKO mice were quantified using Agilent Bioanalyzer DNA 7500 chips. Libraries were sequenced on the Illumina HiSeq 4000 2 × 100 (Illumina, San Diego, CA, USA) to generate 150bp paired end reads, yielding approximately 20-40 million reads per sample (~80 million reads per lane).

Read Alignment, Quantification, Differential Expression, and GO Analysis: Raw sequence reads were aligned to the mouse genome and initially analyzed by the Next-Generation Sequencing Core of the University of Pennsylvania using the standard Illumina sequence analysis pipeline. Some mRNA samples were sequenced twice, but their resulting libraries were aligned separately before merging into a single mean read count matrix of mapped genes for all the samples (Marioni et al., 2008; McIntyre et al., 2011). Initial analyses included determinations of RNA-seq data quality control (QC) of results and expression levels for all mapped genes. After filtering genes with no read counts, an average count matrix of over 25K genes was generated and analyzed for differential expression. For evidence of differential expression between control and *Arx* CKO mice, we applied standard approaches to analysis and normalization of the filtered count data using the Bioconductor DESeq2 (Love et al., 2014) package [https://www.bioconductor.org] in the R environment. DEseq2 uses a shrinkage estimation algorithm for dispersions and fold changes, allowing for improved stability and interpretability of read counts. Differential gene expression was then analyzed using the standard parameters in DESeq2 and a threshold of false discovery rate (FDR) < 0.05. The Benjamini-Hochberg procedure (FDR) was used as the default option in DESeq2 for the adjustment test for P-value. A gene was considered differentially expressed when the $\log_2$ fold enriched was ≥ 1 and an adjusted *P-value* or FDR<0.05. To identify the cellular processes regulated by postnatal *Arx* in PVIs, we applied gene ontology (GO) analysis to examine the functional attributes of DEGs using the Database for Annotation, Visualization and Integrated Discovery (DAVID) (Huang da et al., 2009a, b). Separate GO analyses for functional annotations of the upregulated and downregulated DEGs were performed (FDR < 0.05).

Network analysis: To construct gene-gene interaction networks for the DEGs, we used the GeneMANIA-cytoscape app [http://apps.cytoscape.org/apps/genemania] (Montojo et al., 2014). GeneMANIA is a web-based prediction server for the prediction and prioritization of gene/protein function on the basis of multiple networks derived from published proteomics and genomic data (Warde-Farley et al., 2010), whereas cytoscape provides a platform for visualizing and integrating these networks with gene expression profiles (Shannon et al., 2003). DEGs were imported into the GeneMania database of previously discovered networks and screened for gene-gene interactions. Functional gene-gene associations such as constructed based on co-expression, co-localization, physical interaction, predicted interaction, shared protein domain, and other functional relations were assessed. The strength and significance of gene networks between DEGs and associated genes was determined by a GO term (biological process)-based weighting algorithm, which was then was filtered to include only gene-gene interaction networks above a significance FDR threshold of 0.05.

Arx binding Motif analysis: The occurrence of *Arx* binding motifs in open chromatin regions identified in DEGs was performed with Cistrome Analysis Pipeline (v 3.4.0) [http://cistrome.org/ap/] in combination with UCSC Genome Table browser [https://genome.ucsc.edu/] (Karolchik et al., 2004; Liu et al., 2011). Analysis was conducted using the mouse database and the up- and down-regulated DEGs were analyzed separately. Briefly, PVI specific ATAC motifs near DEGs were defined as areas of open chromatin within ±100Kb flanking regions of each DEG TSS. Screen motif tool in Cistrome was used to scan these regions for *Arx* binding motifs using the positional weight matrix in TRANSFAC for Arx (Motif ID: M01423). Analysis of *Arx* binding motifs in identified ATAC-seq regions was performed using GREAT (v3.0.0) algorithm (McLean et al., 2010) with standard parameters [http://great.stanford.edu] to determine distance of motifs sites from the TSS. For a more unbiased view of the occurrence of *Arx* binding motifs in DEG ATAC-seq regions, we conducted overlapping analysis using randomly matched genomic regions generated in RSAT. These genome-wide and computationally generated matched regions were used as control for prevalence of *Arx* binding motifs in DEG ATAC-seq regions.

Validation of RNA-Seq results with RTqPCR

To verify the RNA-Seq results, we conducted RTqPCR analysis using new RNA samples as opposed to those used in the RNAseq experiments. RNA was isolated using the Trizol LS/Chloroform method (TRIzol Reagent, Invitrogen, Carlsbad, CA, USA) as in the case of the samples used for RNAseq. First strand cDNA was prepared using the Invitrogen superscript kit (Invitrogen, life technologies, USA) with random primers according to the manufacturer's instructions. Quantitative analysis of real-time PCR was conducted for *Arx* and the following DEGs: *Gria3, Olfm1, Cck, and Nid1*. All RTqPCR reactions were performed with the TaqMan assay RTqPCR System according to manufacturer's instructions (Applied Biosystems, USA) using the following probes: Mm01237524_m1 (*Arx*), Mm00497506_m1 (*Gria3*), Mm00444666_m1 (*Olfm1*), Mm0044170_m1 (*Cck*), Mm00477827_m1 (*Nid1*), and Mm03928990_g1 (18S ribosomal RNA).The real time cycler (Applied Biosystems; 7500 fast) was employed for all PCR reactions using the following standard conditions: 50°C for 2 min, 95°C for 10 min, and 40 cycles of denaturation at 95°C for 15 sec and annealing and extension at 60°C for 1 min. Efficiency and specificity of amplification with the Taqman probes were confirmed by analysis of standard and melting curves, respectively. Transcript levels for the analyzed genes were normalized to the stably expressed housekeeping gene 18S ribosomal RNA (RRN18S) and relative expression levels were calculated by the $2^{-\Delta\Delta CT}$ method (Livak and Schmittgen, 2001).

Histology

Fixed brains from 8-10 weeks old *Arx*; PV^{Cre}Tom mice and *Arx*; PV^{Cre}Tom CKO mice were analyzed by immunohistochemistry (Marsh et al., 2009). Mice were anesthetized with a mixture of ketamine (100mg/kg) and xylazine (10mg/kg) administered intraperitoneally (ip) followed by isoflurane (1-3%). Anesthetized mice were then perfused transcardially with PBS followed by 4% paraformaldehyde in 0.1 M phosphate buffer (Sigma, St. Louis, MO), pH 7.4. The brains were removed and post-fixed in 4% phosphate-buffered paraformaldehyde at 4°C overnight and incubated in 30% sucrose until the brains sink to the bottom. Brains were then embedded in optimal cutting temperature compound (OCT, Tissue-Tek; Electron Microscopy Sciences, Hatfield, PA) and immediately frozen on dry ice (78.5°C). Coronal sections (14µm) were cut using a cryostat (Leica HM 500; Heidelberg, Germany) and stored at -80ºC until immunostaining. To assess Cre-recombination efficiency, the integrity of the PNN, and the density of interneuron subtypes following loss of Arx, sections containing the hippocampus were processed for immunolabeling with antibodies using a two-day protocol. Briefly, cryosections were rinsed twice in PBS and nonspecific binding was blocked by incubation in 10% normal

goat serum in 0.5% Triton X-100 10% normal donkey serum 0/1% triton-100X for 1h at RT. Sections were then incubated with antibodies against ARX (1:100, Neuromab, Davis, CA), Cat-315 (A gift from Rick Matthews of Syracuse University, 1:10), Aggrecan (ACAN, Millipore Sigma, Burlington, MA), parvalbumin (PV, 1:100, Millipore Sigma), calbindin D28k (CB, 1:500, Swant, Marly, Switzerland), Somatostatin (SST; 1:50, ABCAM, Cambridge, MA), and calretinin (CR, 1:100; Swant, Marly, Switzerland) overnight at 4ºC. For antibodies that required antigen retrieval, slides were placed in citric acid buffer and autoclaved at 105ºC for 20 min. The mouse on mouse (M.O.M) kit was used for staining with antibodies raised in mouse in order to minimize nonspecific binding between primary antibodies and mouse tissue. To detect primary antibodies, sections were then incubated with secondary IgM or IgG antibody conjugated to fluorescein and/or biotinylated secondary followed by Cy3 streptavidin (1:50; Jackson Immuno Research Lab, West Grove, PA) for 30min at RT. Sections were then washed with PBS, air-dried, and mounted with Vectashield mounting medium (Vector Laboratories, Burlingame, CA).

Cell counting and pixel analysis

Immunofluorescence images containing the hippocampus were acquired using a Leica DMR microscope coupled with a CoolSNAP camera (Leica Microsystems, Bannockburn, IL). All images were analyzed using Image J (NIH). Double fluorescent Images were captured from both hemispheres using a 10X or 20X objective without altering the focal plane when switching filter cubes. Co-localization was determined by examining ARX- or TdTom+ interneurons for PV, SST, CB, NPY, or CR. Cell counts were performed on 10X images stitched into a montage containing all brain structures. The perimeter of the counting area of interest was drawn and the density of cells (Cells per mm^2) for each animal was calculated by dividing the number of positive cells by the total area sampled. Cell density for matched slices was calculated in 3-7 mice for each genotype and the median value for each mouse was compared across genotypes. Cell counts were performed by three individuals blinded to the genotype of the mice. Pixel counts were obtained for ACAN using the immunohistochemistry profiler (IHC) plugins for Image J.

Electrophysiology

Hippocampal slice preparation: Juvenile *Arx* CKO and control male mice (PND 35-40) were anesthetized with isoflurane and then transcardially perfused with ice cold (0–4 °C) sucrose aCSF containing in (mM): sucrose 204, KCl 2.5, $CaCl_2$ (Anhydrous) 0.5, $MgSO_4$ (Anhydrous) 10, NaH_2PO4 1.25, $NaHCO_3$ 26 and glucose 11, Na-Ascorbate 5, Na-Pyruvate 3, and Thiourea 2. The sucrose ACSF was maintained at 315mΩ and oxygenated with 95% O_2, 5% CO_2 to maintain a pH close to 7.4. The whole brain was rapidly removed and immersed in ice-slush sucrose artificial cerebrospinal fluid (ACSF) and allowed to cool for 2-3 min to reduce anoxia and promote cell survival. Transverse hippocampal-entorhinal cortex slices (350µm) were prepared in the same ice-slushy sucrose ACSF using a Leica vibratome (VT1200, Leica, Germany). Slices were allowed to recover in a chamber with recovery aCSF (115mM NaCl, 2.5mM KCl, 1mM $MgSO_4$, 2.5mM $CaCl_2$, 1.4mM NaH_2PO_4, 30.8mM $NaHCO_3$, 15.5mM glucose, 5mM NaAscorbate, 3mM NaPyruvate, and 2mM Thiourea) equilibrated with 95% O_2/5% CO_2 for 45 min at 32ºC and then for 1h at RT prior to recordings. Following recovery, dorsal hippocampal slices were transferred to a submerged chamber (RC-27, Warner Instruments) and were continuously perfused with oxygenated recording aCSF (128mM NaCl, 2.5mM KCl, 1mM $MgSO_4$, 2.5mM $CaCl_2$, 1.4mM NaH_2PO_4, 30mM $NaHCO_3$, 15.5mM glucose) with a flow rate of 2mL/min using a gravity-driven perfusion system. Slices were visualized on a screen via a charge-coupled device (CCD) camera system (Rolera, Qimaging) attached to the Olympus BX51WI microscope (Olympus, USA). All recordings were performed at 32°C.

Intrinsic and basal synaptic properties: Whole-cell recordings were made on visually identified tdTom+ PVIs from Juvenile *Arx* CKO and control male mice (PND 35-40) using a 40× water immersion objective and near-infrared differential interference contrast (IR-DIC) video microsopy. CA1 TdTom+ PVIs were first identified under fluorescence then patched using IR-DIC (BX-51WI, Olympus, USA). Patch pipettes (4–6 MΩ) were pulled from thick-walled borosilicate glass (ID: 1.1 mm, OD: 1.5; WPI, Sarasota, FL) using a horizontal puller (Sutter Instruments P-97) and filled with (in mM) 5 KCl, 135 K-gluconate, 2 NaCl, 10 HEPES, 4 EGTA, 4 MgATP, and 0.3 Na_3GTP (pH ≈ 7.2; 285 mΩ). Neurobiotin (0.5%; Molecular Probes, Eugene, OR) was added to the solution for later morphological identification of the recorded neurons. The liquid junction potential between the recording ACSF and internal solution was effectively cancelled out using the bridge balance circuit of the amplifier before sealing onto cell membrane. All voltage- or current-clamp recordings were performed with a Multiclamp 700B amplifier (Molecular Devices, USA) connected to a Digidata 1440A analog-digital converter (Molecular Devices, USA). Signals were sampled at 20 kHz and filtered with a 5 kHz low-pass Bessel filter. To reduce or eliminate artifacts in the recordings, series resistance and capacitance compensation (70–80%) were performed online to decrease the transient observed under a rectangular test pulse. Patch quality was continuously monitored throughout the experiments and only recordings obtained from patches with stable holding current (<100pA) and access resistance (<30 MΩ) were analyzed. Passive intrinsic membrane properties (Input resistance (Rin), RMP, membrane tau,) and active (AP threshold, AP amplitude, and half-width duration, sag, firing frequency) were measured upon establishment of whole mode. Intrinsic membrane properties of TdTom+ PVIs were subsequently characterized in response to hyper- and depolarizing rectangular current steps applied for 500 ms in 10 to 20pA increments at 0.5 Hz in the current-clamp recording mode. The membrane time constant was determined by single-exponential fitting to the average voltage responses activated by hyperpolarizing current steps (10-20 pA). All AP measures were taken from the first AP of the first sweep that reached the spike threshold. Peak amplitudes of the AP and the fast after hyperpolarization (fAHP) amplitude were measured relative to the AP threshold. Duration of the AP was measured at its half-amplitude.

Synaptic recordings of spontaneous or miniature excitatory/inhibitory currents were simultaneously recorded for 5 min by clamping the membrane at -40mV (Zhou et al., 2009) following the acquisition of intrinsic membrane data. Miniature excitatory synaptic currents (mEPSCs) and inhibitory synaptic currents (mIPSCs) were recorded by the addition of 0.5µM tetrodotoxin (TTX) to the ACSF. The peak amplitude and frequency were determined for excitatory and inhibitory spontaneous or miniature events. All data were recorded using Clampex 10.7 (Molecular Devices, USA) and analyzed using Clampfit 10.7 (Molecular Devices, USA) or Minianalysis 6.0.3 (Jaejin software, Leonia, NJ, USA).

Evoked synaptic transmission: CA1 evoked synaptic responses were recorded from on visually identified tdTom+ PVIs from Juvenile *Arx* CKO and control male mice in the whole-cell patch clamp mode as described for the intrinsic and synaptic recordings above. Patch pipettes were filled with an internal solution containing (in mM): $CsMeSO_4$ 125, QX314.Cl 5, HEPES 10, NaCl 4, EGTA 1, MgATP 4, Na_2GTP 0.3, phosphocreatine 10. Synaptic responses were evoked by stimulation of the Schaffer collateral fibers in the SR with a tungsten concentric bipolar electrode as described in the field recording section above. For recording glutamatergic and GABAergic currents in the same cell, synaptic currents were recorded at 0 mV (glutamatergic reversal potential) and − 60 mV (GABAergic reversal potential). For construction of input-output curves for synaptic strength and kinetics, synaptic events (6-10) were evoked 0.1 Hz to minimize synaptic failures. To measure short-term plasticity, a form of facilitation or depression of synaptic response, the half-maximal stimulus intensity was used to assess paired-pulse facilitation and inhibition at intervals of 50, 100, 150, and 200ms. Mixed NMDA/AMPA EPSCs

were evoked in 1mM Mg^{2+} ACSF with bicuculline (50μM) and glycine (50μM) at membrane voltages ranging from -90 to +50 mV (10 mV steps) at 0.1Hz. We confirmed that this stimulation paradigm did not induce LTP by comparing EPSC amplitudes from the beginning to the end of each recording session. To differentiate AMPA and NMDA receptor currents, the time of the peak current at –90 mV, considered to be fully AMPAR-mediated glutamate current, was used to establish the time window for measuring the peak AMPAR currents evoked while cells were clamped at the aforementioned membrane potentials (Myme et al., 2003). The decay to baseline portion of the waveform at -90mV was used to establish a 15ms window for the measurement of NMDAR-mediated glutamate current at those membrane potentials (Myme et al., 2003). Values obtained from this approach were used to construct the I-V relationship curves for both AMPA and NMDA currents. The currents measured at -50 and +50mV were used to calculate the ratio of NMDA/AMPA ($I_{NMDA\ at\ +50mV}/I_{AMPA\ at\ -50mV}$) currents as well as their rectification indices (Matta et al., 2013). All evoked recordings were analyzed in Clampfit 10.7 and the paired pulse ratio was calculated by dividing the mean amplitude of eEPSC or eIPSC of the second pulse by the mean amplitude of the first pulse (Pulse 2/pulse 1).

Neurobiotin filling and Sholl analysis

Following the intrinsic and basal synaptic recordings, TdTom+ PVIs were filled with neurobiotin (0.5%, in intracellular solution) through a combination of diffusive and current-induced (300pA current step at 10Hz for 5 min) loading via the patch pipette. The patch pipette was then slowly retracted from the cell soma and the slice was transferred to a chamber with bubbling ACSF at 32^0C for about an hour to allow for complete diffusion of neurobiotin. To prevent overlapping of processes with neurobiotin labeling, only one to three cells were filled per slice. Slices were subsequently fixed overnight at 4°C in 4% paraformaldehyde containing 0.3% picric acid. To begin recovery of neurobiotin labeling, slices were washed 3 times for 10 min each in 100mM Tris buffer and treated with 1% H_2O_2 in 0.1 M Tris buffer for 30 min. After 3 washes of 5 min each, slices were permeabilized in 0.5% Triton-X-100 overnight at 4°C. The next day, the slices were briefly rinsed and then incubated in avidin–biotin complex (ABC; one drop of each reagent to 5 ml of 0.1M TBS containing 5% Triton-X-100, ABC Elite kits, Vector Laboratories, Burlingame, CA) for 2-3 days at 4°C. To visualize neurobiotin labeling, slices were washed 3 times in 0.1M TBS for 10 min each and incubated in 3,3'-Diaminobenzidine (DAB; One drop to 1 ml of 0.1M TBS, ImmPACT DAB kit, Vector Laboratories, Burlingame, CA) until they turned into a darkish brown color. The DAB reaction was then terminated with 3 washes in water and sections were mounted on glass slides using Fluoromount G (Southern Biotech).

Images of neurobiotin labeled TdTom+ PVIs were acquired on a Leica TCS SP5 confocal laser scanning microscope with a Leica PL APO 10x/1.4 air lens in the transmission mode. Z-stacks of optical sections were captured at 0.25-0.4μm intervals, using the following settings (2048 x 2048 pixel, 8 speed, 4 averaging, a pinhole setting of 1.2 Airy units). To sharpen the pictures, the Z-stacks were processed for 2D deconvolution with the Leica Blind Deconvolution module using up to 25 iterations of the Classic Maximum Likelihood Estimation algorithm with a theoretical point spread function (PSF). Selected deconvolved Z-stacks were average projected to provide accurate view of all the neurobiotin labeled structures and the resultant projections were exported in TIFF format for Sholl analysis (Sholl, 1953) in Image J 1.51i (NIH, Bethesda, MD, USA; https://imagej.nih.gov/ij/). To perform semi-automated Sholl analysis, 8-bit images of projected neurobiotin filled cells were traced using the Simple neurite tracer plugin (Longair et al., 2011) for image J (NIH, Bethesda, MD) to generate tagged skeleton traces. The tagged skeleton traces were then converted to 8-bit and branch complexity was analyzed using the Sholl analysis plugin for image J (Ferreira et al., 2014). The initial Sholl analysis window was set at 10μm from the center of the cell soma and the radius of subsequent circles increased by 2μm increments. The number of intersections made by each branch with each circle was plotted against the distance from the soma.

Statistical analysis

Statistical analyses were performed using excel and Graph Pad Prism software (San Diego, CA, USA). In most cases, the unpaired two-tailed Student's *t* test was used for normally distributed data and the Mann-Whitney U test was used for data not normally distributed, with genotype as the variable in both cases. Statistical significance for PPR and some behavioral experiments was determined by single-factor ANOVA from a two-tailed test, followed by Bonferroni *post hoc* test. For the Rotarod test, reference learning test of the MWM, novel object recognition test, RNAseq validation, power spectral analysis, and contextual fear conditioning test, two-way ANOVA with repeated measures was performed using genotype and trials or time as variables. These tests were followed by Tukey, Sidak, or Bonferroni *post hoc* analysis. The Kolmogorov-Smirnoff (K-S) test was used to analyze the cumulative distribution of TTX-dependent and independent miniature postsynaptic currents. Data are given as means (±SEM) and differences in means were considered statistically significant at $p \leq 0.05$. Significance levels [$p<0.05$ (*), $p<0.01$(**), $p<0.001$(***) or $p<0.0001$(****)] are indicated in the text and figures. Sample sizes were not predetermined by power analysis, but they conformed to those reported in similar studies.

REAGENT or RESOURCE	SOURCE	IDENTIFIER
Antibodies		
Rabbit anti-ARX	Neuromab	RRID:AB_2491188
Mouse anti-PV	Millipore Sigma	RRID:AB_2313804
Mouse anti-CB	Swant	RRID:AB_2314070
Rabbit anti-CR	Swant	RRID:AB_2619710
Rabbit anti-SST	ABCAM	RRID:AB_2286681
Rabbit anti-ACAN	Millipore Sigma	RRID:AB_90460
Mouse anti-Cat-315	Millipore Sigma	RRID:AB_94270
FITC Goat-anti rabbit IgG	Jackson Immunoresearch	RRID:AB_10015288
Cy3 Goat anti-mouse IgG	Jackson Immunoresearch	RRID: AB_2338680
Chemicals, Peptides and Recombinant proteins		
Tetrodotoxin citrate	Tocris	Cat# 1069
Picrotoxin	Tocris	Cat# 1128
Bicuculline methiodide	Tocris	Cat# 2503
Glycine	Millipore Sigma	Cat# 410225
Oligonucleotides		
Arx (LoxP Forw: AAG AAC CCC AAA AGCTAA GGA ATG	Invitrogen	N/A
LoxP Rev: TGG AGC GGG GAC AGG GGT GAG GTT	Invitrogen	N/A
Wildtype Rev: GGC CGGTCT CTT TCT TTC TACTCA)	Invitrogen	N/A
Cre (Forw: GGC GCG CGG TCT GGC AGT AAA AAC	Invitrogen	N/A

Rev: CCC TGA TCC TGG CAA TTT CGG CTA TA	Invitrogen	N/A
TdTom (Forw: CTC TGC TGC CTC CTG GCT TCT	Invitrogen	N/A
Rev: CGA GGC GGA TCA CAA GCA ATA	Invitrogen	N/A
Mutant Rev: TCA ATG GGC GGG GGT CGT T)	Invitrogen	N/A
Taqman-Mm01237524_m1 (*Arx*)	Applied Biosystems	N/A
Taqman-Mm00497506_m1 (*Gria3*)	Applied Biosystems	N/A
Taqman-Mm00444666_m1 (*Olfm1*)	Applied Biosystems	N/A
Taqman-Mm0044170_m1 (*Cck*)	Applied Biosystems	N/A
Taqman-Mm00477827_m1 (*Nid1*)	Applied Biosystems	N/A
Taqman-Mm03928990_g1 (18S ribosomal RNA).	Applied Biosystems	N/A
Deposited data		
Bulk RNA sequencing	This paper	GEO: GSE157689
Experimental models		
Mouse: Rosa-CAG-LSL-tdTomato-WPRE	The Jackson Laboratory	RRID:IMSR_JAX:007914
Mouse: B6; 129P2-Pvalbtm1 (cre)Arbr/J	The Jackson Laboratory	RRID:IMSR_JAX:008069
Mouse: Lox P flanked *Arx*	Jeff Golden (Fulp et al., 2008; Marsh et al. 2009)	N/A
Software and Algorithms		
Minianalysis 6.0.3	Jaejin software	N/A
pClamp 10.7	Molecular devices	N/A
Simple neurite tracer plugin	Longair et al., 2011,	https://imagej.net/Simple_Neurite_Tracer
Image J	NIH	https://imagej.nih.gov/ij/
Sholl analysis plugin	Ferreira et al., 2014	https://imagej.net/Sholl_Analysis
ANY-maze software	Stoelting	N/A
MATLAB 2015b	Mathworks	N/A
Harmonie	Stellate systems	N/A
UCSC Genome Table browser	Karolchik et al., 2004	https://genome.ucsc.edu/
Cistrome (v 3.4.0)	Liu et al., 2011	http://cistrome.org/ap/
Prism 8.2	GraphPad	https://www.graphpad.com/scientific-software/prism/
GREAT (v3.0.0)	McLean et al., 2010	http://great.stanford.edu
Bioconductor DESeq2	Love et al., 2014	https://www.bioconductor.org
Other		
Avidin–Biotin Complex	Vector Laboratories	Cat# PK6200

ImmPACT DAB kit	Vector Laboratories	Cat# SK4105

REFERENCES

Ferreira, T.A., Blackman, A.V., Oyrer, J., Jayabal, S., Chung, A.J., Watt, A.J., Sjostrom, P.J., and van Meyel, D.J. (2014). Neuronal morphometry directly from bitmap images. Nat Methods 11, 982-984.

Fulp, C.T., Cho, G., Marsh, E.D., Nasrallah, I.M., Labosky, P.A., and Golden, J.A. (2008). Identification of Arx transcriptional targets in the developing basal forebrain. Hum Mol Genet 17, 3740-3760.

Guo, H., Mao, C., Jin, X.L., Wang, H., Tu, Y.T., Avasthi, P.P., and Li, Y. (2000). Cre-mediated cerebellum- and hippocampus-restricted gene mutation in mouse brain. Biochem Biophys Res Commun 269, 149-154.

Hirata, H., Takahashi, A., Shimoda, Y., and Koide, T. (2016). Caspr3-Deficient Mice Exhibit Low Motor Learning during the Early Phase of the Accelerated Rotarod Task. PloS one 11, e0147887.

Huang da, W., Sherman, B.T., and Lempicki, R.A. (2009a). Bioinformatics enrichment tools: paths toward the comprehensive functional analysis of large gene lists. Nucleic Acids Res 37, 1-13.

Huang da, W., Sherman, B.T., and Lempicki, R.A. (2009b). Systematic and integrative analysis of large gene lists using DAVID bioinformatics resources. Nat Protoc 4, 44-57.

Karolchik, D., Hinrichs, A.S., Furey, T.S., Roskin, K.M., Sugnet, C.W., Haussler, D., and Kent, W.J. (2004). The UCSC Table Browser data retrieval tool. Nucleic Acids Res 32, D493-496.

Liu, T., Ortiz, J.A., Taing, L., Meyer, C.A., Lee, B., Zhang, Y., Shin, H., Wong, S.S., Ma, J., Lei, Y*., et al.* (2011). Cistrome: an integrative platform for transcriptional regulation studies. Genome Biol 12, R83.

Livak, K.J., and Schmittgen, T.D. (2001). Analysis of relative gene expression data using real-time quantitative PCR and the 2(-Delta Delta C(T)) Method. Methods 25, 402-408.

Longair, M.H., Baker, D.A., and Armstrong, J.D. (2011). Simple Neurite Tracer: open source software for reconstruction, visualization and analysis of neuronal processes. Bioinformatics 27, 2453-2454.

Love, M.I., Huber, W., and Anders, S. (2014). Moderated estimation of fold change and dispersion for RNA-seq data with DESeq2. Genome Biol 15, 550.

Marioni, J.C., Mason, C.E., Mane, S.M., Stephens, M., and Gilad, Y. (2008). RNA-seq: an assessment of technical reproducibility and comparison with gene expression arrays. Genome Res 18, 1509-1517.

Marsh, E., Fulp, C., Gomez, E., Nasrallah, I., Minarcik, J., Sudi, J., Christian, S.L., Mancini, G., Labosky, P., Dobyns, W*., et al.* (2009). Targeted loss of Arx results in a developmental epilepsy mouse model and recapitulates the human phenotype in heterozygous females. Brain 132, 1563-1576.

Matta, J.A., Pelkey, K.A., Craig, M.T., Chittajallu, R., Jeffries, B.W., and McBain, C.J. (2013). Developmental origin dictates interneuron AMPA and NMDA receptor subunit composition and plasticity. Nat Neurosci 16, 1032-1041.

McIntyre, L.M., Lopiano, K.K., Morse, A.M., Amin, V., Oberg, A.L., Young, L.J., and Nuzhdin, S.V. (2011). RNA-seq: technical variability and sampling. BMC Genomics 12, 293.

McLean, C.Y., Bristor, D., Hiller, M., Clarke, S.L., Schaar, B.T., Lowe, C.B., Wenger, A.M., and Bejerano, G. (2010). GREAT improves functional interpretation of cis-regulatory regions. Nat Biotechnol 28, 495-501.

Montojo, J., Zuberi, K., Rodriguez, H., Bader, G.D., and Morris, Q. (2014). GeneMANIA: Fast gene network construction and function prediction for Cytoscape. F1000Res 3, 153.

Myme, C.I., Sugino, K., Turrigiano, G.G., and Nelson, S.B. (2003). The NMDA-to-AMPA ratio at synapses onto layer 2/3 pyramidal neurons is conserved across prefrontal and visual cortices. J Neurophysiol 90, 771-779.

Saxena, A., Wagatsuma, A., Noro, Y., Kuji, T., Asaka-Oba, A., Watahiki, A., Gurnot, C., Fagiolini, M., Hensch, T.K., and Carninci, P. (2012). Trehalose-enhanced isolation of neuronal sub-types from adult mouse brain. Biotechniques 52, 381-385.

Shannon, P., Markiel, A., Ozier, O., Baliga, N.S., Wang, J.T., Ramage, D., Amin, N., Schwikowski, B., and Ideker, T. (2003). Cytoscape: a software environment for integrated models of biomolecular interaction networks. Genome Res 13, 2498-2504.

Sholl, D.A. (1953). Dendritic organization in the neurons of the visual and motor cortices of the cat. J Anat 87, 387-406.
Simonet, J.C., Sunnen, C.N., Wu, J., Golden, J.A., and Marsh, E.D. (2015). Conditional Loss of Arx From the Developing Dorsal Telencephalon Results in Behavioral Phenotypes Resembling Mild Human ARX Mutations. Cereb Cortex 25, 2939-2950.

Warde-Farley, D., Donaldson, S.L., Comes, O., Zuberi, K., Badrawi, R., Chao, P., Franz, M., Grouios, C., Kazi, F., Lopes, C.T*., et al.* (2010). The GeneMANIA prediction server: biological network integration for gene prioritization and predicting gene function. Nucleic Acids Res 38, W214-220.

Zhou, F.W., Chen, H.X., and Roper, S.N. (2009). Balance of inhibitory and excitatory synaptic activity is altered in fast-spiking interneurons in experimental cortical dysplasia. J Neurophysiol 102, 2514-2525.